Computational and Experimental Investigation of DSC-MRI Signal Behavior in Magnetically Inhomogeneous Media

By

Natenael B. Semmineh

Dissertation

Submitted to the Faculty of the

Graduate School of Vanderbilt University

in partial fulfillment of the requirements

for the degree of

DOCTOR OF PHILOSOPHY

in

Physics

May, 2014

Nashville, Tennessee

Approved by

Professor C. Chad Quarles

Professor John C. Gore

Professor Daniel F. Gochberg

Professor David J. Ernst

Professor Kalman Varga

ACKNOWLEDGEMENT

I would like to thank my advisor, Professor Chad Quarles, for his consistent support, patient encouragement and invaluable guidance. It has been a privilege to work under his supervision. I would also like to thank Prof. John Gore, Prof. Daniel Gochberg, Prof. David Ernst and Prof. Kalman Varga for being on my committee and taking the time to evaluate this thesis.

I would like to thank my current and former colleagues for their help. I would especially like to thank Dr. Junzhong Xu for the many inspiring discussions and tireless work to make this possible.

This work would not have been possible without the financial support and state-of-the-art research resources provided by the Vanderbilt University Department of Physics and Astronomy and the Vanderbilt University Institute of Imaging Science. My research was funded by NCI grants R00 CA127599, R01 CA158079, P30 CA068485, U24 CA126588.

A great big thanks goes to my late parents, whose love and support has given me the determination to pursue my education. Most of all, I would like to thank and dedicate this dissertation to my wife Lily, whose love, patience and support has been the driving force.

ABSTRACT

The systematic investigation of susceptibility-induced contrast in MRI is important to improve our understanding of the influence of tissue microstructure on dynamic susceptibility contrast (DSC)-MRI derived perfusion data. The Finite Perturber Method (FPM) has previously been used to investigate susceptibility contrast in MRI arising from arbitrarily shaped structures. However, the FPM has low computational efficiency in simulating water diffusion, especially for complex three-dimensional structures that mimic tissue. In this work, an improved computational approach that combines the FPM with a matrix-based finite difference method (FDM), termed the Finite Perturber Finite Difference Method (FPFDM), was developed to more efficiently investigate the biophysical basis of DSC-MRI data and its sensitivity to vascular geometry and contrast agent (CA) distribution within tissue. The application of the FPFDM to the physiological and physical conditions encountered in a typical DSC-MRI brain tumor study enabled the derivation of a new DSC-MRI metric, termed the Transverse Relaxivity at Tracer Equilibrium (*TRATE*), which we propose specifically reports on tumor cellular properties. Computational FPFDM studies revealed that *TRATE* depends on cellular density, size, shape and spatial distribution. To validate the *in vivo* sensitivity of *TRATE* it was evaluated in two animal brain tumor models, the 9L and C6, which have varying cellular characteristics. The *TRATE* values were also compared to measures of the apparent diffusion coefficient (*ADC)*, the CA transfer constant (K^{trans}), the extravascular extracellular volume fraction (v_e) and histological data. The *TRATE* values in 9L tumors were significantly higher than those in C6 tumors, a finding that reflects the histologically confirmed higher cell density in 9L tumors and lower cellular density. A voxel-wise comparison of *TRATE* with *ADC*, v_e, and K^{trans} maps showed low spatial correlation, indicating it is providing unique and complementary information on tumor status. In summary, the studies described herein highlight the value of pairing computational and experimental advancements in order to enhance our characterization of DSC-MRI contrast mechanisms and how such mechanisms can be leveraged to derive new non-invasive metrics for evaluating brain tumors.

TABLE OF CONTENTS

LIST OF FIGURES

CHAPTER III

CHAPTER IV

LIST OF TABLES

CHAPTER 1

INTRODUCTION

Magnetic Resonance Imaging (MRI) is a non-ionizing medical imaging tool that has become a prominent imaging technique in radiological practice. The use of MRI in the field of medical imaging was not introduced until the 1970s when it was shown that normal and abnormal tissue exhibit different signal intensities (1). Compared to other medical imaging modalities, MRI has an outstanding ability to differentiate soft tissues and provides an abundance of anatomical, physiological and functional information. Since its conception there as been considerable progress in MRI, including development of efficient methods for data acquisition, and the use of higher magnetic fields and advanced radiofrequency coil design for human imaging. These advances has transformed MRI from experimental studies of specimens within laboratories to a major diagnostic tool in clinical practice, such as for the detection of tumors and strokes, as well as a powerful tool for many research studies, such as studies of brain structure and function in neuroscience. Despite the remarkable progress in MRI methodologies, the complex nature of MR signal has limited our understanding of what physical, physiological and pulse sequence factors affect MR signal changes in various situations. This study attempts to investigate the biophysical basis of signal changes observed in a specific MRI technique known as Dynamic Susceptibility Contrast Magnetic Resonance Imaging (DSC-MRI).

The passage of highly paramagnetic (e.g., Gd-DTPA or Dy-DTPA) or superparamagnetic (e.g., magnetized iron oxide particles) contrast agents (CA) through brain tissue induces a measurable drop in T_2- or T_2^*-weighted MR signal (2) that forms the basis for DSC-MRI. When combined with appropriate kinetic models, DSC-MRI can be used to measure hemodynamic parameters quantitatively, such as blood flow (BF), blood volume (BV) and mean transit time (MTT) (3). This imaging approach relies upon MR signal relaxation enhancement created by CA-induced susceptibility differences between tissue compartments, such as blood vessels and the surrounding extravascular space. The assessment of tumor perfusion parameters using DSC-MRI has proven to be useful for characterizing tumor grade (4-10) and treatment response (11-15). Despite its increased use in brain tumor and stroke patients, accurate calculation of perfusion parameters using DSC-MRI relies on two assumptions: 1) a linear relationship, with a spatially uniform rate constant termed the vascular susceptibility calibration factor (k_p), exists between CA concentration and the measured transverse relaxation rate change (16); and 2) the blood-brain barrier (BBB) is intact, so that contrast agent remains intravascular and can be treated as a nondiffusible tracer (3). However, heterogeneous distributions of blood vessels within tissue and the dependence of susceptibility field gradients on vascular geometry may yield spatially variant k_p values across tissue. Furthermore, leakage of contrast agent in tumors with BBB disruption causes additional T_1 and T_2^* shortening with subsequent distortion of DSC-MRI signal profiles (17-21). Improved characterization of these potential confounding factors could shed new insights into the biophysical basis of DSC-MRI signals and direct future improvements in acquisition and post-processing strategies. Because of the complex heterogeneous nature of biological tissues and their widely different composition, which can be further complicated by disease, the relationship between observed MR signal changes and specific underlying causes are not well understood. However, a better understanding of the relation between relevant

parameters and measured signal variations in tissues can be achieved through realistic computer simulations. This is the rationale behind the work presented in this thesis.

The first part of this work is devoted to develop and validate an efficient computational approach to estimate the intravascular and extravascular magnetic field perturbations induced by magnetic susceptibility variation between arbitrary shaped mesoscopic scale compartments, and also the associated spin echo (SE) and gradient echo (GE) transverse relaxation rate enhancement. The subsequent part of this thesis utilizes the validated computational tool to investigate the influence of vascular and cellular morphology as well as physiological and pulse sequence parameters on DSC-MRI signals using simulated three-dimensional tissue structures.

This thesis is organized as follows:

A brief overview of NMR focusing on experimental and theoretical concepts crucial to understand the subsequent research topics is presented in chapter 2.

Chapter 3 proposes an efficient computational approach called the Finite Perturber Finite Difference Method (FPFDM), as a tool for modeling susceptibility based contrast mechanisms. The accuracy of the proposed tool is validated by comparison with previous traditional Monte Carlo methods. In addition to its potential applications, the advantages and limitations of the FPFDM in contrast to previous methods are discussed in detail.

Chapter 4 presents the results of computational studies of the influence of vascular morphology on susceptibility induced DSC-MRI signal changes. The computational studies are carried out using fractal tree based three-dimensional vascular models. In addition, k_p values are characterized for vascular structures obtained from micro-CT based renal angiograms. The results show marked k_p heterogeneity across vascular networks, suggesting that the assumption of a constant k_p for all tissue types could affect DSC-MRI derived perfusion parameters.

Chapter 5 investigates the dependence of extravascular T_2^* effects on cellular features. Computational results, obtained using tissue structures composed of randomly distributed ellipsoids around fractal tree based vascular network, show that DSC-MRI data acquired in the presence of contrast agent leakage are highly sensitive to variations in cellular features.

Chapter 6 proposes a new imaging biomarker that may be used to evaluate brain tumor cytoarchitecture. The combination of multi-echo DSC-MRI acquisition method to simultaneously quantify the changes in T_1 and T_2^*, and analytical gradient-correction model were used to enable the estimation of the Transverse Relaxivity at Tracer Equilibrium (*TRATE*). To validate the sensitivity of *TRATE* to tumor cellular features we employ realistic biophysical simulations and compare its characteristics in two animal brain tumor models that are known to have histologically different cellular properties. We also present initial results of *TRATE* data in a glioma patient. The *TRATE* maps are spatially compared to parameters traditionally derived from DSC-MRI, Dynamic Contrast Enhanced (DCE)-MRI and Diffusion Weighted Imaging (DWI) in order to preliminarily assess its potential to provide unique sensitivity to microstructural features not assessed with these techniques.

Summary of the work presented in this thesis along with future research directions are presented in chapter 7.

CHAPTER 2

FUNDAMENTALS OF MRI

2.1 A Brief History of NMR and MRI

In 1938, Rabi et al (22) demonstrated that electromagnetic waves with certain frequencies could be used to induce transition of magnetically aligned nuclei from one energy state to the other. This observation has allowed the measurement of magnetic properties of atomic nuclei using a 'resonance' method, and was the basis for the origin of nuclear magnetic resonance. In 1946, Bloch and Purcell advanced the technique for use on liquids and solids. Purcell observed a phenomenon he later called 'nuclear magnetic resonance' (NMR) by studying the precession of nuclear magnetization in a magnetic field with a constant radiofrequency (RF), which resulted a strong absorption of radiation as nuclei flipped from the lower to the higher energy state (23). Bloch investigated the water in an adjustable magnetic field and, rather than measuring absorption, he detected re-emission of resonant radiation using a second coil placed perpendicular to the first (24). Although Rabi's work was crucial, both works by Purcell and Bloch were a very big leap forward, laying the foundation for the development of modern NMR and MRI techniques. In 1950, Hahn discovered the spin echo (25), which is considered the beginning of the widespread use of pulsed NMR methods. In 1973, Lauterbur described the use of linear magnetic field gradients to spatially localize NMR signals (26). He obtained spectra that were actually the projections of an object's spin density distribution onto the gradient axis. By rotating the object in the field, a series of angular projections could be obtained and two-dimensional MR images were reconstructed using the mathematics of filtered back projection developed for computed tomography. Soon after that, Sir Peter Mansfield published an extensive paper showing projection images of a human finger, which perhaps was the first MRI of live human anatomy (27). In order to speed up the scan acquisition, he also developed an MRI protocol called echo planar imaging (EPI) (28), which made fast imaging possible.

In the forty years since its invention, MRI has continued to grow at an incredible speed with significant discoveries in both research and clinical applications. For instance, the realization of clinically feasible EPI sequences through improved gradients enabled the development of the field of DSC-MRI and enabled the non-invasive assessment of perfusion in normal, ischemic and tumor-bearing brain (4,8,9,16). Rapid imaging also enabled the development of functional MRI techniques for detecting brain neuronal activation based on the blood oxygenation level dependent or BOLD effect (29). Numerous methods have been developed that leverage MRI's sensitivity to the magnetic properties of protons in heterogeneous biological conditions in order to assess, for example, water diffusion, metabolic composition, protein content, and proton exchange rates. A total of seven outstanding scientists have been awarded Nobel Prizes for their major contributions to the discovery and development of NMR and MRI.

2.2 Basic Principles of MRI Physics

MRI is based on the interaction of nuclear spins with an external magnetic field. In the presence of an external magnetic field, B_0, the magnetic moment of a spin will precess about the field direction with an angular frequency given by the Larmor equation:

$$\omega_0 = \gamma B_0 \tag{2.1}$$

where ω_0 is called the Larmor frequency and γ is the gyromagnetic ratio. (the hydrogen proton has a γ value of 2.675×10^8 rad/s/T). A static magnetic field B_0 results in a net longitudinal equilibrium magnetization, M_0, aligned along the B_0 direction, which by definition is taken to be along the z direction. If another perpendicular radiofrequency (RF) magnetic field (B_1) (tuned to the Larmor frequency) is applied in a short time (an RF 'pulse'), spin magnetic moments will be 'tipped' away from the alignment along the B_0 direction and towards the transverse plane, in which the magnetization will have *x* and *y* components M_x and M_y, as well as M_z along the B_0 direction.

The magnetization of the system returns to equilibrum through 2 processes: T_1 and T_2 relaxation. Relaxation is caused by fluctuations in the local field felt by a magnetic nucleus. If this field fluctuates at the appropriate frequency, it induces transitions between spin states, causing relaxation. The time for magnetization to recover from the excited state to original longitudinal equilibrium state (along B_0 direction) is described by T_1, which is called longitudinal relaxation time or spin-lattice relaxation time. The spin-spin relaxation, which primarily occurs as spins exchange energy with each other and lose coherence in the transverse plane, causes the transverse magnetization decay and can be described by T_2. The equation of motion for the spin magnetization in the presence of a magnetic field and with relaxation terms can be expressed by the Bloch equation (30)

$$\frac{d\vec{M}}{dt} = \gamma\vec{M}\times\vec{B}_{eff} + \frac{1}{T_1}\left(M_0 - M_z\right)\hat{z} - \frac{1}{T_2}\vec{M}_{\perp} \tag{2.2}$$

The T_1 and T_2 relaxation times vary greatly from tissue to tissue and thus provide excellent sources of contrast in medical imaging. In addition to the effects of intrinsic T_2 relaxation, spatial inhomogeneities in the magnetic field induce additional transverse magnetization decays. These magnetic field inhomogeneities arise from hardware limitation to create a perfectly homogeneous B_0 field, and existence of susceptibility inhomogeneities within the object being imaged. The presence of field inhomogeneities cause spins to precess at different rates and lose their phase coherence. This leads to a transverse relaxation time called T_2^*, which can be significantly shorter than T_2.

The random Brownian motion of the spins has been shown to contribute to the attenuation of the observed spin echo signal (25). To incorporate this self-diffusion effects Torrey developed a continuum description based on the magnetization diffusion equation and Bloch equation, which was subsequently named as the Bloch-Torrey equation. For the transverse magnetization of interest, the Bloch-Torrey equation can be written as

$$\frac{\partial \vec{M}_{\perp}}{\partial t} = -i\gamma\left(g(\vec{r},t).\vec{r}\right)\vec{M}_{\perp} - \frac{\vec{M}_{\perp}}{T_2} + \nabla\left(D\vec{M}_{\perp}\right) - \nabla V.\vec{M}_{\perp}, \tag{2.3}$$

where $M_{\perp}$ is the transverse magnetization, D is diffusion coefficient, $g(r,t)=\nabla B(r,t)$ is the applied magnetic gradient, v is the velocity of the fluid flow.

2.3 MR Signal Detection

The time-varying transverse magnetization induces an electromotive force (*emf*) in a receiver coil wrapped around the sample. However, the signal measured in the coil, which is known as the free induction decay (FID), is from the whole sample. In order to acquire MR images, it is necessary to implement a technique, which applies spatially dependent fields (linearly dependent with a constant gradient) to encode signals. Appling field gradient along *x* direction yields a spatially dependent Larmor frequency as $\omega(x)=\gamma(Gx+B)$, which leads to different spins precessing at different rates. The resulting detected MR signal will then be a superposition of many frequencies, and can be expressed as

$$S(t) = \int \rho(x)\exp(i\phi)dx, \tag{2.4}$$

where $\rho(x)$ is density of transverse magnetization precessing at $\omega(x)$ and ϕ represents the phase, which is given by

$$\phi(x,t) = -\gamma x \int_0^t G(t')dt' \tag{2.5}$$

The signal in Eq. (2.4) can be written as

$$S(k) = \int \rho(x)\exp(-i2\pi kx)dx \tag{2.6}$$

where

$$k = -\frac{\gamma}{2\pi}\int_0^t G(t')dt' \tag{2.7}$$

It is clear from Eq. (2.6) shows that the MR signal is the Fourier transform of the spin density of the sample. By systematically manipulating the gradient fields, a grid of points in *k* space can be covered and a series of corresponding signal points can be obtained. An image of the sample spin density can easily be obtained using inverse fast Fourier transform of measured signals. This brief description underlines the basic principle of MRI.

2.4 Basic Principles of DSC-MRI

2.4.1 Susceptibility Based Contrast

Susceptibility induced contrast is an important source of contrast in MRI. When a system composed of objects with different susceptibilities is immersed in a uniform static magnetic field, the boundaries between the objects cause distortion of the static field. These field perturbations facilitates the loss of spin phase coherence and contributes to T_2^* relaxation. Example sources of susceptibility contrast in the body include blood vessels, bone marrow, and air bubbles. To alter the susceptibility of blood in the body, paramagnetic or superparamagnetic contrast agents are sometimes injected into the bloodstream. As a result a significant transverse relaxation occurs in the vicinity of contrast agent containing vessels. MR signal measured during the passage of the CA through the body exhibits substantial signal drop in areas with high blood volume and blood flow. Alternatively, in addition to exogenous CA injected to change blood vessel susceptibility, the susceptibility difference between oxygenated and deoxygenated blood can be used as a naturally occurring susceptibility contrast mechanism. When blood flow in a tissue of interest increases, oxygenated blood (diamagnetic) replaces deoxygenated blood (highly paramagnetic). This leads to a decrease in field perturbation hence an increase in signal. The nature of the susceptibility contrast mechanism has made blood a useful source of contrast because it can be used as a marker to indicate hemodynamic properties of tissue.

2.4.2 Perfusion Measurement Using DSC-MRI

DSC-MRI utilizes very rapid imaging (most commonly T_2^* weighted gradient-echo echo planar imaging, GE-EPI) to capture the first pass of intravenously injected paramagnetic CA. The time evolution of the MRI signal from such a sequence can be written as

$$S(t) = \frac{S_0\left(1 - e^{-TR/T_1(t)}\right)e^{-TE/T_2^*(t)}\sin(\alpha)}{1 - e^{-TR/T_1(t)}\cos(\alpha)} \tag{2.8}$$

where S_0 is a constant describing the scanner gain and proton density, TR is the repetition time, TE is the echo time, α is the flip angle, and $T_1(t)$ and $T_2^*(t)$ are tissue longitudinal and transverse relaxation times, respectively, shortened by the CA.

Assuming appropriate pulse sequence parameter choice and negligible blood signal contribution to the overall tissue MRI signal, signal changes due to changes in longitudinal relaxation rate, $\Delta R_1(t) = 1/T_1(t)$, can be eliminated. The transverse relaxation rate, $\Delta R_2^*(t) = 1/T_2^*(t)$, is then computed using:

$$\Delta R_2^*(t) = \frac{-1}{TE}\ln\left(\frac{S(t)}{S(0)}\right) \tag{2.9}$$

where S(0) is the baseline signal acquired before CA injection.

Quantification of perfusion parameters is achieved by comparison of CA concentration time course in both a the tissue of interest and a feeding artery. In practice, the tissue CA concentration ($C_t(t)$) is measured indirectly via the associated increase in the transverse relaxation rate. It is assumed that the underlying dependence is linear and has the same form and magnitude in both the tissue and the arterial voxel. Using a uniform vascular susceptibility calibration factor (k_p) the tissue CA concentration can be expressed as

$$C_t(t) = \frac{-1}{k_p TE} \ln\left(\frac{S(t)}{S(0)}\right) \tag{2.10}$$

In common DSC-MRI practice the relative cerebral blood volume (rCBV) is estimated using the ratio of the areas under the tissue and arterial concentration time curves (3,31-33):

$$rCBV = \frac{\int_0^\infty C_t(\tau)\,d\tau}{\int_0^\infty C_a(\tau)\,d\tau} \tag{2.11}$$

In order to calculate blood flow using tracer kinetic theory, first DSC-MRI estimates of the temporal shapes of the input concentration into the voxel and the tissue concentration curve are required. The input concentration time curve is different for every voxel. The most common approach is to measure the contrast agent concentration curve in a large feeding artery and then to apply this arterial input function ($C_a(t)$) to all of the voxels in the brain. The tissue concentration curve is determined by a combination of the blood flow, $C_a(t)$ and the inherent tissue properties. The property of the tissue is modeled using s a "residue function," R(t), which describe the fraction of tracer remaining in the voxel at time t after injection. Using the residue function the relationship between the tissue concentration and $C_a(t)$ is given by the well-known convolution equation (33-35):

$$C_t(t) = CBF \bullet C_a \otimes R(t) \tag{2.12}$$

where $\otimes$ is the convolution operator, CBF is the cerebral blood flow, and the product CBF R(t) is called the tissue impulse response function. In order to derive CBF from Eq. (2.12), the tissue impulse response function has to be determined by a deconvolution technique. Several deconvolution techniques such as, methods that utilize the properties of the Fourier transform (35), a well accepted matrices based approach known as singular value decomposition (SVD) and also parametric deconvolution methods which assume a shape for the residue function (34), has been used to solve for the tissue impulse response function. After deconvolution, since the initial value of residue function is 1 by definition, R(0)=1, CBF is commonly determined as the initial height of the tissue impulse response function. The detail mathematics basis of these deconvolution techniques and their respective advantage and drawbacks are beyond the scope of this research topic.

The mean transit time (MTT) is calculated based on the central volume theorem (33),

$$MTT = \frac{CBV}{CBF} \tag{2.13}$$

Hemodynamic parameters quantified using DSC-MRI technique as described above has proven to be useful for characterizing tumor grade and treatment response (4-15). Nevertheless, the common assumption that k_p values are spatially uniform for all tissue types could lead to either an overestimated or underestimated perfusion parameters depending on the relative k_p variation between the reference region, where $C_a(t)$ is measured, and the tissue of interest, where $C_t(t)$ is measured (36). Chapter 4 is dedicated to utilize the FPFDM to investigate the extent of k_p variation across tissue models, as well as its relation with structural parameters and influence on DSC-MRI derived blood volume fraction.

Furthermore calculation of perfusion parameters relies on the concept of tracer kinetic theory, which assumes that contrast agent remains within the compartment of interest so that it can be treated as a nondiffusible tracer (3). This assumption is valid in normal tissue where the blood-brain barrier (BBB) is generally intact. However, in tumors with BBB disruption the leakage of contrast agent causes undesirable additional T_1 and T_2^* shortening with subsequent distortion of DSC-MRI signal profiles, which result in unreliable perfusion measures if left uncorrected (17-21). It has been sufficiently shown that T_1 extravasation effects can be minimized with the application of a preloading dose of contrast agent (8) or by using multiecho methods (37). The focus of Chapter 5 is quantifying T_2^* leakage effects and understanding its relation with physical and physiological features of the extravascular space. Chapter 6 exploits the unpleasant contribution of T_2^* leakage effects to extract a new imaging biomarker to characterize tumor cellularity.

CHAPTER 3

AN EFFICIENT COMPUTATIONAL APPROACH TO CHARACTERIZE DSC-MRI SIGNALS ARISING FROM THREE-DIMENSIONAL HETEROGENEOUS TISSUE STRUCTURES

3.1 Overview

Chapters 1 and 2 have presented basic overview of susceptibility contrast mechanism and DSC-MRI. Despite the success of DSC-MRI technique to estimates of perfusion parameters in order to assess tumor grade and treatment response, there are many difficulties to overcome in order to achieve an accurate and robust calculation of perfusion parameters. These challenges range from optimization of data acquisition to data post processing and interpretations (38). DSC-MRI derived perfusion parameters are often confounded due to an assumed relationship between contrast agent concentration and measured transverse relaxation rate change, and leakage of contrast agent into the extravascular space. Understanding the relation between DSC-MRI signal and the complex morphological and physiological tissue parameters could help to optimize data acquisition techniques as well as improve the reliability of perfusion calculations. Therefore, to better understand the biophysical basis of DSC-MRI signal in biological tissues with more complex morphologies, it is necessary to develop an efficient computational tool capable of simulating DSC-MRI signal in realistic tissue structures.

In order to better understand susceptibility-based image contrast, several theoretical (39-43) and computational models using fixed perturber geometry (e.g., cylinders or spheres) (43-50) have been proposed. To address the limited ability of these computational models to represent the complex vascular morphologies in both normal brain and tumors, Pathak et al introduced the Finite Perturber Method (FPM) for simulating susceptibility-based contrast for arbitrary microvessel geometries (51) and evaluating differences in k_p for normal brain and tumor (36). The FPM uses estimated magnetic field perturbations to calculate MR signal by simulating proton diffusion and phase accumulation using the conventional time consuming Monte Carlo methods.

For realistic complex tissues, the MC method needs to track the diffusion of a large number of spins to capture complex structural features, which in turn can increase the computation time. As an alternative, the Bloch-Torrey partial differential equation describing the transverse magnetization can be directly solved using finite difference methods (FDM). This approach has been previously shown to improve the computational efficiency of such simulations (52,53) and used to explore water diffusion in MRI and to aid the interpretation of diffusion-weighted imaging measures and their dependence on the morphology of biological structures such as those found in tumors.

The aim of the research presented in this chapter is to evaluate the combination of the finite pertuber and finite difference methods, termed the FPFDM, as a tool for modeling susceptibility based contrast mechanisms. Such an approach leverages the strengths of the FPM, for computing magnetic field perturbations for arbitrarily shaped structures, and the FDM, for efficiently computing the resulting MRI signal evolution. The accuracy of the FPFDM is validated by comparison to traditional Monte Carlo methods. In the following chapters the potential of the

FPFDM to compute DSC-MRI signals arising from realistic three-dimensional cellular and vascular models is exploited to investigate the influence of vascular morphology, contrast agent kinetics and extravasation on DSC-MRI signals.

3.2 The Finite Perturber Finite Difference Method (FPFDM)

In this section, we first describe the method to compute magnetic field perturbations induced by susceptibility differences between arbitrary shaped tissue compartments. We then describe the calculation of the associated MR signal evolution.

3.2.1 Computation of Magnetic Field Perturbations Using the FPM

The magnetic field perturbations induced by susceptibility variations within tissue structures were computed using the FPM (51). To calculate the magnetic field shift at a given point, the FPM breaks the structure into numerous small cubic perturbers (finite pertubers) and the contribution to the magnetic field shift due to each perturber is calculated independently. The total magnetic field shift is then evaluated as the sum of the magnetic field shifts from all of the perturbers. As a computational input the FPM requires: a tabular listing of the tissue structure, the B_0 field components, and the susceptibility difference ($\Delta\chi$) between tissue compartments.

The first step in FPM is to sample the 3D tissue volume with N^3 cubic voxels. The resulting array is then represented using a binary function $V(x,y,z)$ indicating whether a given point/voxel within the tissue volume lies inside or outside a specific compartment (cellular or vascular), i.e.:

$$V(x,y,z)=\begin{cases} 1, & \textit{if } (x,y,z) \textit{ is inside simulated compartments} \\ 0, & \textit{if } (x,y,z) \textit{ is outside simulated compartments} \end{cases} \tag{3.1}$$

The magnetic field shift arising from a single finite cubic perturber at point $P(x,y,z)$ is approximated by the magnetic field shift of a sphere embedded within the cube weighted by a volume factor $6/\pi$, and is given by:

$$\Delta B_{cube}(x,y,z)=\frac{6}{\pi}\frac{\Delta\chi}{3}\frac{R^3}{r^3}(3\cos^2\theta-1)B_0 \tag{3.2}$$

where R is the radius of the sphere equivalent to one-half the size of the cube, $\Delta\chi$ is the susceptibility difference between tissue compartments, and r and θ indicate the distance from the center of the cube and the angle with respect to B_0 of the magnetic field calculation point, respectively. The volume-weighting factor ($6/\pi$) is used to compensate for the unoccupied space left by the sphere at each corner of the cube.

The total magnetic field perturbation arising from the entire compartment of interest, can be calculated by integrating Eq. (3.2) over the entire tissue volume:

$$\Delta B(x,y,z) = \int_{volume} V(\zeta,\eta,\xi)\Delta B_{cube}(x-\zeta, y-\eta, z-\xi)\, d\zeta\, d\eta\, d\xi \tag{3.3}$$

Eq. (3.3) represents a 3D convolution of the tissue structure with the finite perturber field shift, suggesting the use of the convolution theorem to achieve a computationally efficient means of calculating the magnetic field perturbation map arising from the entire tissue structure. Taking the Fourier transform of Eq. (3.3) and making use of the convolution theorem one finds:

$$\Delta B(x,y,z) = \Im^{-1}\ \{\Im\ \ \{V(x,y,z)\}\ \ \Im\{\Delta B_{cube}(x,y,z)\}\} \tag{3.4}$$

Equation (3.4) illustrates, performing a point-wise multiplication of the 3D fast Fourier transform of the tissue structure and the magnetic field arising from a single finite perturber followed by inverse Fourier transform of the resulting 3D function yields the magnetic field perturbation map arising from the entire tissue structure.

3.2.2 Computation of MR Signal Using the FDM

Estimation of the MR signal relaxation induced by the inhomogeneous field gradients requires simulation of proton diffusion. To track the Brownian motion of thousands of protons over a large number of time steps and calculate their phase accumulation, a Monte Carlo (MC) simulation is frequently used (43-49,51). The MC method is potentially time consuming for complex tissue structures because in order to accurately calculate the phase distribution it must track a large number of spins that encounter tissue boundaries during their random walks. An alternative approach is to directly solve the Bloch-Torrey partial differential equation using the FDM (52). The FDM discretizes the tissue sample to a spatial grid and updates the magnetization at each grid point over a series of time steps. To increase the computational efficiency and eliminate edge effects encountered with traditional FD methods an improved matrix-based FDM with a revised periodic boundary condition has been previously developed (53). For tissue structures sampled with N^3 voxels the discretized solution of the Bloch-Torrey equation for transverse magnetization (M) using the matrix-based FDM is described by:

$$M(t+\Delta t) = \Phi(t) \otimes (I + A) M(t), \tag{3.5}$$

A is an $N^3 \times N^3$ diffusion transition matrix containing the tissue structural information given in terms of the jump probabilities (probability that a spin starts at one grid point and diffuses to another grid point after a time interval Δt), I is an identity matrix with the same size of A, and $\otimes$ represents element-by-element vector multiplication. The $\Phi(t)$ term is a $1 \times N^3$ vector containing the phase accumulation and relaxation for each voxel at each time step and is given by:

$$\Phi(t) = [\exp(-i\gamma\Delta B_1(t)\Delta t - \Delta t / T_{2,1}), \cdots, \exp(-i\gamma\Delta B_k(t)\Delta t - \Delta t / T_{2,k}), \cdots,$$
$$\exp(-i\gamma\Delta B_{N^3}(t)\Delta t - \Delta t / T_{2,N^3})] \tag{3.6}$$

where γ is the proton gyromagnetic ratio (267.5×10^6 rad s^{-1} T^{-1}), Δt is the simulation time step, the subscript k indicates a spatial index, $\Delta B_k(t)$ is the field perturbation at point k, and $T_{2,k}$ is the transverse relaxation time at location k within the simulation grid. When a GE sequence is used $T_{2,k}$ represent the intrinsic tissue T_2^*, and in the case of SE it represents the intrinsic T_2. In general, the jump probability from simulation grid a to b is described by:

$$s_{a\to b} = \begin{cases} \dfrac{D_{a\to b}\Delta t}{\Delta x_{a\to b}^2} & if \quad a \equiv b \\ \dfrac{2\Delta t}{\Delta x_{a\to b}^2} \cdot \dfrac{D_a D_b P_m c_f c_b \Delta x_{a\to b}}{D_a c_a c_f P_m \Delta x_{a\to b} + 2 D_a c_a D_b c_b + D_b c_b c_f P_m \Delta x_{a\to b}} & if \quad a \neq b \end{cases} \tag{3.7}$$

where $D_{a\to b}$ is the diffusion coefficient if a and b are within the same compartment, $\Delta x_{a\to b}$ is the distance between simulation grid a and b, P_m is the permeability of the membrane when a and b are in different compartments, c_f is the free concentration of water. The explicit form of the 1D transition matrix can be found in (53). The MR signal normalized to the initial magnetization M^0 is estimated by summing the magnetizations over all grid points at a particular t and is given by:

$$S(t) = \frac{1}{M^0} \sum_{k=1}^{N^3} M(t) \tag{3.8}$$

The associated spin echo and gradient echo change in transverse relaxation rates are then calculated at a particular echo time $t = TE$ using:

$$\Delta R_2, \Delta R_2^* = -\frac{\ln S(TE)}{TE} \tag{3.9}$$

For spin echo imaging, the phase was inverted at $t = TE/2$. This model is designed to handle cases where the three tissue compartments within a voxel can have different intrinsic transverse relaxation times. By updating $T_{2,k}$ in equation 5, for each grid point at each simulation time step, the total transverse relaxation, which includes the microscopic and mesoscopic relaxation effects, can also be calculated. The decay of signal from large static perturbers is known not to be exponential (e.g. diffusion in a static linear field gradient) but a simple exponential fit is a good approximation for realistic cases, and other functions can be easily fit. All simulations were performed in the Matlab environment (Mathworks, Natick, MA) running on Intel Core 2 Duo at 2.66GHz and 4GB of RAM processors. For clarity, the computational steps involved to obtain the final results using the FPFDM are illustrated in Fig 3.1.

3.3 Monte Carlo Method

To demonstrate the computational accuracy of the FPFDM computed MR signals were compared with those obtained from MC method. Monte Carlo method, which is based on the first principles, uses computer-generated random numbers to simulate the random processes. In this case MC method is used to model proton diffusion within a magnetically heterogeneous medium and calculate the associated MR signal relaxation. Here MC technique is described briefly, at time t = 0 thousands of particles (spins) are initially placed at random locations within the simulation space. Then, after allowing each proton to diffuse randomly for a time Δt, the new location for each proton is updated using:

$$r_j(t+\Delta t) = r_j(t) + \sqrt{6D_j\Delta t}\,r', \tag{3.10}$$

Where $r_j(t)$ is the position of j^{th} particle at time t, D_j is the intrinsic diffusion coefficient at the location of the j^{th} particle, Δt is simulation time step, and r' is a unit vector in an arbitrary direction. The phase accumulated by the j^{th} particle after diffusing for time t is calculated using:

$$\phi_j(t) = \sum_{k=1}^{t/\Delta t} \gamma \Delta B(r_j(k\Delta t))\Delta t \tag{3.11}$$

Where γ is proton gyromagnetic ratio, $\Delta B(r(t))$ is magnetic field perturbation calculated at location $r(t)$ using the FPM . The MR signal is finally calculated by summing the accumulated phase shift across N diffusing protons:

$$S(t) = \frac{1}{n}\sum_{j=1}^{n} \exp(i\phi_j(t)) \tag{3.12}$$

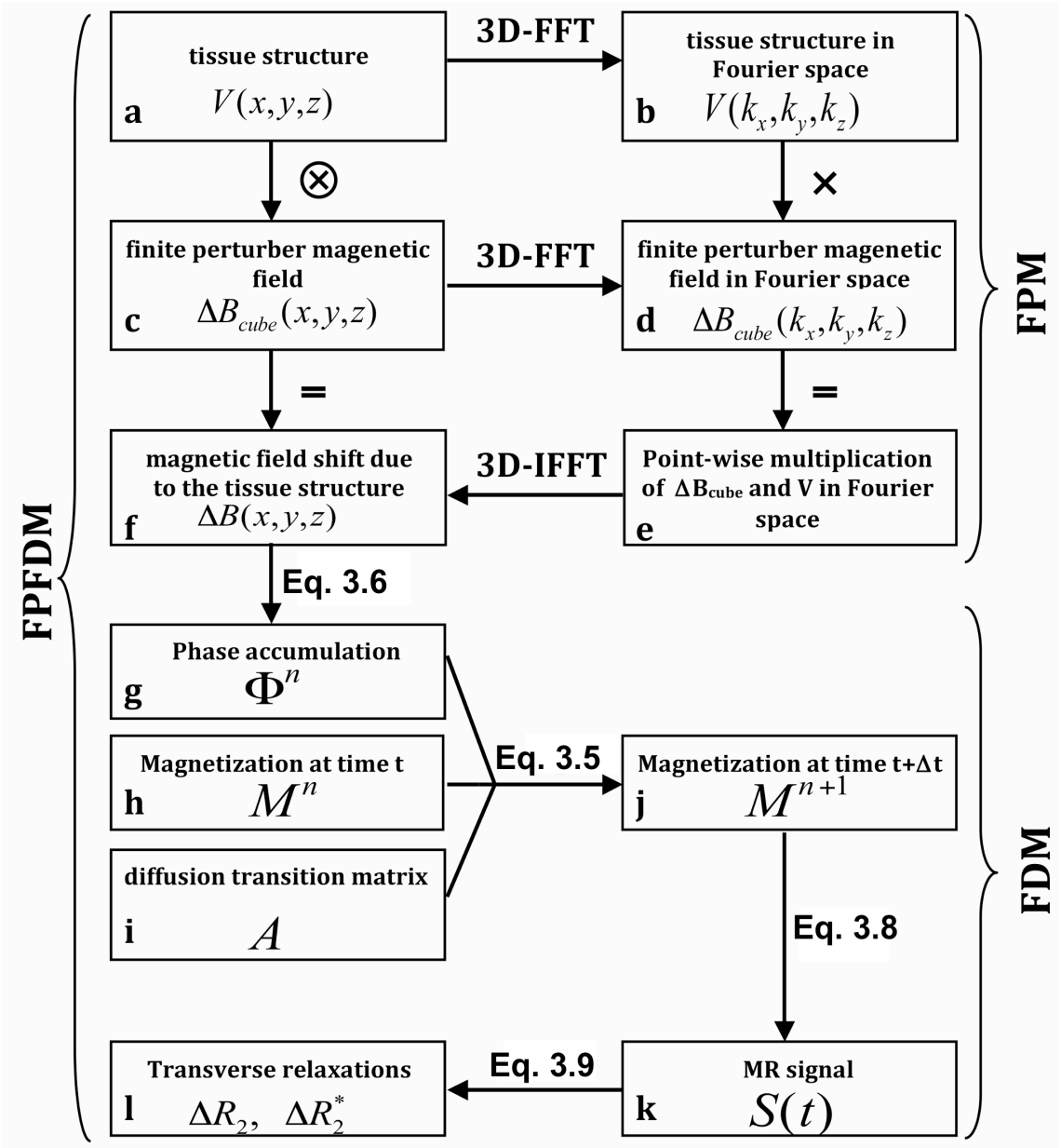

Figure 3.1: Computational steps involved in the FPFDM. This figure illustrates the steps involved in computing the susceptibility induced transverse relaxation rates for a 3D tissue structure using the FPFDM: (a) The tissue structure is $V(x,y,z)$. (b) The 3D Fourier transform of (a). (c) The magnetic field from the cubic finite perturber. (d) The 3D Fourier transform of $\Delta B_{cube}(x,y,z)$. (e) The point-wise multiplication of (b) and (d) in the Fourier domain. (f) The magnetic field shift due to the vascular structure computed as the 3D inverse Fourier transform of (e) or the convolution of (a) and (c). (g), (h) and (i) are the phase accumulation, the magnetization and the diffusion transition matrix, respectively. These are used to compute the magnetization in (j). (k) The computed MR signal. (l) The transverse relaxation rates associated with an arbitrarily shaped tissue structure.

3.4 Validation of the FPM

The accuracy of the FPM to calculate field perturbation has been tested using simple geometries with known theoretical field perturbations (51). In this section example validation of our version of the adopted FPM is presented by comparing the computational results with analytical solutions for cylindrical perturbers. For a long cylinder oriented along the y-axis and immersed in a region of constant magnetic field B_0 in the z-axis (see Fig. 3.2a), the theoretical field shift along the z-axis and the x-axis normalized to the applied magnetic field B_0 and the susceptibility difference ($\Delta\chi$) is given by (30):

$$\frac{\Delta B_{z,x}}{\Delta\chi B_0} = \begin{cases} -1/6 & \rho < R \\ \pm 1/2 \dfrac{R^2}{\rho^2} & \rho \geq R \end{cases} \tag{3.13}$$

Where ρ is the distance to the point of interest and R is the radius of the cylinder. As seen from Eq. (3.10) while the field shift is constant in side the cylinder, outside it falls with $1/\rho^2$ as we go away from the axis of the cylinder with positive field shifts in the direction parallel to the applied field (z-axis) and negative shift along x-axis. Figure 3.2 shows the excellent agreement between the magnetic field perturbations computed from theory and the FPM performed using 128^3 simulation grids. Example 2D map through the magnetic field perturbation shows the dipole nature of the field shift as expected. In general, increasing the number of simulation grids minimizes the small difference at the edge of the cylinder between the two field perturbations.

3.5 Validation of the FPFDM

For validation, FPFDM and Monte Carlo based MRI signals were computed and compared for models consisting of randomly orientated cylinders and packed spheres. The dependence of gradient-echo (ΔR_2^*) and spin-echo (ΔR_2) relaxivity on perturber (vessel) size has previously been characterized using Monte Carlo techniques (45). To replicate these findings we created 10 different structures composed of approximately 40 randomly distributed cylinders for each vessel radius taken between 1μm and 100μm, each with total cylinder volume fraction equal to 2% of the simulation cube. Using the previously reported simulation parameters (45,51) (susceptibility difference $\Delta\chi = 10^{-7}$, cylinder volume fraction (V_p) = 2%, B_0 = 1.5T, water diffusion coefficient D = 10^{-5} cm^2/s, simulation time step Δt = 0.2 ms, GE TE = 60 ms and SE TE = 100 ms), we computed the vessel size dependence of ΔR_2^* and ΔR_2 averaged over all cylinder arrangements. The computed ΔR_2^* and ΔR_2 values show negligible changes as the number of averaged structures increases beyond 10. As shown in Fig. 3.3a, there is excellent agreement between the FPFDM results and those obtained in the Monte Carlo-based comparison studies, which used analytical expressions (45) and FPM (51) for field perturbation calculations.

To compare the computational efficiency of the FPFDM with that of the MC method, we computed ΔR_2^* values using both techniques. For each technique ΔR_2^* values were computed for

18 radii using a TE = 60 ms and Δt = 0.2 ms. The computation time for the FPFDM was approximately 140 seconds per structure. Using 1000 randomly distributed spins, the computation time for the MC method was approximately 220 seconds per structure. Table 3.1 summarizes the simulation parameters used in the MC and FPFDM along with the respective computational times to generate ΔR_2^* values for 18 cylinder radii.

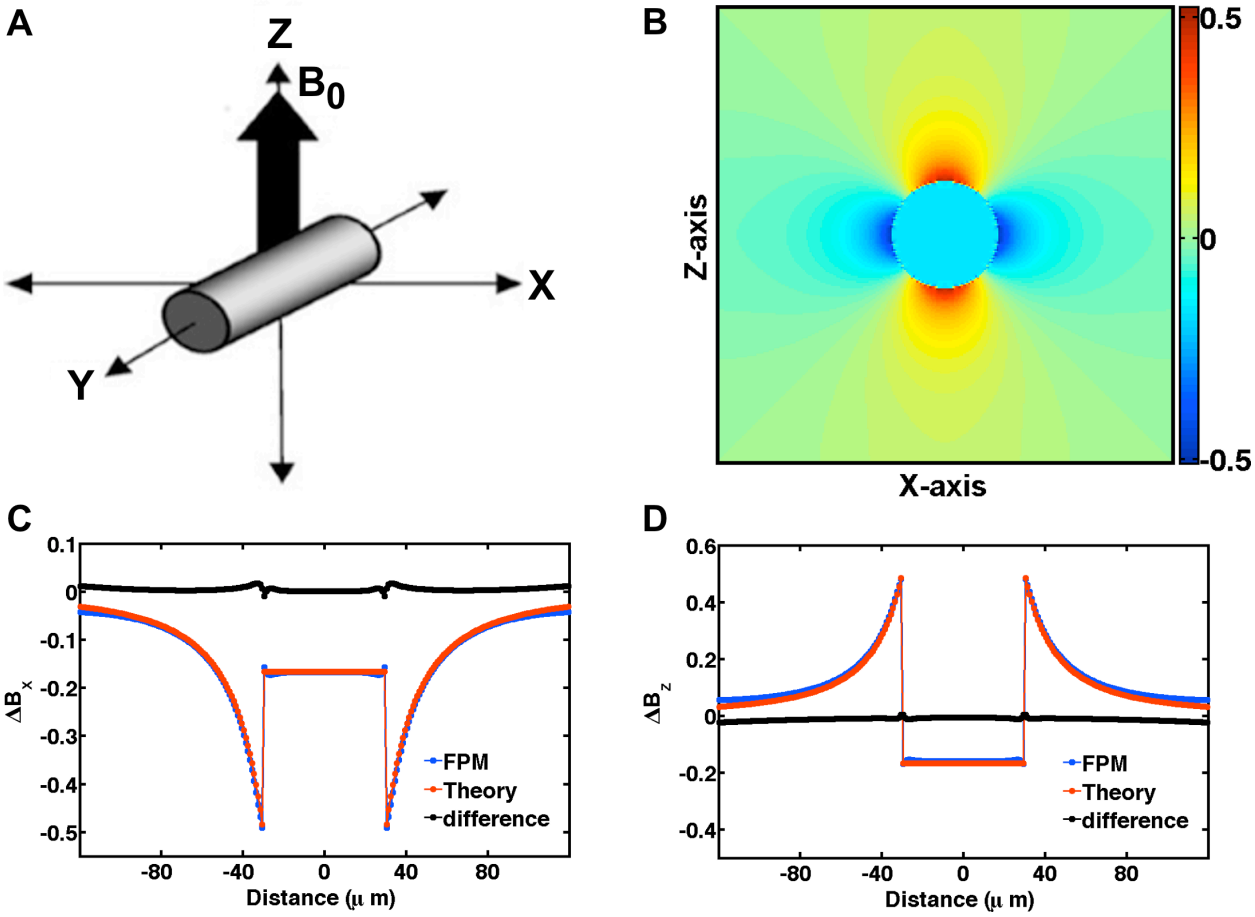

Figure 3.2: Validation of the FPM. (a) Illustration of the magnetic field and cylinder orientation. (b) 2D slice through the normalized magnetic field perturbation along a plane parallel to the XZ-plane. (c-d) FPM computed magnetic field shifts (blue) versus field shifts predicted by theory (red), and the difference between the two (black) plotted along the x-axis (c), and z-axis (d), respectively.

Table 3.1: Parameters used in MC and FPFDM simulations along with total computing times to calculate ΔR_2^* values for 18 cylinder radii.

Parameters	Meaning	Value
TE	Echo time	60 ms
Δt	Simulation time step	0.2 ms
$\Delta\chi$	Susceptibility difference	10^{-7}
B_0	Static magnetic field	1.5 T
V_p	Cylinder volume fraction	2%
D	Water diffusion coefficient	10^{-5} cm^2/s
N_s	Number of spins used in MC method	1000
$Time_{MC}$	Computing time for MC method	220 s
$Time_{FPFDM}$	Computing time for FPFDM	140 s

To further validate the accuracy of the FPFDM we also computed ΔR_2^* for simulated 3D cellular models consisting of packed spheres. Two packing conditions were considered: randomly distributed spheres and sphere packing on FCC gird. For each model, the sphere size was fixed at 9 μm radius corresponding to an approximate pertuber size where the SE relaxivity peaks and the GE relaxivity reaches plateau (45). The ΔR_2^* dependence on cell (sphere) volume fraction for the FPFDM was compared to that for the MC method (45) using similar simulation parameters. Fig. 3.3b compares the volume fraction dependence of ΔR_2^* for each of the two sphere packing techniques computed by both the MC and FPFDM, using $\Delta\chi = 5\times10^{-8}$, B_0 =1.5T, D = 10^{-5} cm^2/s, Δt = 0.2 ms, GE TE = 40 ms, and simulation universe size = (0.5 mm)^3. The FPFDM results were obtained by averaging the MR signal for 5 different sphere distributions for each packing and sphere volume fraction using a simulation grid size of 128^3. In contrast, the MC method involves tracking 15,000 random walks for each cell volume fraction and the redistribution of the spheres prior to each random walk. The FPFDM results are in excellent agreement to those produced from the MC methodology.

To investigate the convergence of the FPFDM for randomly distributed structures such as those used above, ΔR_2^* values obtained from (45) for vessel sizes of 10 μm and 15 μm were compared to the FPFDM results as a function of the number of structures used for averaging. Fig. 3.3c shows the percentage difference between the MC and FPFDM derived ΔR_2^* values. For both vessel sizes the computed FPFDM ΔR_2^* values converge to the corresponding reported values (45,51) to within 7% with only five structure averages. This percentage difference decreases to 0.8% as the number of averaged structures increases to 30.

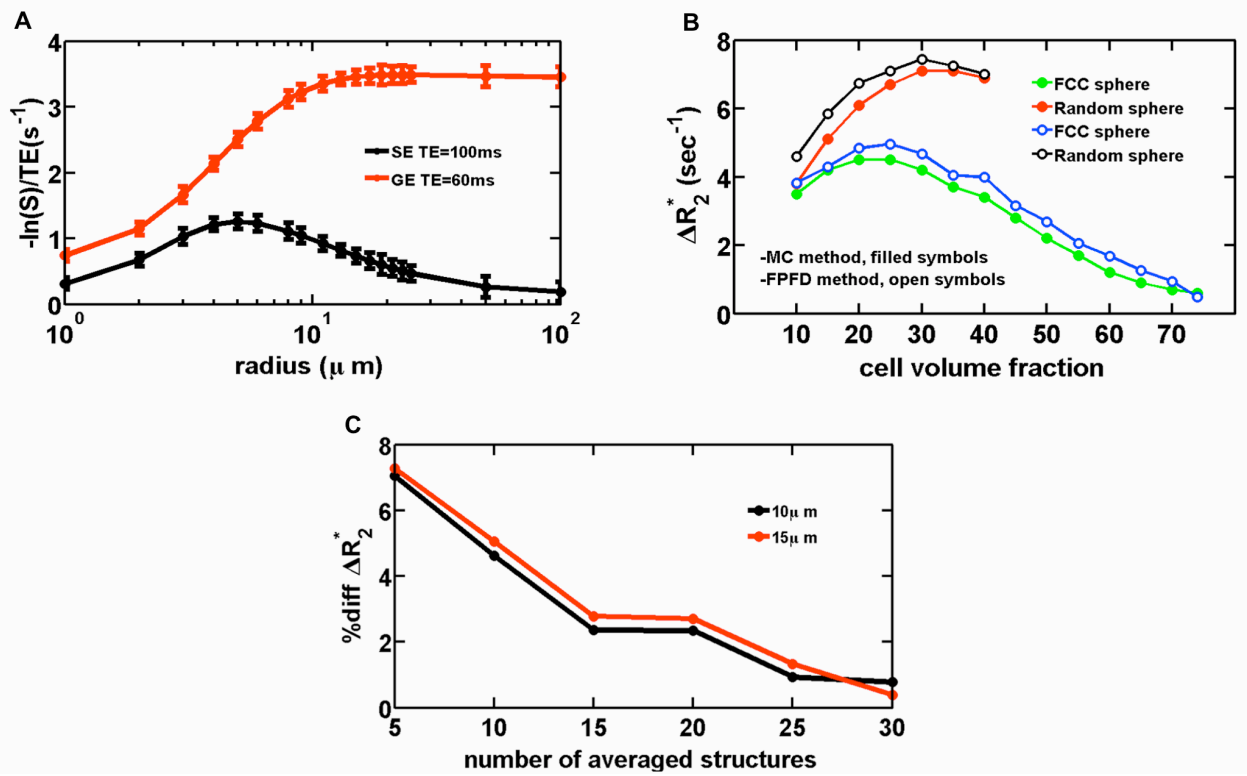

Figure 3.3: Validation of the FPFDM. (a) FPFDM replicates the characteristic vessel size dependence of ΔR_2^* and ΔR_2 as has been previously shown with MC methods. (b) A comparison of computed ΔR_2^* values as a function of sphere volume fraction and packing arrangement using MC (filled symbols) and FPFDM (open symbols) techniques, with excellent agreement between the two methods. (c) The computed ΔR_2^* percentage difference between MC and FPFDM decreases as the number of FPFDM structures used for averaging increases.

3.6 Modeling First-pass DSC-MRI Data in Brain Tumors using the FPFDM

To demonstrate the potential of the FPFDM to simulate DSC-MRI signals arising from the dynamic passage of contrast agent through the vascular and extravascular spaces, such as would occur in brain tumors with a breakdown of the blood brain barrier, we used the GE signal equation given in Eq. (2.8). The simplified form of the post-contrast to pre-contrast signal ratio can be written as:

$$\frac{S(t)}{S(0)} = \left[\frac{1-\exp\left(-TR\bullet R_{10}\right)\bullet\cos\alpha}{\left(1-\exp\left(-TR\bullet R_{10}\right)\right)\bullet\exp\left(-TE\bullet R_{20}^{*}\right)}\right]\bullet\left[\frac{\left(1-\exp\left(-TR\bullet R_{1}(t)\right)\right)\bullet\exp\left(-TE\bullet R_{2}^{*}(t)\right)}{1-\exp\left(-TR\bullet R_{1}(t)\right)\bullet\cos\alpha}\right] \qquad (3.14)$$

The first term in Eq. (3.14) is a constant that depends on pre-contrast tissue properties and imaging sequence parameters.While the first term can be calculated with relevant choice of pulse sequence parameters and the pre-contrast tissue longitudinal ($R_{10} = 1/T_{10}$) and transverse ($R_{20}^* = 1/T_{20}^*$) relaxation rates from previous studies, calculation of the second term in Eq. (3.14) requires the time evolution of the longitudinal ($R_1(t) = 1/T_1(t)$) and transverse ($R_2^*(t) = 1/T_2^*(t)$) relaxation rates caused by CA injection. Assuming a fast water exchange between the compartments the $R_1(t)$ can be expressed as (54,55):

$$R_1(t) = r_1 . C_t(t) + R_{10}, \tag{3.15}$$

where r_1 is the CA T_1 relaxivity and $C_t(t)$ is the tissue CA concentration and is estimated by the weighted average of the concentrations in the extravascular extracellular space (EES), vascular space and the intracellular space. Assuming the CA does not penetrate into the cells $C_t(t)$ takes the form:

$$C_t(t) = v_e C_e(t) + v_p C_p(t), \tag{3.16}$$

where v_e, C_e, v_p, C_p represent the volume fractions and CA concentrations of the EES and vascular space, respectively.

In addition to microscopic interaction effect, which can be described in a similar fashion as the longitudinal relaxation rate, the tissue transverse relaxation also depends on mesoscopic scale interactions. These additional effects arises due to susceptibility variation in the order vessel and cell sizes (56). Consequently, the tissue transverse relaxation rate can be expressed by:

$$R_2^*(t) = R_2^{micro}(t) + R_2^{meso}(t) + R_{20}^*, \tag{3.17}$$

where R_{20}^* is the tissue pre-contrast transverse relaxation rate. The microscopic term is calculated using:

$$R_2^{micro}(t) = r_2 . C_t(t), \tag{3.18}$$

where r_2 is the CA T_2 relaxivity and $C_t(t)$ is calculated using Eq. (3.16).

The mesoscopic relaxation rate has been shown to significantly depend on the geometry of the host tissue compartments (45,57-59). The qualitative and quantitative relationship between the mesoscopic effects and various tissue morphological parameters is the subject of Chapters 4 and 5. In this section the FPFDM is used to estimate this effect, which in turn allow us to calculate the DSC-MRI signal using Eq. (3.14).

To demonstrate the feasibility of using the FPFDM as a tool to simulate DSC-MRI signals in the presence of contrast agent extravasation and demonstrate the influence of extravascular features on DSC-MRI, we used two sample tissue structures composed of 60% cells and 4%

blood vessels. The two different tissue structures were constructed by packing ellipsoids with radii of 5μm and 15μm around a fixed fractal-based vascular network. The motivation for using ellipsoid and fractal based tissue structures along with details of their construction will be described in the next chapters. Sample arterial input function (AIF) with a criterion that is often observed in DSC-MRI studies was generated as previously described (60). The vascular (C_p) and EES (C_e) CA concentration time curves were computed using the pharmacokinetic two compartmental model described by Brix et al (61). The relevant input physiological, pulse sequence and physical parameters (e.g. blood flow, blood volume, contrast agent transfer coefficient, T_1, T_2, etc) were selected from values measured in previous MRI, PET and CT brain tumor studies as previously described (17). All concentration time curves were sampled using 150 time points for a total of 9 minutes and converted to susceptibility difference between compartments using $\Delta\chi = \chi_m$. [CA], where [CA] is compartmental CA concentration and χ_m is the CA molar susceptibility (0.027×10^{-6} mM^{-1}) (62).

Fig. 3.4a shows a sample 3D volume rendering of such a tissue structure, which contains ellipsoids of mean axis radii 15μm and vascular network with vessel size ranging from 5μm to 45 μm. The simulated C_p and C_e time curves are shown in (Fig. 3.4b). Fig. 3.4c shows a representative 2D slice through the computed magnetic field perturbations at a particular time.

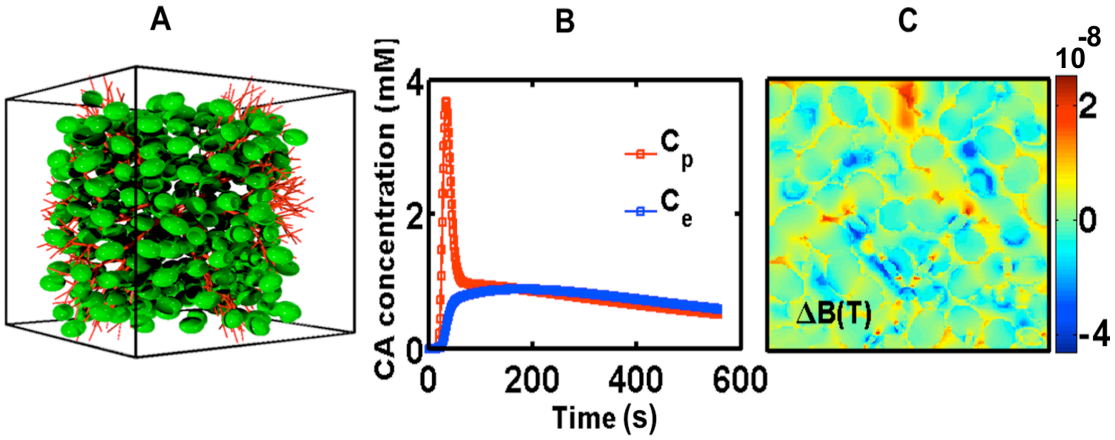

Figure 3.4: Example simulation with realistic tissue structure and contrast agent kinetics. (a) Sample tissue structure composed of ellipsoids packed around fractal tree based vascular network. (b) Simulated C_p and C_e curves derived using 2-compartment model. (c) Example 2D map through the magnetic field perturbation computed at time t=300 sec.

The simulated C_p and C_e curves along with model tissue structure, in Fig. 3.4, were used as an input to compute the dynamic DSC-MRI signal. Fig. 3.5 shows the GE post-contrast to pre-contrast DSC-MRI signal ratio time curves (S/S_0), both in the presence (K^{Trans} = 0.2 min^{-1}) and absence (K^{Trans} = 0 min^{-1}) of contrast agent extravasation. Fig. 3.5a-c show the time series for the tissue structure composed of ellipsoids with a 5μm mean radii, at pre-contrast longitudinal relaxation times values of T_{10} = 500 ms, T_{10} = 1000 ms and T_{10} = 1500 ms, respectively. The corresponding time series for the tissue structures modeled with 15μm cellular radii are shown in

(Fig. 3.5d-f). The following input parameters were used to compute the DSC-MRI signal: B_0 =3T, D = 1.3×10^{-5} cm^2/s, Δt = 0.2 ms, TE = 50 ms, TR = 1500 ms, flip angle $\alpha = 90^o$, pre-contrast transverse relaxation time $T_{20}^* = 50ms$. The CA T_1 and T_2 relaxivity values, r_1 and r_2, were set to 3.9 and 5.3 $mM^{-1}s^{-1}$, respectively (63). The compartmental membrane water permeability values were set at $P_m = 0$, to model restricted water diffusion. For a fixed cell volume fraction, the simulated time series demonstrate a marked cell size dependency. In general, for both tissue structures, as T_{10} increases from 500 ms to 1500 ms the influence of T_1 leakage effects becomes more substantial, as indicated by the increased signal recovery. For the small cell size structure, the T_1 leakage effects eventually result in a signal overshot from baseline (e.g. Fig. 3.5c). However, the structure constructed with larger cell sizes is dominated by T_2^* leakage effects (as apparent from the low signal recovery well after the CA's first pass) even at T_{10} = 1500 ms (Fig. 3.5f). The simulation time to compute the signal for 150 time points, for 3 T_{10} values, 2 contrast agent leakage conditions and 2 tissue structures was approximately 240 mins.

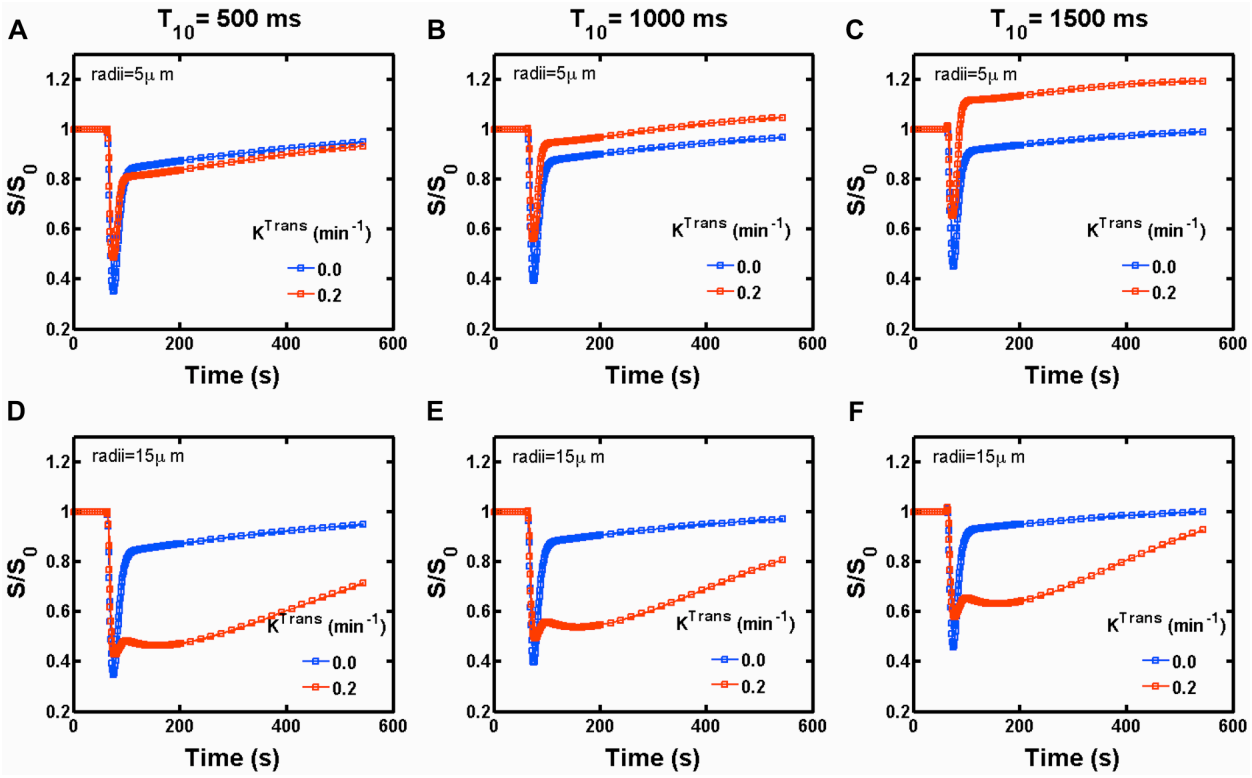

Figure 3.5: FPFDM derived DSC-MRI signals in the presence of CA leakage. The GE post-contrast to pre-contrast DSC-MRI signal ratio (S/S_0), both in the presence (K^{Trans} = 0.2 min^{-1}) and absence (K^{Trans} = 0 min^{-1}) of CA leakage at pre-contrast T_1 values of T_{10} = 500 ms, T_{10} = 1000 ms and T_{10} = 1500 ms, for tissue structures constructed using ellipsoids with mean radii of 5μm (a-c) and 15μm (d-f), respectively. The (S/S_0) values were computed using input parameters of B_0 =3T, D = 1.3×10^{-5} cm^2/s, Δt = 0.2 ms, TE = 50 ms TR = 1500 ms, $\alpha = 90^o$, $T_{20}^* = 50ms$, r_1 = 3.9 $mM^{-1}s^{-1}$, r_2 = 5.3 $mM^{-1}s^{-1}$ and $P_m = 0$.

3.7 Discussion

The FPFDM is a novel efficient computational tool combining features of the FP and FD techniques for calculating susceptibility-induced relaxivity changes for realistic simulated or imaging-based 3D vascular and cellular geometries that might be observed *in vivo*. The FPM can compute the induced magnetic fields around arbitrary microvasculature structures without necessitating any assumptions about the underlying vessel geometry (51). Although the Fast Fourier transform (FFT) improves the computational efficiency of the FPM for computing magnetic field perturbations, the application of MC techniques for tracking proton diffusion through the tissue in order to derive the resulting relaxivity change reduces its computational efficiency. The replacement of the MC component of FPM with matrix-based FDM can increase the computational efficiency by computing the evolution of the discretized magnetization simultaneously (53). The diffusion transition matrix A is either invariant or requires only partial updating for most tissues under consideration, further increasing the computing efficiency of matrix-based FDM that also benefit from optimized MATLAB packages for computations involving large matrices (53).

A Gaussian diffusion kernel convolution can also be used to model CA and water diffusion (64-66). This approach is computationally more efficient than MC approaches, but limited to unrestricted water diffusion. Although non-Gaussian diffusion, a consequence of tissue structure that creates diffusion barriers and compartments, could be modeled by adding a kurtosis term to the kernel, it is not clear how this will affect the slower diffusion process observed in the restricted CA diffusion model (66). Modeling restricted water diffusion using the MC method (51) or the Gaussian diffusion kernel approach (64-66) requires either incorporation of elastic collisions at membrane boundaries or neglecting proton diffusion steps that involve membrane crossing. Unlike the case of unrestricted water diffusion, using these later methods to model restricted water diffusion and/or water diffusion in complex tissue with different compartmental diffusion coefficients will require additional computations, thereby increasing the overall processing time. Given compartmental diffusion coefficients and membrane permeability values, the FPFDM can be used to model restricted water and CA diffusion and water exchange across compartments. For the FPFDM, including these additional structural features requires the computation of multiple versions of the diffusion transition matrix, A. Since A can be determined at the start of the simulation, a library of diffusion transition matrices, for a range of tissue structures, can be established to increase the computing efficiency. For example, computing a dynamic signal for the same structure only requires loading the transition matrix corresponding to the structure once from the library of diffusion transition matrices.

We validated the FPFDM in two ways. First, we replicated the vessel size dependence of ΔR_2^* and ΔR_2 (Fig. 3.3a) using identical simulation parameters to previously described MC and FP techniques (45,51). Next, we found excellent agreement for relaxivity from packed spheres across a range of packing densities and packing strategies using traditional MC technique versus FPFDM (Fig. 3.3b). The agreement between MC and FPFDM converges as the number of structures included in the average for the FPFDM increases (Fig. 3.3c). Unlike MC simulation, which tracks a large number of particles in the simulation or, equivalently, runs the same simulation many times to obtain an accurate average result, the FPFDM converges to the average result with only a few simulation runs. This behavior can be explained in the following way. In the MC simulation, a population of particles distributes in the whole system and the particles that encounter membranes within the complex tissue are only a small portion of all the particles such

that the echo signal does not contain sufficient enough information about the tissue features that restrict diffusion. Hence, to solve this problem, more particles are considered in the simulation or, equivalently, the same simulation is run many times to obtain an accurate average result. In contrast, the FDFDM determines the diffusion transition matrix at the start of the simulation, which already contains the tissue structural information and results in a faster convergence of the average signal.

For a simplistic structure containing randomly oriented cylinders with a total of 18 different radii, the FPFDM, as compared to MC, reduced the computation time to calculate ΔR_2^* values from 220 s to 140 s. For complex tissue structures, and under conditions of restricted water diffusion, the increase in computational efficiency afforded by the FPFDM will improve even further. In such cases, the MC method requires a larger number of spins and additional computation steps in order to converge and capture sufficient information about the tissue structure (67). In contrast, for these more complex structures, the FPFDM does not require additional computing time and is not limited by restricted water diffusion (53).

Although simulations in this study are based on a simple 2-compartment model, at the expense of computational time, the same approach to model water diffusion and exchange can be used to model CA diffusion and transport across compartments, yielding a more realistic heterogeneous CA distribution within a voxel. This can be achieved by updating CA concentration for each voxel/simulation grid at each simulation time step using a CA diffusion transition matrix (A_{CA}) calculated using appropriate CA diffusion coefficients and permeability across membranes from literature (68,69). For the purposes of this study, we assumed that the contrast agent equilibrates within each compartment over the time it takes to acquire each DSC-MRI image (1 – 2 seconds). Such an assumption is traditionally employed and consistent with current DSC-MRI analysis techniques.

The FPFDM also provides a computationally reasonable approach for simulating DSC-MRI derived transverse relaxation rates both in the presence and absence of CA extravasation, and restricted water diffusion induced by membrane permeability (Fig. 3.4 and Fig. 3.5). The results shown in Fig. 3.5 demonstrate that contrast agent leakage can lead competing T_1 and T_2^* effects as the CA traverses the extravascular extracellular space. For a given T_{10}, the structure with smaller sized cells exhibited higher signal intensity recoveries as compared to that with larger sized cells. The compartmentalization of CA around the larger cells creates stronger magnetic field perturbations and greater relaxation rate changes (T_2^* effects). In general, as T_{10} increases, T_1 leakage effects will be more pronounced and may dominate any T_2^* leakage effects, as is the case for the smaller-sized cells. In such cases, the characteristic signal overshoot may be observed (Fig. 3.5c). For the tissue structure with larger perturber sizes, the signal intensity exhibits less recovery due to the presence of substantial T_2^* leakage effects (Fig. 3.5d-3.5f). Given the clinical importance of DSC-MRI signal recovery characteristics to help differentiate among tumor types (70,71), a systematic *in silico* study of DSC-MRI signal recovery and its dependence on physiological, pulse sequence and physical parameters is currently under investigation.

One of the limitations of the FPM is the use of FFT to calculate the spatial convolution of the vascular structure with the finite perturber magnetic field perturbation. As demonstrated in (51) the resulting field perturbation is equivalent to the field perturbation from a periodic array of the tissue structure under consideration. Although realistic tissue structures extend beyond the boundary of the simulation space, which introduces a "boundary problem", we used zero-padding of the tissue structure to avoid additional field perturbation at the boundaries from the

neighboring array. The padding size to eliminate boundary field effects depends on the perturber size and the tissue structure. Here we used a zero-pad size of one-tenth of the simulation box, since the field perturbation changes we observed by using higher zero-pad sizes were negligible.

The FPM was designed to compute the magnetic field changes from a single finite perturber convolved with a digitized tissue structure array, and hence this approach cannot be used for arbitrary magnetic susceptibility distributions. While methods capable of computing arbitrary susceptibility distributions are more comprehensive and should be explored (72,73) , it is typically assumed that contrast agent instantaneously distributes within each tissue compartment (e.g. intravascular and extravascular extracellular space) at each imaging time point. Accordingly, the FPFDM is a practical approach to compute field perturbations arising from tissue structure with only a few susceptibility compartments, such as the intravascular, intracellular, and extravascular extracellular spaces.

The sampling of tissue structures at higher resolution increases the computational accuracy of the FPM but it comes at the expense of computational time. Such increases in resolution would also add to computational time needed to compute the MR signal using the FDM. This is particularly true if a need arises to reduce the simulation time step (Δt) due to increased resolution or decreased perturber size (Δx), in order to satisfy the constraint that the jump probability (see Eq. 3.7) should be $\leq 1/6$. This is because when the number of spins leaving a given node exceeds the number that was present, the FDM becomes unstable (52). With the parallel high-performance computing techniques we previously developed (53), we are exploring ways to increase the computational efficiency of the FPFDM at higher resolutions so that we can more accurately characterize fine tissue microstructure across a broader range of structural dimensions (e.g. a few microns up to a hundreds of microns).

3.8 Conclusion

The FPFDM is an alternative computational tool for efficiently modeling susceptibility induced MR signal relaxation from complex perturber geometries. In general, the proposed FPFDM could be used to investigate the influence of realistic tissue microstructure on any susceptibility based contrast mechanism such as vessel size imaging, BOLD contrast, single cell imaging, and quantitative susceptibility mapping. The proposed method has been used and will continue to be utilized to assess the influence of geometrical, morphological and physiological parameters of microvessels and cells on susceptibility induced MR relaxation rate changes. Such studies should shed new insights into DSC-MRI contrast mechanisms and enable the systematic evaluation of how acquisition and analysis methods influence the measurement of reliable perfusion parameters in brain and tumor tissue.

CHAPTER 4

THE INFLUENCE OF VASCULAR MORPHOLOGY ON DSC-MRI DERIVED BLOOD VOLUME MEASUREMENTS IN BRAIN TUMORS

A central assumption in all DSC-MRI studies is that a linear relationship, with a spatially uniform rate constant, termed the vascular susceptibility calibration factor (k_p), exists between the CA concentration and the measured transverse relaxation rate change. Given the dependence of susceptibility field gradients on vascular geometry, this assumption could significantly impact the reliability of DSC-MRI hemodynamic measurements. Tumor vascular structures are known to be fundamentally different from normal vasculature (74-76). Whereas vascular networks in normal tissue are highly ordered, those found in tumors are abnormally heterogeneous, with a large degree of random variation in vessel length, diameter and branching patterns. In this computational study, we investigate the influence of vascular morphology on DSC-MRI derived blood volume measurements and characterize the vascular susceptibility calibration factor for simulated vascular tree networks that replicate structural properties observed in normal and tumor tissue. In addition to simulated vascular structures attempts were made to characterize k_p values for MR size voxels obtained from micro-CT based renal angiograms.

4.1 Vascular Network Model

In order to provide a framework that mimics in vivo conditions but also enables the systematic investigation of the influence of vascular features on DSC-MRI data we explored the use of fractal tree based vascular networks (77,78). Starting with an initial cylindrical segment representing an arterial vessel, the vascular tree was created using successive bifurcation into smaller daughter segments until a target vascular volume fraction is reached to terminate the fractal tree development. At each bifurcation junction the diameter of each daughter vessels was calculated using Murray's law (79). The idea of Murray's model is based on the principle that naturally occurring vascular networks must achieve an optimal arrangement that minimize the biological work needed to maintain blood flow. According to Murray's law, at each junction (Fig 4.1a) the reduction of parent diameter (D_0) to daughter diameters (D_1, D_2) is given by:

$$D_0^x = D_1^x + D_2^x, \tag{4.1}$$

where x is called the bifurcation exponent. Large number of studies based on human and animal organs has been shown to support the Murray's power law with scattered values of the exponent x ranging from 2 to 3 (78,80-86). For capillaries and small vessels the value of x is shown to be close to 3, consequently in this study x is set at 3 and kept constant across tissue (81,87).

An important morphological parameter that describes the symmetry of the daughter vessels is the bifurcation index (λ), calculated using the ratio of the narrower to the wider daughter vessel diameters at each junction ($\lambda = D_1/D_2$). Previous experimental studies in animals have shown bifurcation index values ranging from 0 to 1 (88,89). For a given λ and D_0, Eq. (4.1) was used to

calculate the daughter diameters at each bifurcation node. The ratio of the daughter to parent vessel length at a given junction provides another morphological parameter termed the scale factor ($\alpha = L_1/L_0 = L_2/L_0$). Values of α ranging from 0.7 to 0.9 has been observed in previous animal studies (89).

The two branching angles θ_1, the angle between a parent and daughter 1, and θ_2, the angle between daughter 2 and parent (Fig 4.1a), considerably influence the geometry of the vascular network. The rotation angles Φ_1 and Φ_2 are the azimuthal angles of the two daughters with respect to the parent cylindrical axis (Fig 4.1a).

Given the initial feeding artery (L_0 and D_0) and morphological parameters at each junction such as, λ, θ_1, θ_2, Φ_1,Φ_2, and α, using Eq. (4.1) the diameter and length of each cylindrical segment required to build the target vascular network can be calculated. The diameters and lengths (the spatial coordinates of the two end points) of each building segment are then used to construct a binary tissue structure to be used as an input in the FPFDM. Figure 4.1b shows an isosurface plot of an example binary tissue structure sampled with 128^3 cubes of size 3.9 μm.

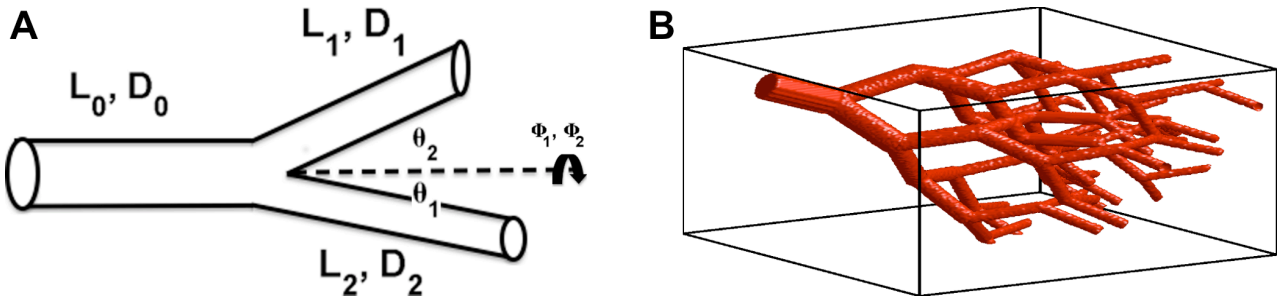

Figure 4.1: Morphological parameters of fractal based vascular network. (a) Illustrates the physical parameters used in the vascular model. L_0 and D_0 represent the parent vessel. (L_1, D_1, θ_1, Φ_1) and (L_2, D_2, θ_2, Φ_2) represent the upper and lower daughter vessels, respectively. (b) Sample binary vascular tissue structure constructed using uniform morphological parameters across tissue.

4.2 The Effects of Vascular Network Heterogeneity on ΔR_2 and ΔR_2^*

To investigate the effect of vascular geometry variation on DSC-MRI derived ΔR_2 and ΔR_2^* values, we used fractal-based tissue models to represent the complex geometries of the microvasculature as input to the FPFDM. Fig. 4.2 illustrates the effect of branching angle heterogeneity ($\Delta\theta$) on the CA concentration dependence of ΔR_2 and ΔR_2^* for typical DSC-MRI contrast agent concentrations. For these simulations we generated three different vascular networks within a 1 mm^3 volume sampled with 128^3 voxels. Fig. 4.2a-4.2c shows sample vascular trees constructed using homogenous λ, Φ_1,Φ_2, and α values at each branching node, but with increasing heterogeneity in branching angles θ_1 and θ_2. The model for normal vasculature is shown in Fig. 4.2a, with branching angles at each junction chosen randomly from a narrow range

of 25°–40°. To represent the tortuous and chaotically organized morphology of tumor vessels, the range of branching angle heterogeneity were increased to 25°–80° (Fig. 4.2b) and 25°–140° (Fig. 4.2c). Fig. 4.2d shows three orthogonal 2D slices through the body center of the magnetic field perturbations computed using the FPM for the vascular structure in Fig 4.2c. Fig. 4.2e and 4.2f plot the concentration dependence of ΔR_2^* and ΔR_2 for the three θ heterogeneities (Δθ) considered. For these simulations we used, $\Delta\chi = \chi_m$. [CA], B_0 = 4.7T, D = 10^{-5} cm^2/s, Δt = 0.2 ms, GE TE = 40 ms and SE TE = 80 ms. All simulated vascular structures incorporate vessel radii ranging from 12 μm to 80 μm with a 2% target vascular volume fraction (v_p). The computed relaxation rates were averaged over five different orientations for each simulated vascular network. Using the slope of the ΔR_2^* dose response curves, k_p values ranging from 100-295 $(mM\text{-}sec)^{-1}$ were obtained. The k_p values for the more tumor-like vascular trees (higher Δθ) were higher than those in normal trees, up to three fold for this simplified simulation. Similar dependency on branching angle with a reduced susceptibility effect was observed for ΔR_2 dose response curves.

4.3 The Effects of Vascular Morphology on DSC-MRI Derived Blood Volume

To investigate the effects of assuming uniform values of k_p across voxels when measuring rCBV we created tissue structures representing normal and tumor like vascular trees. Normal vascular trees were created using a volume fraction of 2.5%, while a range of volume fractions (4%, 8% and 12%) were used for tumor structures. For each vascular volume fraction considered here two sets of tumor structures were simulated. In the first set of tumor structures, heterogeneity was introduced by increasing branching angle variability (choosing θ_1 and θ_2 randomly from a range of 25° to 140°), while bifurcation index heterogeneity (λ taken randomly from a range of 0.5 to 1) was used to construct the second set of tumor vascular structures. Example 3D rendering of tissue structures representing normal and tumor vascular structures modeled using θ and λ heterogeneity are shown in Fig. 4.3. In order to compute rCBV for each vascular volume fraction a representative C_p time course was simulated as previously described in section (3.6). The simulated C_p time course and the tabular tissue structures along with $\Delta\chi = \chi_m$. C_p, B_0 = 3T, D = 10^{-5} cm^2/s, Δt = 0.2 ms, GE TE = 40 ms were used as an input to the FPFDM to compute the corresponding ΔR_2^* time courses for each tissue structure. The area under the computed ΔR_2^* time courses was used to calculate CBV values for the normal and tumor structures. Consistent with the common DSC-MRI practice Eq. (2.11), the rCBV values for each tumor tissue is computed using the ratio of the tumor to normal tissue CBV values (CBV_{tum}/CBV_{nor}), and compared with the actual tumor to normal tissue v_p ratios ($v_{p,tum}/v_{p,nor}$). To determine if differences between the computed rCBV values and the actual v_p ratios were due to k_p variation, the k_p values for each structure were first normalized to the tissue v_p and then computed using the slope of a linear regression fit of ΔR_2^* versus CA concentration.

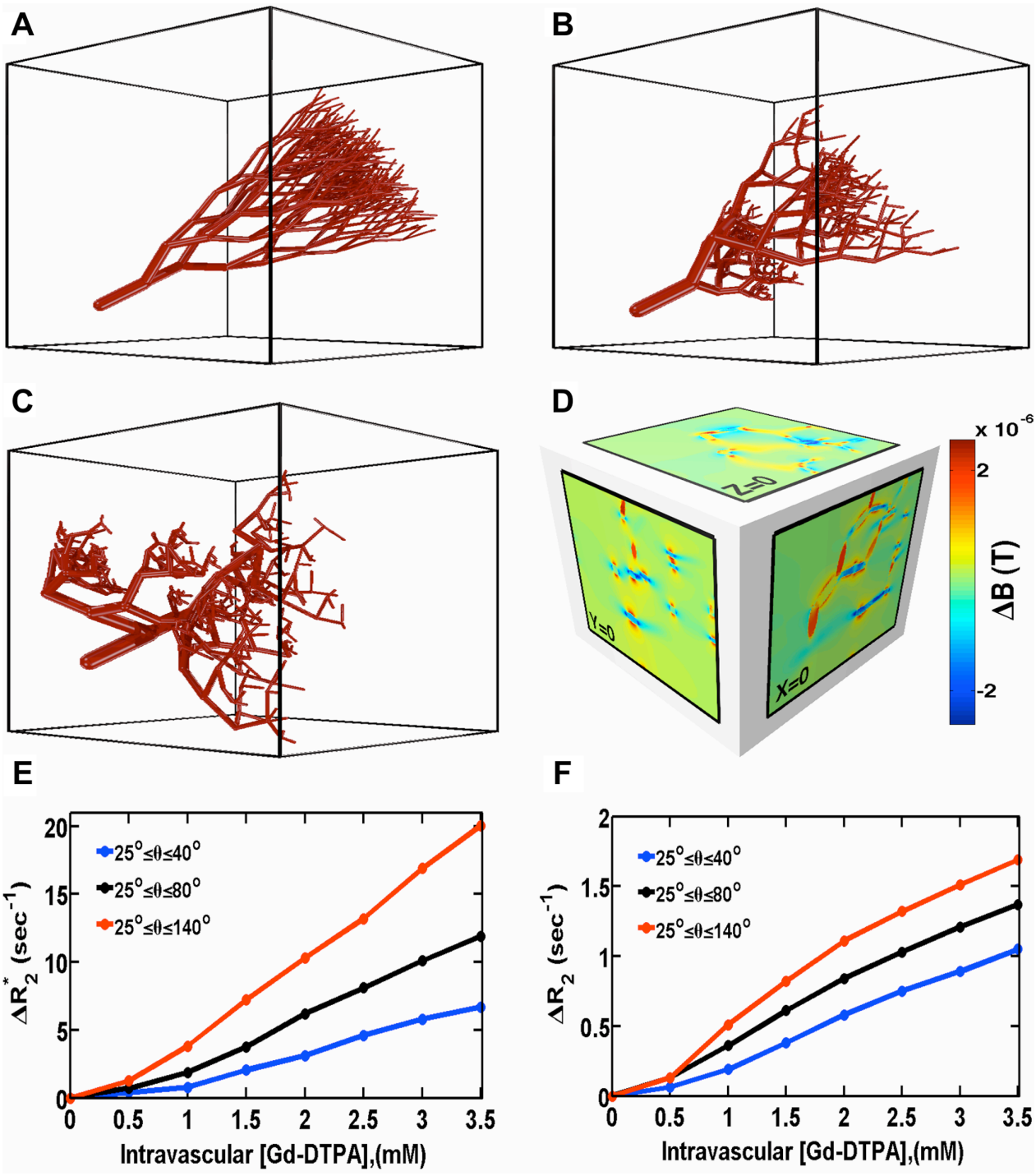

Figure 4.2: The influence of vascular morphology on ΔR_2^* and ΔR_2. (a-c) Sample microvascular networks simulated using a fractal tree model with increasing branching angle heterogeneity. (d) Three orthogonal slices through the magnetic field perturbation at the body center for the vascular network in (c). (e-f) Effect of branching angle heterogeneity on the concentration dependence of ΔR_2^* and ΔR_2 computed with FPFDM (B_0 = 4.7T, v_p = 2%, GE TE = 40 ms, and SE TE = 80 ms). Both ΔR_2 and ΔR_2^* increase with branching angle heterogeneity.

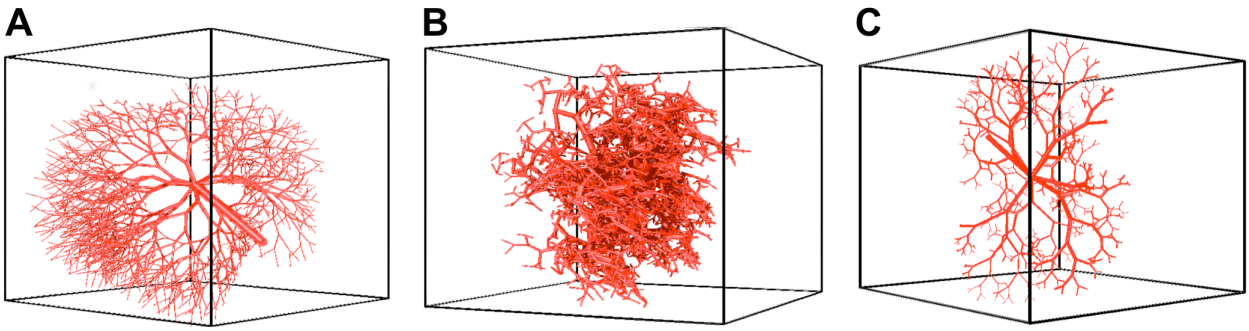

Figure 4.3: Sample normal and tumor like vascular networks. (a) Example normal microvascular networks simulated using homogenous morphological parameters. Tumor microvasculature modeled using, branching angle heterogeneity (b), and bifurcation index heterogeneity (c).

The computational results shown in Fig. 4.4 are for tumor tissue structures obtained by introducing branching angle heterogeneity. Figure 4.4a shows the computed ΔR_2^* time courses for three tumor tissue structure and one normal tissue representing a reference region. The corresponding computed rCBV values (CBV_{tum}/CBV_{nor}) along with the actual vascular volume fraction ratios ($v_{p,tum}/v_{p,nor}$) for the three tumor structures are shown in Fig. 4.4b. For all tumor tissues, the rCBV overestimates the actual vascular volume fraction ratio and as the tumor vascular volume fraction increases the difference between the computed rCBV and the actual vascular volume fraction ratio increases from 6.9% to 21.3%. The dose response of the computed ΔR_2^* values for each tissue structure is shown in Fig. 4.4c. The ratio of the tumor to normal tissue vascular susceptibility calibration factors ($k_{p,tum}/k_{p,nor}$) estimated using a linear fit to the data in Fig. 4.4c is greater than 1 for all tumor tissue as shown in Fig. 4.4d. This indicates that disparities between normal and tumor tissue branching angles will lead to an overestimation of rCBV when a spatially invariant k_p value is assumed.

The corresponding simulation results for tumor tissue structures constructed by increasing bifurcation index heterogeneity are shown in Fig. 4.5. Unlike the overestimated rCBV values found for branching angle heterogeneity, the, rCBV values computed for tumor structures with heterogeneous bifurcation indices underestimate the actual vascular volume fraction ratio and to a greater degree, with the differences ranging from 2.7% to 74.3%. As expected the ratio ($k_{p,tum}/k_{p,nor}$) is less than 1 for each tumor tissue, Fig. 4.5d. Whereas a greater distribution of branching angles led to an overestimation of rCBV, bifurcation index heterogeneity results in an underestimation of rCBV for tumor tissue.

In general increasing branching angle heterogeneity tended to increase tumor k_p values, whereas increasing bifurcation index heterogeneity decreased k_p, with the latter effect being more predominant. It is of note that the difference in normal and tumor k_p values for the bifurcation index heterogeneity case, with a 12% blood volume fraction, agrees closely with previously reported in vivo data in 9L brain tumors (36).

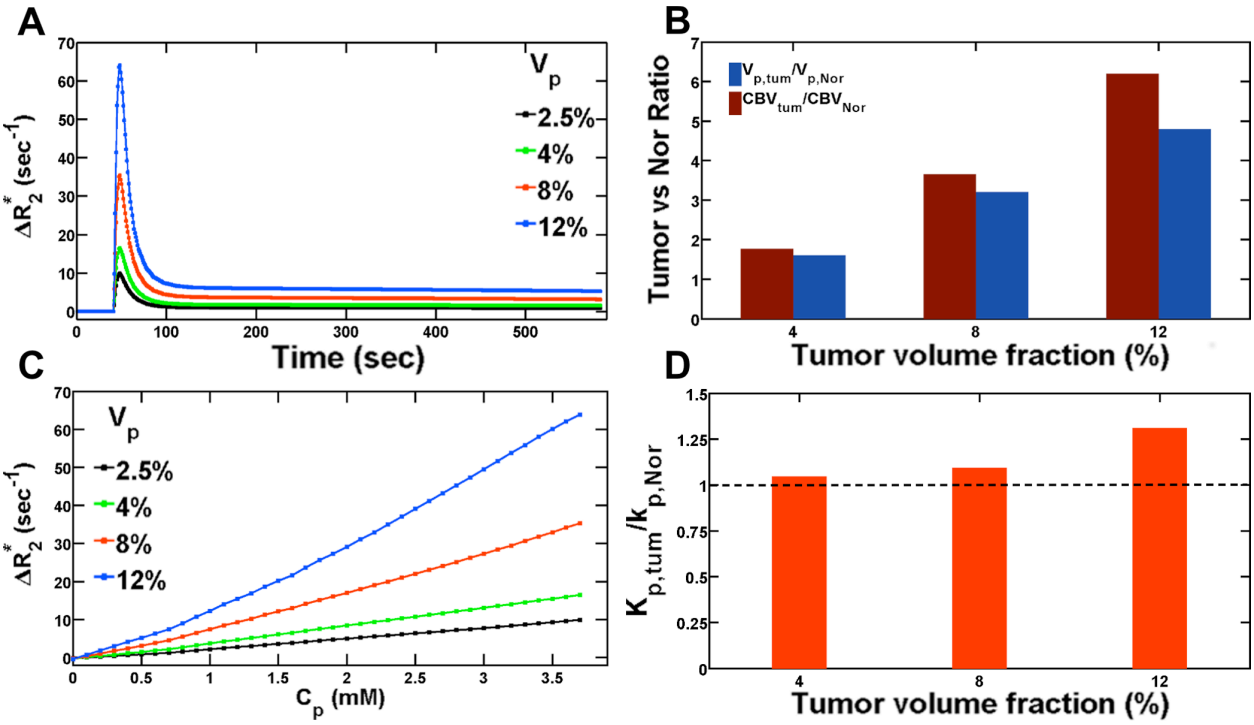

Figure 4.4: The influence of branching angle heterogeneity on rCBV. (a) ΔR_2^* time courses computed for one normal tissue vascular model (2.5%) created by randomly choosing branching angles from a narrow range ($25^o < \theta < 40^o$), and three tumor vascular models (4%, 8%, and 12%) created by randomly choosing branching angles from a wider range ($25^o < \theta < 140^o$), in order to increase branching angle heterogeneity. (b) Actual ($V_{p,tum}/V_{p,nor}$) and computed (CBV_{tum}/CBV_{nor}) tumor to normal blood volume ratios. The computed blood volume ratios overestimate the actual ratios. (c) The linear dependence of ΔR_2^* on CA concentration is used to calculate k_p values for each tissue. (d) The ratio of the tumor to normal tissue vascular susceptibility calibration factors ($k_{p,tum}/k_{p,nor}$) , suggests tissue structures with higher branching angle heterogeneity tends to have greater k_p values, which explains the overestimation in (b). All k_p estimates are normalized to the tissue v_p value.

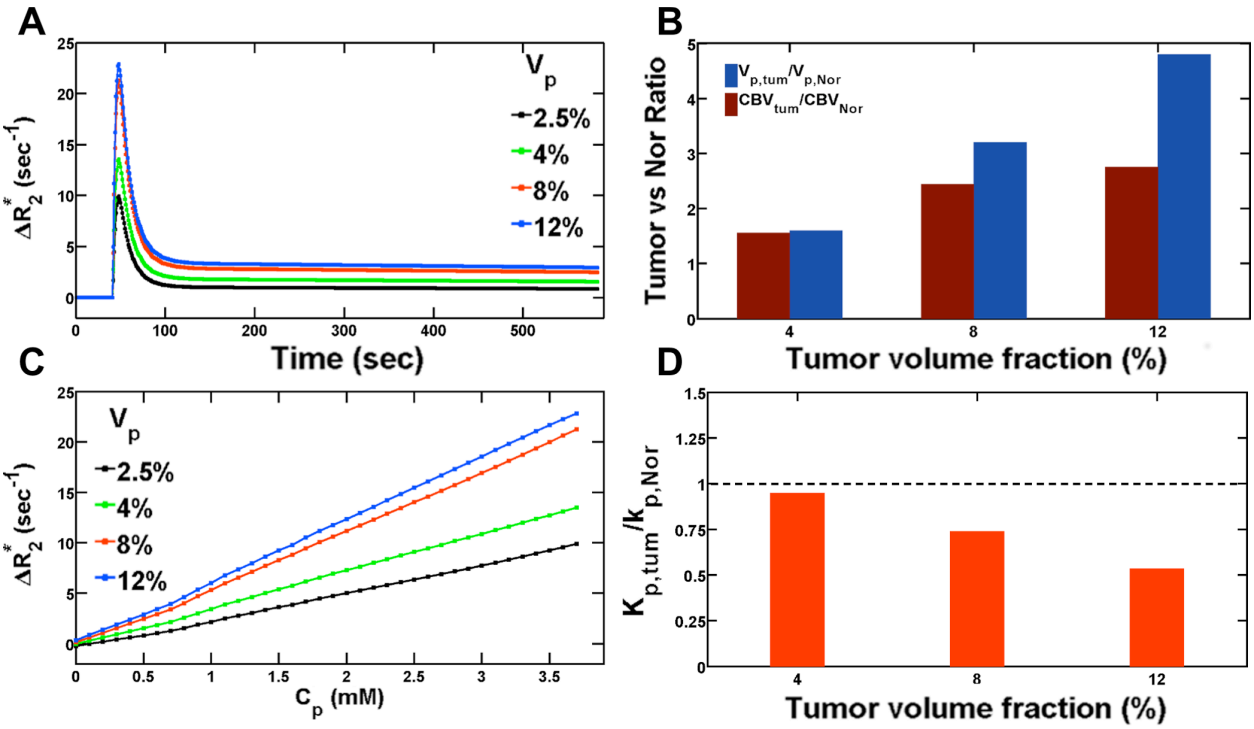

Figure 4.5: The influence of bifurcation index heterogeneity on rCBV. (a) ΔR_2^* time courses computed for one normal tissue vascular model (2.5%) created by using homogenous bifurcation index ($\lambda = 1$), and three tumor vascular models (4%, 8%, and 12%) created by randomly choosing bifurcation index values from ($0.5 < \lambda < 1$), in order to increase bifurcation index heterogeneity. (b) Actual ($V_{p,tum}/V_{p,nor}$) and computed (CBV_{tum}/CBV_{nor}) tumor to normal blood volume ratios. For each tumor tissue the computed blood volumes ratio underestimates the actual ratio. (c) The linear dependence of ΔR_2^* on CA concentration is used to calculate k_p values for each tissue. (d) The ratio of the tumor to normal tissue vascular susceptibility calibration factors ($k_{p,tum}/k_{p,nor}$), indicates tissue structures with higher bifurcation index heterogeneity tends to have lower k_p values, leading to the underestimation observed in (b). All k_p estimates are normalized to tissue the tissue v_p value.

4.4 Caracterizing k_p Heterogeneity using Image-based Tissue Structures

To investigate k_p variation across tissue structures and further illustrate the versatility of the FPFDM, micro-CT was used to create a three-dimensional rendering of a murine kidney vasculature perfused with Microfil (MV-122, Flow Tech). Following perfusion and fixation in 10% neutral buffered formalin, the kidney was scanned in a microCT50 (Scanco Medical AG, Brüttisellen Switzerland). Cross-sectional images of the entire kidney were acquired with an isotropic voxel size of 5.0 μm using an energy of 55 kVp, 200 μA intensity, 700 msec sample time, and 1000 projections per rotation using the manufacturers 1200 mg HA/ccm beam hardening correction algorithm in a 10.24 mm field of view. Using the manufacturer's software, we assembled individual slices into a z-stack and contrast-filled vessels were segmented from

soft tissue by applying a threshold of 260 mg HA/ccm (determined by calibration against a hydroxyapatite phantom) and a three-dimensional Gaussian noise filter with sigma 2.3 and support of 4. The resulting binary three-dimensional images of the perfused mouse kidney vasculature (1242 slices with 1428 × 1012 matrix size and 5 μm isotropic voxels) were used as source data for multiple 1 mm^3 vascular models with 200^3 finite cubic perturbers, each 5 μm in size. The 1 mm^3, MR voxel size, vascular models were prepared using in-house Matlab codes (Mathworks, Natick, MA) and used as an input for the FPFDM simulation.

Fig. 4.6 shows the entire extracted kidney vascular structure, with sample MR voxel-sized sub-structures and their respective vascular volume fractions. Figs. 4.7a and 4.7b show the FPFDM derived SE and GE k_p values obtained from the slope of the ΔR_2 and ΔR_2^* dose response curves, respectively. These results are normalized to the vascular fractional volumes and were computed using B_0 = 4.7T, D = 10^{-5} cm^2/s, Δt = 0.2 ms, GE TE = 40 ms, SE TE = 80 ms, and a clinically relevant range of $\Delta\chi$ values ranging from 0 to 9.4×10^{-8}, corresponding to a Gd-DTPA concentration ranging from 0 to 3.5 mM. In general, the SE and GE k_p values were highest for low vascular volume fractions and tended to decrease as the vascular volume fraction increased, with SE and GE k_p values ranging from 3.6 - 27.8 and 53.8-174.3 $(mM\text{-}sec)^{-1}$, respectively.

4.5 Discussion and Conclusion

In this chapter we describe a fractal tree based approach for generating more realistic, three-dimensional vascular tissue structures that can be used for the systematic investigation of DSC-MRI signal dependence on vascular morphology. We computed the contrast agent concentration dependence of transverse relaxation rates for vascular trees. Our results demonstrate the feasibility of using FPFDM for complex geometries, and suggest that although the generally accepted linear relationship between relaxation rate and CA concentration is reasonable, the proportionality constant k_p depends upon the microvascular geometry, a finding that is consistent with previous studies (45,51,90). The higher relaxation rate for vascular structures with greater range of branching angles is most likely due to the greater heterogeneity of vessel branch orientation with respect to B_0 and their larger space occupancy which impacts the frequency offset of a larger volume compared to narrow branching angles that pack vessels in a small region (Fig. 4.2). This is also consistent with the overestimation of tumor relative blood volume, observed when the tumor vascular structure is modeled by introducing branching angle heterogeneity compared to the reference region normal tissue (Fig. 4.4). On the other hand, the lower k_p values for tumor vascular structures with greater bifurcation index heterogeneity (Fig. 4.5), is most likely due to a larger number of small vessels, which induces smaller relaxation rate changes compared to the relatively larger vessels in the normal tissue due diffusion narrowing. These preliminary computational results show marked k_p heterogeneity across vascular networks, suggesting that further work is needed to better characterize the influence of vascular heterogeneity on DSC-MRI derived perfusion parameters in brain tumors.

Traditionally, randomly oriented cylinders were used to investigate the influence of vascular properties (e.g. vessel size, vessel volume fraction) on relaxation rates. Fractal-based vascular trees better approximate the microvascular network in vivo, but this complex geometry with variable vessel rotation, size distribution, branching angles, and diameters of daughter vessels is very difficult to model and require high resolution to achieve structural details. The high resolution required to sufficiently capture the fine detail of tissue microvasculature significantly

reduce the computing efficiency of the FPFDM. Currently a parallel computing technique to decrease the computing time to a feasible level is being investigated. This will allow more systematic studies for wide range of morphological, physiological and pulse sequence parameters to investigate the preliminary findings presented here.

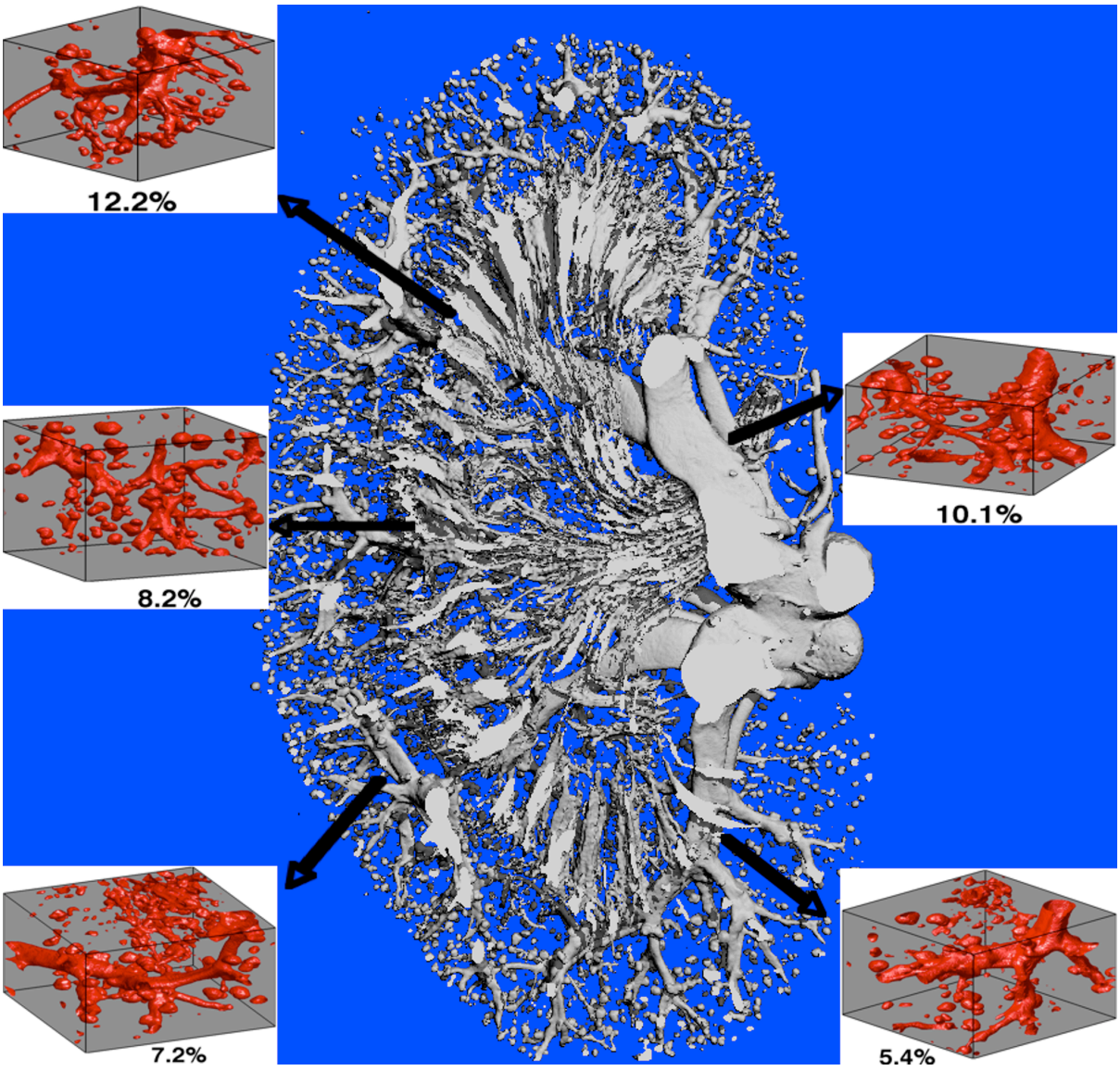

Figure 4.6: Kidney vascular structure extracted from micro-CT. Kidney vasculature extracted from micro-CT along with representative MR voxel-sized (1 mm^3) microvascular models taken from different sections of the kidney vasculature with their respective vascular volume fractions. The existence of the bubble-like structures demonstrates the filling of glomeruli with Microfil but a higher resolution would be required to differentiate the individual capillaries.

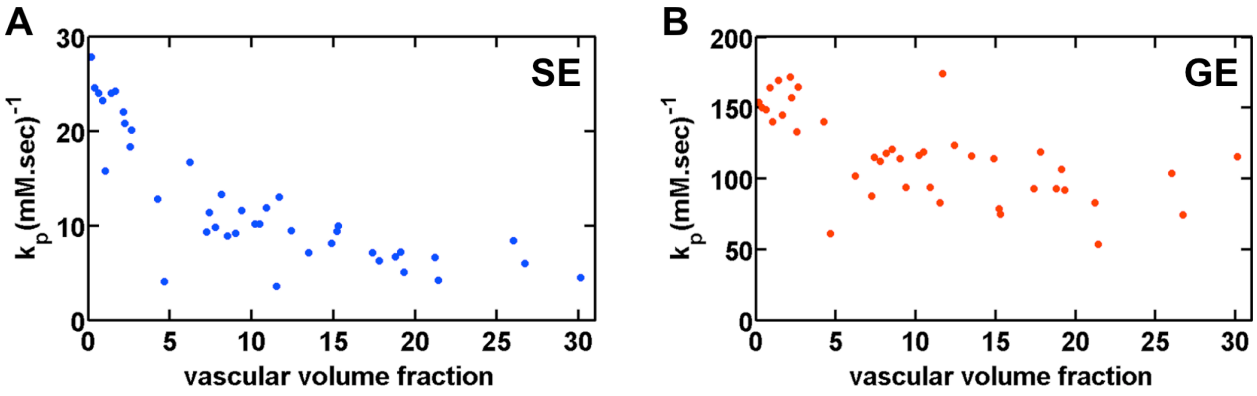

Figure 4.7: Computed k_p values for vascular structure extracted from micro-CT. (a) SE and (b) GE k_p values as a function of vascular volume fraction computed using the FPFDM for the kidney microvascular models (with vascular volume fractions > 0.1%) shown in Fig. 4.5. SE k_p values ranged from 3.6-27.8 (mM-sec)$^{-1}$, and GE k_p values ranged from 53.8-174.3 (mM-sec)$^{-1}$. Above 5% volume fraction, the GE k_p values were relatively constant with a mean value of 103.3(mM-sec)$^{-1}$.

The systematic evaluation of fractal-based vascular trees using the FPFDM could shed new insights into the relationship between DSC-MRI relaxation rate and vascular geometry. Furthermore, the use of fractal trees enables the application of well-established flow models (91-93) such that contrast agent kinetics and the associated DSC-MRI time series can be considered for each vascular structure. This would enable a more rigorous investigation of DSC-MRI-based voxel-wise measures of vessel size, transit time and flow distributions and oxygen extraction. Realistic 3D vascular and flow models could then be expanded to incorporate the extravasation of contrast agent and its subsequent diffusion around cells in the extravascular space. Such expansions would create a powerful framework with which to investigate DSC-MRI and susceptibility-based imaging methodologies in brain, tumors and other organs of the body.

Prior studies have shown the potential and value of incorporating image-based vascular structures into susceptibility simulations (64). Similar to these previous studies we sought to demonstrate the versatility of the FPFDM and k_p heterogeneity across vascular networks by determining the dose-response of relaxation rates for vascular structures derived from *ex vivo* micro-CT scans of perfused kidney vasculature. The dose-response curves from MRI voxel-sized regions of the kidney vasculature were used to determine the distribution of vascular susceptibility calibration factors, k_p, within the kidney. For vascular volume fractions up to 30%, k_p values were very heterogeneous (Fig. 4.7), with decreased heterogeneity for vascular volume fractions greater than 5%. The k_p decreased over vascular volume fractions between 0 and 5% with a slower decrease above 5%, consistent with a previous study in rodent brain that found grey matter k_p to be nearly twice that of tumor (36). It should be noted that the kidney microvascular structure presented in this study is limited by the spatial resolution of the micro-CT data. With a 5 mμ resolution individual capillaries could not be resolved and capillary dense regions, such as in the glomeruli, present as a single large perturber. The differentiation and inclusion of these capillaries will likely influence the overall k_p heterogeneity across voxels for both SE and GE computations. For the purposes of this study, this example illustrates the ability

of the FPFDM to explore susceptibility contrast and k_p heterogeneity in tissue structures acquired using *ex vivo* imaging modalities. As the FPFDM only requires that structures consist of a digital format it could accept structural input from any imaging modality (e.g. optical, CT, electron microscopy, MRI).

In conclusion, the preliminary computational results presented herein show marked k_p heterogeneity across vascular networks, suggesting that the assumption of a constant k_p for all tissue types could affect DSC-MRI derived perfusion parameters. However, it is encouraging that morphological features can both increase and decrease tumor k_p values, as this may suggest that the net effect in vivo is less substantial than observed herein due to averaging. While k_p heterogeneity may have little clinical impact on identifying highly vascular tumors it could affect the interpretation of serial DSC-MRI data during treatment response. Anti-angiogenic agents are known to significantly modify the tumor microvasculature (94,95), which, in turn, could serially alter k_p values. Further studies are needed to explore such effects and suggest the need to validate serial DSC-MRI measurements of tumor hemodynamics.

CHAPTER 5

MODELING THE EFFECTS OF CONTRAST AGENT EXTRAVASATION ON DSC-MRI

In normal brain regions, the biophysical basis of DSC-MRI signal is well characterized, primarily reflecting the underlying contrast agent kinetics and vascular geometry (45). When the BBB is disrupted, as is often in tumor regions, small molecular weight contrast agents, such as Gadolinium-Diethylenetriaminepentaacetic Acid (Gd-DTPA) may extravasate, leading to dynamic changes in the tissue T_1, T_2 and T_2^* relaxation times. In such cases, DSC-MRI signals are more complex and depend on hemodynamics, vascular geometry and permeability, the extravascular microstructure and the applied pulse sequence (17-19). When DSC-MRI signals are acquired and processed without consideration of CA extravasation, the derived hemodynamic parameters are well known to be unreliable (7,8,96). Several techniques have been proposed and employed to correct for T_1 and T_2^* leakage effects (17,20,21,96-99). We propose that such DSC-MRI signals are influenced by the extravascular compartmentalization of CA and could potentially be used to extract information about the underlying spatial features of tumor cells within tissue (e.g. cell density, intercellular distance). The goal of this computational study is to investigate the dependence of extravascular T_2 and T_2^* leakage effects on physical features of extravascular space.

The motivation for exploring whether cellular properties influence DSC-MRI data originates from previous reports demonstrating that contrast agent extravasation and compartmentalization around cells can induce measurable and dynamic changes in gradient echo acquired signals (17-19,71). While spheres have been used extensively for evaluating susceptibility-based contrast mechanisms they poorly represent *in vivo* cellular distribution and shape. In particular, packed spheres intrinsically provide no means for modeling orientation heterogeneity and are unable to achieve cellular densities that approximate those found *in vivo.* To overcome these limitations we explore here the use of randomly packed ellipsoids (100). Modeling cells as ellipsoids enables the systematic investigation of several features relevant to DSC-MRI including ellipsoid orientation heterogeneity, volume, aspect ratio and higher packing fractions.

5.1 The Effects of Cellular Shape, Arrangement and Volume Fraction on ΔR_2^* and ΔR_2

To investigate the complex susceptibility effects that occur when contrast agent extravasates and compartmentalizes around cells, we used the FPFDM to compute the dependence of DSC-MRI derived ΔR_2^* and ΔR_2 leakage effects on structural features of the extravascular space. Three dimmenstonal cellular tissue models consisting of packed spheres or ellipsoids of fixed radii (9 μm) were used to study the effects of cellular shape and volume fraction. In addition to the effects of cellular shape and volume fraction, the influence of cellular packing arrangement is investigated by comparing results from randomly distributed spheres, closely-packed spheres on a face centered cubic (FCC) grid and randomly packed ellipsoids. To model contrast agent leakage effects relevant contrast agent levels corresponding to a $\Delta\chi$ value half the peak value of single dose Gd-DTPA injection is assumed. Figure 5.1a illustrates the FCC, random sphere and

ellipsoid packing models along with the respective representative 2D slices through the computed magnetic field perturbations. Figure 5.1b and 5.1c demonstrates the influence of cellular packing arrangements, shape and volume fraction on the computed ΔR_2^* and ΔR_2 values for $\Delta\chi = 5\times10^{-8}$, B_0 =1.5T, D = 10^{-5} cm^2/s, simulation time step Δt = 0.2 ms, GE TE = 40 ms and SE TE = 80 ms.

For a given packing arrangement, as cell volume fraction increases, the ΔR_2^* and ΔR_2 first increases and then decreases, reaching a peak value at a certain cell volume fraction which depends on cellular shape and arrangement. The highly ordered FCC packing of spheres resulted in the smallest relaxivity, reflecting the more homogeneous magnetic field perturbations and proton phase distributions. Randomly distributed spheres yielded slightly greater relaxivities with a non-linear relationship with packing fraction. Finally, the packed ellipsoids, which better approximate cell shape in vivo, enable higher random non-overlapping packing fractions (> 65%), are less ordered and also yielded a non-linear relationship between relaxivity and cell volume fraction. For all cell volume fractions, the ΔR_2^* and ΔR_2 values associated with the ellipsoid-based structures were greater in magnitude than those found with spheres.

To illustrate the observed dependence of ΔR_2^* and ΔR_2 on cell volume fraction, we computed the standard deviation of the magnetic field perturbation between the simulated grid points (ΔB_{std}) at each cell volume fraction. Figure 5.2 demonstrates that, the computed ΔR_2^* and ΔR_2 values are strongly related to ΔB_{std}.

5.2 The Effects of Cellular Spacing and Clustering on ΔR_2^* and ΔR_2

To further demonstrate the dependence of CA leakage induced T_2 and T_2^* effects on extravascular features, tissue structures composed of fixed vascular structure and variable ellipsoid packing are constructed. To study the effect of cellular spacing, which measures the mean separation between a given cell and neighboring cells, tissue structures reflecting variation in cellular separation ranging from 21-27 μm are constructed. To study the effect of cellular clustering, which estimates the size of an individual colony of cells that make up the extravascular space, tissue structures composed cellular cluster of varying sizes ranging from 5% to 30% are simulated. Both sets of tissue models are simulated using a fixed vascular volume fraction of 6%, cell volume fraction of 30% and cellular size of 9 μm. The resulting tissue structures along with the following simulation parameters (B_0 =1.5T, D = 10^{-5} cm^2/s, Δt = 0.2 ms, GE TE = 40 ms and SE TE = 80) were used in the FPFDM to compute ΔR_2^* and ΔR_2 values at different $\Delta\chi$ values.

Figure 5.3a and 5.3b illustrates sample tissue structures composed of fixed vascular tree and different cell separation of 21 μm and 27 μm, respectively. Figure 5.3c and 5.3d demonstrates the response of ΔR_2^* and ΔR_2 to changes in cell separation at three $\Delta\chi$ values of 3×10^{-8}, 4×10^{-8} and 5×10^{-8}. For a given $\Delta\chi$, the ΔR_2^* decreases as cell separation increases. This decrease in ΔR_2^* becomes larger at higher $\Delta\chi$ values, at $\Delta\chi=5\times10^{-8}$ the ΔR_2^* decreases by 60% as cell separation increase from 21 μm to 27 μm. Unlike ΔR_2^*, the computed ΔR_2 values show a slight increase as cell separation increases. While changes are very small at low $\Delta\chi$, for $\Delta\chi=5\times10^{-8}$ the ΔR_2 increases by 27% as cell separation increase from 21 μm to 27 μm.

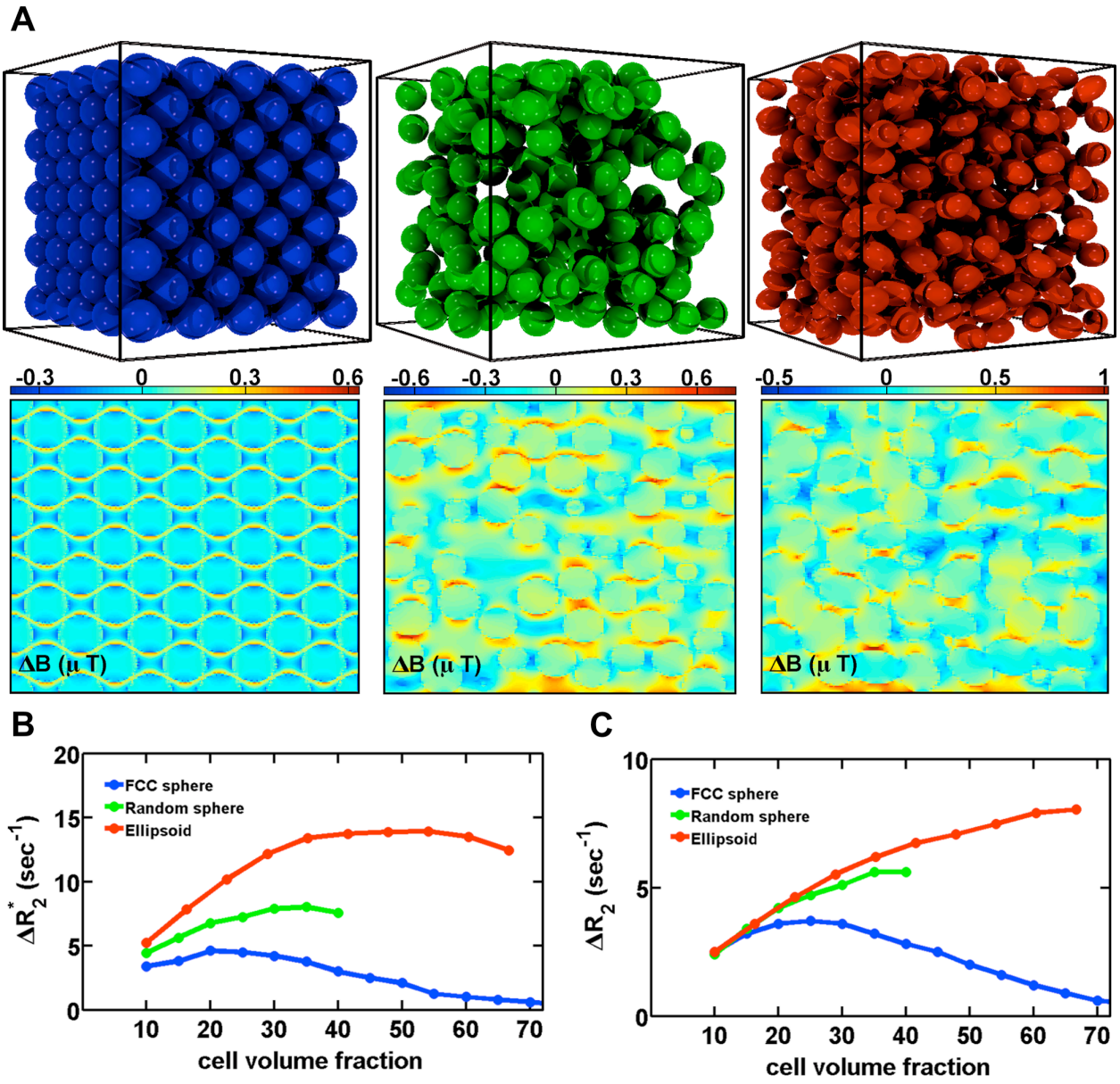

Figure 5.1: Dependence of ΔR_2^* and ΔR_2 on cellular shape, volume fraction and packing arrangement. (a) top raw shows example cellular models for FCC sphere packing (left), random sphere packing (middle) and random ellipsoid packing (right), bottom raw shows the respective 2D slice through the associated magnetic field perturbation for each structure calculated at B_0 =1.5T and $\Delta\chi = 5\times10^{-8}$. Compared to random sphere and ellipsoid packing, the field perturbation pattern for FCC packing is a homogenous periodic pattern suggesting that most spins experience similar field shifts as they diffuse, hence less phase dispersion. (b, c) The computed ΔR_2^* and ΔR_2 dependence on cell shape, volume fraction and packing arrangement. For all packing arrangements, the relaxivity increases and then decreases with cell volume fraction. Ellipsoid packing yields greater relaxivity than spheres. ΔR_2 exhibits qualitatively similar behavior to ΔR_2^* yet with a reduced magnitude.

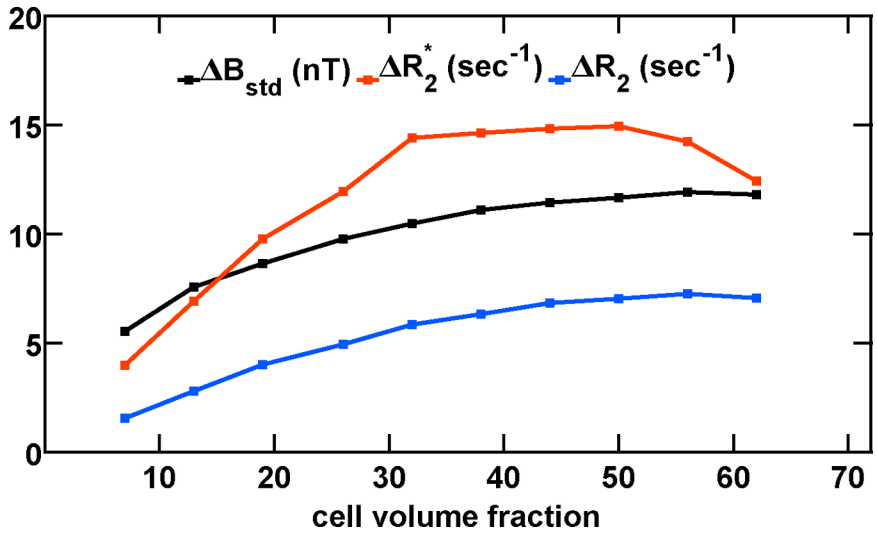

Figure 5.2: Dependence of ΔR_2^*, ΔR_2 and ΔB_{std} on cell volume fraction. The dependence of ΔR_2^*, ΔR_2 and ΔB_{std} on cell volume fraction exhibits a strong similarity suggesting both ΔR_2^*, ΔR_2 are mainly determined by ΔB_{std}. The ΔR_2^* starts to decrease before ΔB_{std} reaches the maximum indicating stronger diffusion averaging at high cell volume fraction compared to less dense tissues.

Figure 5.4 illustrates the effect of cluster size variation on the computed ΔR_2 and ΔR_2^* values. Example 3D tissue structures representing 5% and 15% cluster volume fraction are shown in Fig. 5.4a and 5.4b respectively. Simulation results show that ΔR_2^* increases with increasing cluster volume, Fig. 5.4c. The variation in ΔR_2^* becomes larger at higher $\Delta\chi$ values, for $\Delta\chi=5\times10^{-8}$ the ΔR_2^* increases by 40% as cluster size increase from 5% to 30%. The computed ΔR_2 values show negligible decrease as cluster volume increases, Fig. 5.4d.

In general, given other parameters are kept constant, cells that are closer together, such as may occur when cells are regionally localized within a voxel, yield greater ΔR_2^* as compared to those that are more homogenously distributed throughout a voxel. While variation is very small the overall compactness of cells has an opposite effect on the computed ΔR_2 values.

5.3 The Effects Ellipsoid Aspect Ratio on ΔR_2^* and ΔR_2

To further illustrate the influence of cellular geometry on DSC-MRI derived T_2 and T_2^* leakage effects we computed the dependence of ΔR_2^* and ΔR_2 on ellipsoid shapes. In addition to the enhanced relaxation rates, the use of ellipsoids allows one to investigate a wide range of cell geometries. In order to alter the shape of the ellipsoid we varied the ellipsoid aspect ratio, which is the ratio of the smallest to the largest ellipsoid axis, from 0.25 (flat) to 1 (spherical). Using model tissue structures reflecting variations in ellipsoid aspect ratio we computed the ΔR_2^* and ΔR_2 values for three $\Delta\chi$ and two B_0 values, using simulation parametrs of D = 10^{-5} cm^2/s, Δt = 0.2 ms, GE TE = 40 ms and SE TE = 80. The cell volume fraction, vascular volume fraction and cell size constant at 30%, 6% and 9 μm, respectively, were kept constant.

Example tissue structures using ellipsoid aspect ratio of 0.7 and 0.25 are shown in Fig. 5.5a and 5.5b, respectively. For a given $\Delta\chi$ and B_0 values the computed ΔR_2^* values first increase with increasing aspect ratio and reaches a peak value near 0.6 before decreasing as ellipsoids become more spherical. For $\Delta\chi=5\times10^{-8}$ and B_0=1.5T, ΔR_2^* increases by 30% as the aspect ratio changes from 0.25 to 0.6 (Fig. 5.5c). In general the difference between the computed ΔR_2^* values induced by changes in aspect ratio become larger for higher field strengths (B_0=3T) and large $\Delta\chi$ values, (Fig. 5.5d). Though the dependence of the computed ΔR_2 values is similar to ΔR_2^* the variation is very small (Fig. 5.5e and 5.5f).

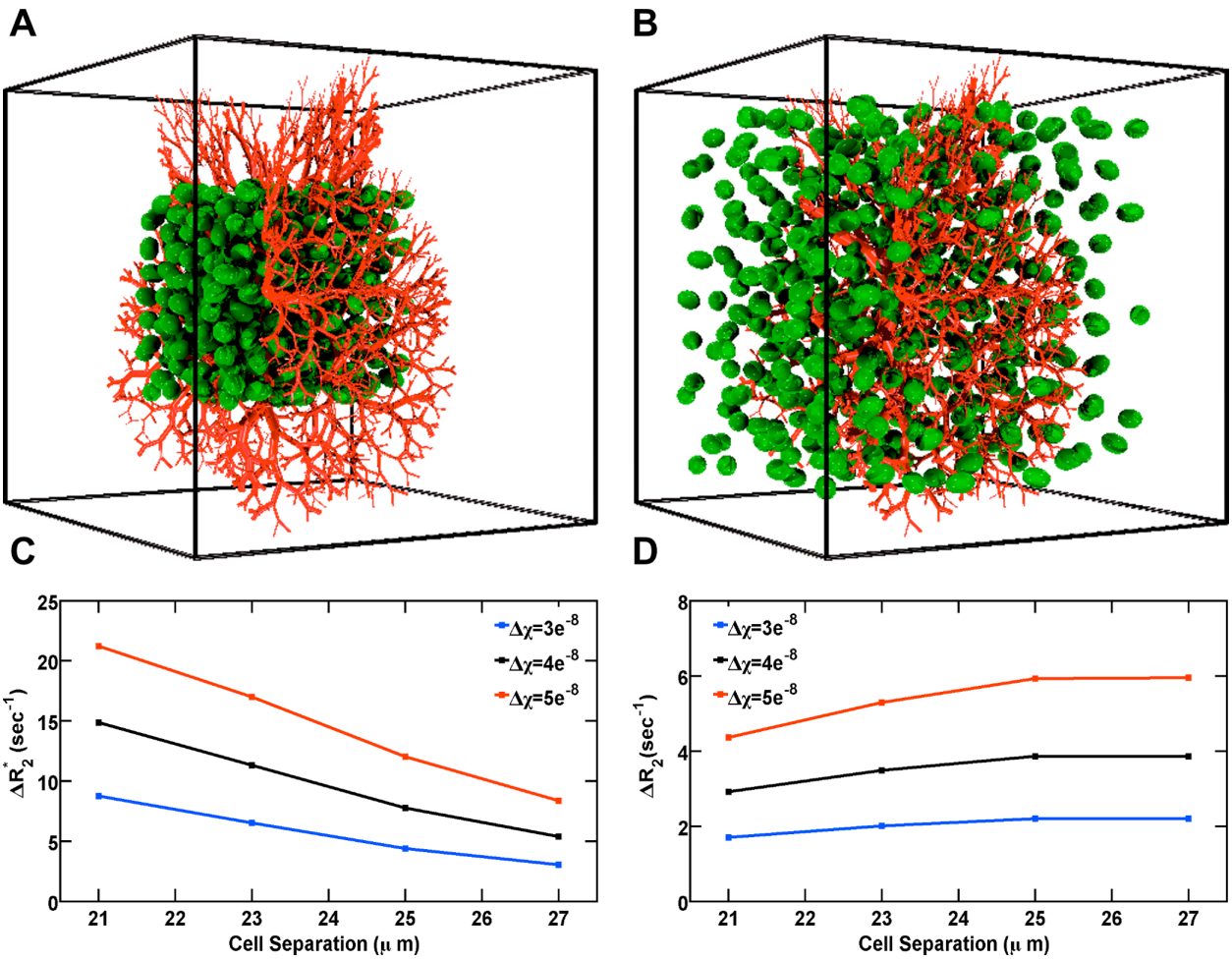

Figure 5.3: Dependence of ΔR_2^* and ΔR_2 on cell separation. Example tissue structures composed of 6% vascular tree and 30% cell volume fraction for mean cellular separation of 21 μm (a) and 27 μm (b). The dependence of the computed ΔR_2^* (c), and ΔR_2 (d), values on cell separation calculated at B_0 =1.5T and three $\Delta\chi$ levels. While the decrease in ΔR_2^* observed as cell separation increases is associated with a decrease in field perturbation variation, the less pronounced increase in ΔR_2 values is due to an increase in the non reversible diffusion related loss of phase coherence.

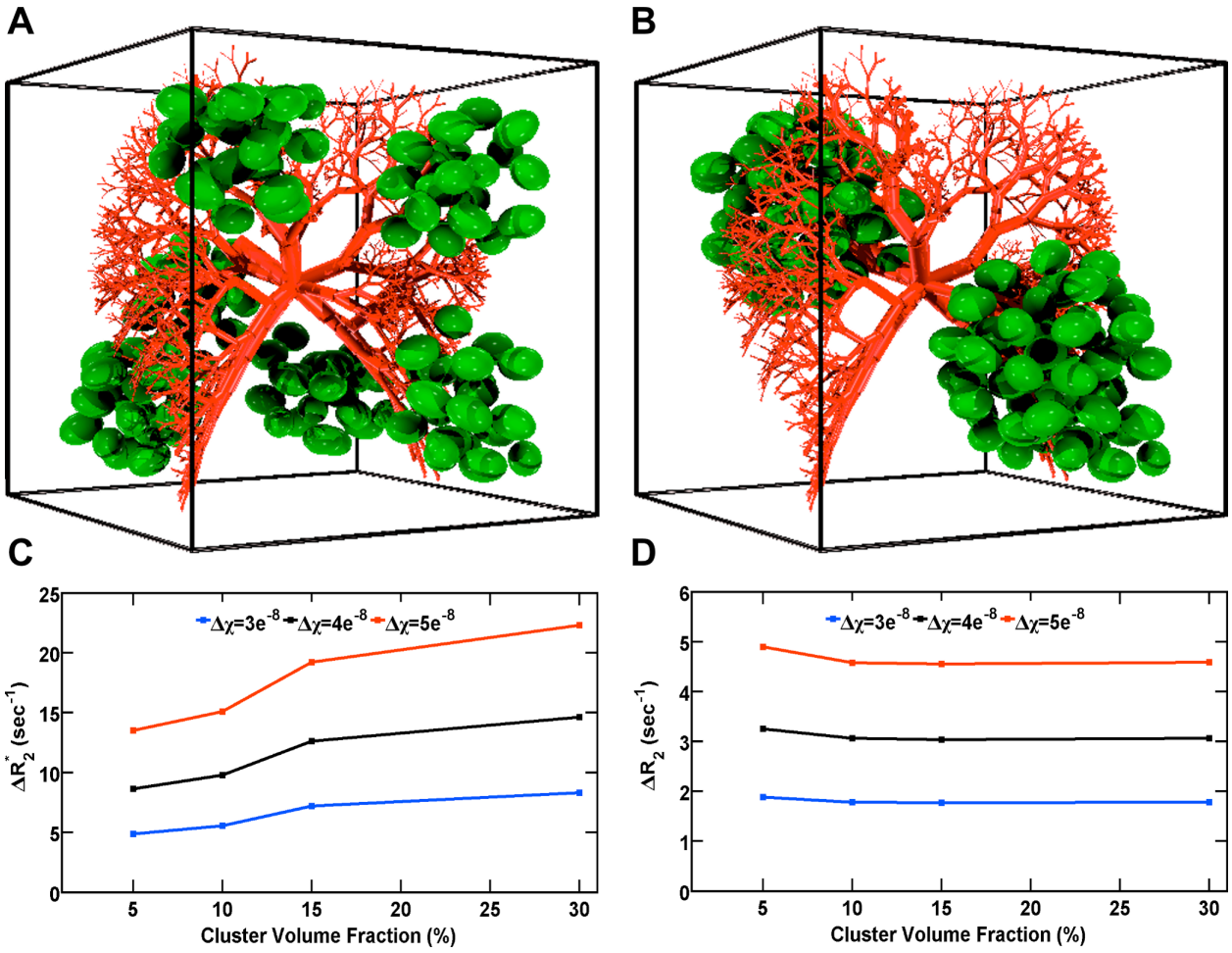

Figure 5.4: Dependence of ΔR_2^* and ΔR_2 on cell clustering. Example tissue structures composed of 6% vascular tree and 30% cell volume fraction with ellipsoids cellular clusters of 5% (a) and 15% (b). The dependence of the computed ΔR_2^* (c), and ΔR_2 (d), values on cellular cluster size calculated at B_0 =1.5T and three $\Delta\chi$ levels. While the computed ΔR_2^* exhibit a measurable increase with increasing cluster volume, the changes in ΔR_2 values are very small.

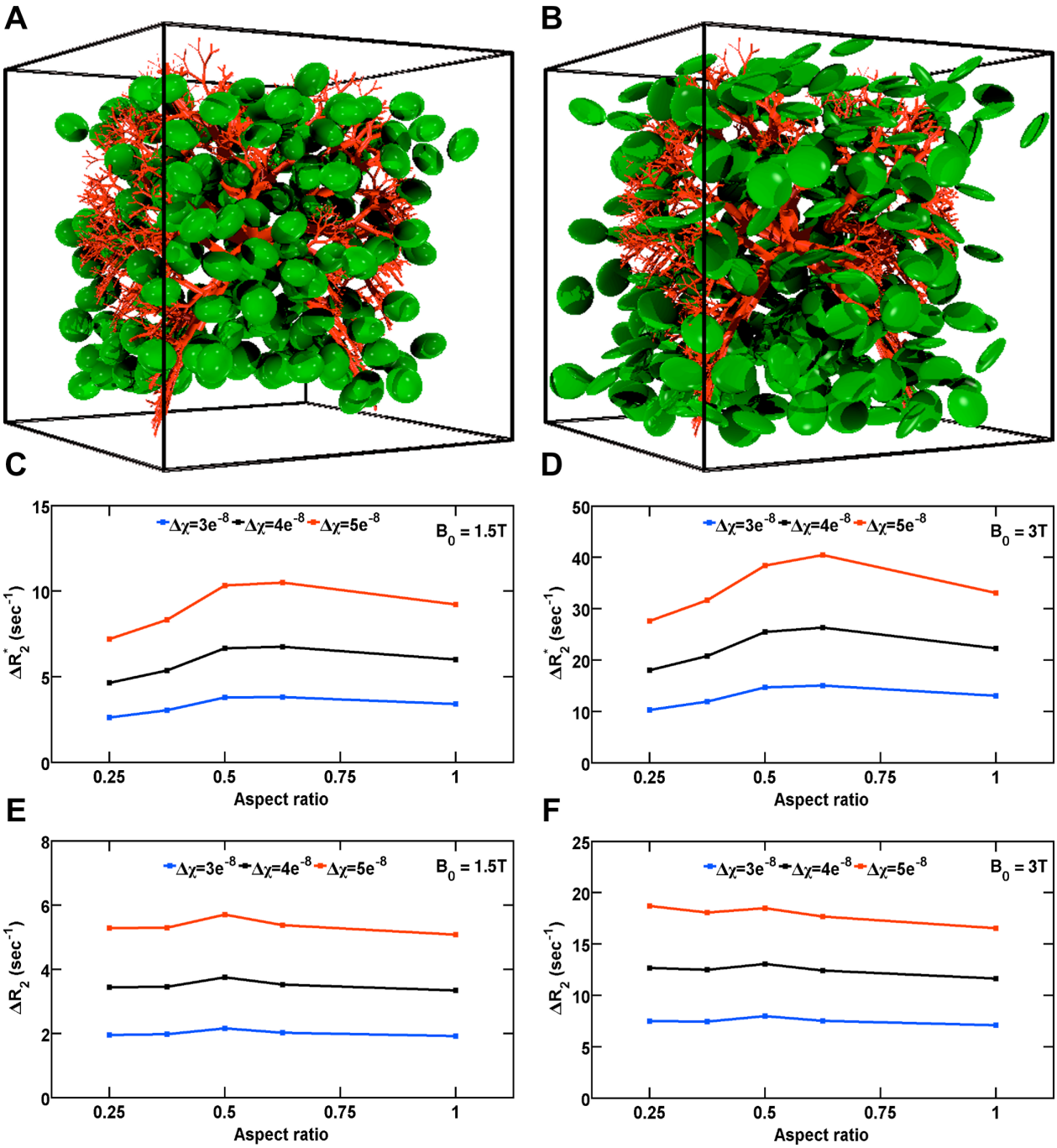

Figure 5.5: Dependence of ΔR_2^* and ΔR_2 on ellipsoid aspect ratio. Example tissue structures composed of 6% vascular tree and ellipsoid cells of 30% volume fraction with ellipsoid aspect ratio of 0.7 (a) and 0.25 (b). The dependence of ΔR_2^* on ellipsoid shapes calculated for three $\Delta\chi$ levels at B_0 =1.5T (c) and B_0 =3T (d), shows that ellipsoids with an intermediate aspect ratio (0.7) create a larger variation in field perturbations as compared to those that are very flat (0.25). (e, f) The corresponding computed values of ΔR_2 exhibit a similar but very small dependence on ellipsoid aspect ratio. These effects are greater at higher field strengths.

5.4 The Effects of Diffusion and Cell Size on ΔR_2^* and ΔR_2

To investigate the effect of water diffusion on the observed ΔR_2^* and ΔR_2 characteristic dependence to changes in cell volume fraction, we first computed the dependence of ΔR_2^* and ΔR_2 on cell volume fraction at a fixed cell size (9 μm) for variable water diffusion coefficients ranging from $D=0.5\times10^{-5}$ cm^2/s to $D=2.5\times10^{-5}$ cm^2/s. This diffusion coefficient values were chosen to encompass the range of MR imaging derived apparent diffusion coefficients of human brain tumors (101). To investigate the dependence of ΔR_2^* and ΔR_2 on cellular size at different cell volume fraction levels (10%-60%), we computed ΔR_2^* and ΔR_2 for 18 perturber sizes ranging from 1-100 μm at a fixed $D=10^{-5}$ cm^2/s.

Figure 5.6a shows the cell volume fraction dependence of ΔR_2^* computed at different D values. For all cell volume fractions considered, the ΔR_2^* decreases as D increases, as a consequence of the increased effect of motional narrowing. These results also show that the difference between ΔR_2^* values computed at the slowest diffusion ($D = 0.5\times10^{-5}$ cm^2/s) and fastest diffusion ($D = 2.5\times10^{-5}$ cm^2/s) increase from 30% to 50% as cell density increases from 7% to 62%. This observation demonstrates that the motional averaging effect becomes more significant at higher cell densities. Figure 5.6b shows that the computed ΔR_2 dependence on D relies on cell volume fraction. For instance, a closer look at the ΔR_2 values at lower cell density shows the ΔR_2 values first increase, reaching a peak at $D = 2\times10^{-5}$ cm^2/s, before decreasing. On the other hand, at higher cell density the computed ΔR_2 values peaks at a relatively lower diffusion cofficent, $D = 1\times10^{-5}$ cm^2/s.

Figure 5.7a and 5.7b shows the expected perturber size dependence of ΔR_2^* and ΔR_2 over a range of cell volume fractions. These results show that the perturber size corresponding to, the point where the diffusion independent regime for gradient echo begins and the spin echo relaxivity peaks, shifts to the right (larger sizes) as cell volume fraction increases. This indicates that at relatively higher cell density (50%-60%), relevant to cellular volume fraction levels observed in vivo (102), the ΔR_2^* becomes more sensitive cell size. For instance, for v_i=20% a change in cell size from 5 μm to 20 μm results ΔR_2^* to increases by 25% whereas the same cellular size change yields a 45% change in ΔR_2^* for v_i=60%.

Both set of computational results (Fig. 5.6 and Fig. 5.7) were carried out using $\Delta\chi = 5\times10^{-8}$, B_0 =1.5T, Δt = 0.2 ms, GE TE = 40 ms and SE TE = 80 ms, and taken together demonstrate the influence of motional averaging on the cell density dependence of ΔR_2^* and ΔR_2.

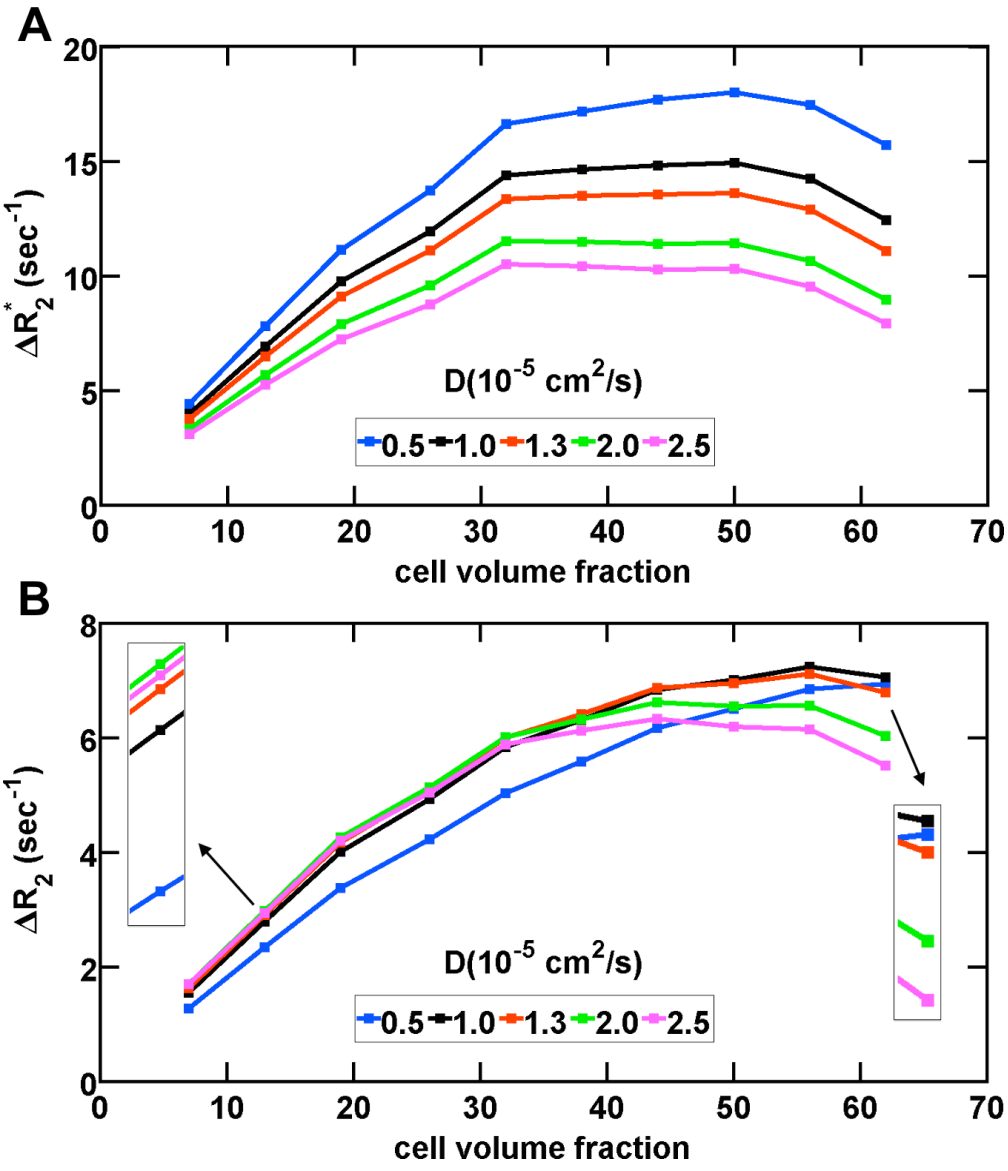

Figure 5.6: Dependence of ΔR_2^* and ΔR_2 on diffusion. The dependence of ΔR_2^* (a), and ΔR_2 (b) on cell volume fraction computed at water diffusion values ranging from slow ($D=0.5\times10^{-5}$ cm^2/s) to fast ($D=2.5\times10^{-5}$ cm^2/s). For a given cell volume fraction, the ΔR_2^* decreases as D increases owing to increased motional averaging, but the diffusion induced percentage decrease in ΔR_2^* depends on cell density. As expected, an increase in D could increase or decrease ΔR_2, but the diffusion value corresponding to the peak ΔR_2 relies on cell density. Results were obtained using, cell size=9 μm, $\Delta\chi = 5\times10^{-8}$, B_0 =1.5T, Δt = 0.2 ms, GE TE = 40 ms and SE TE = 80 ms.

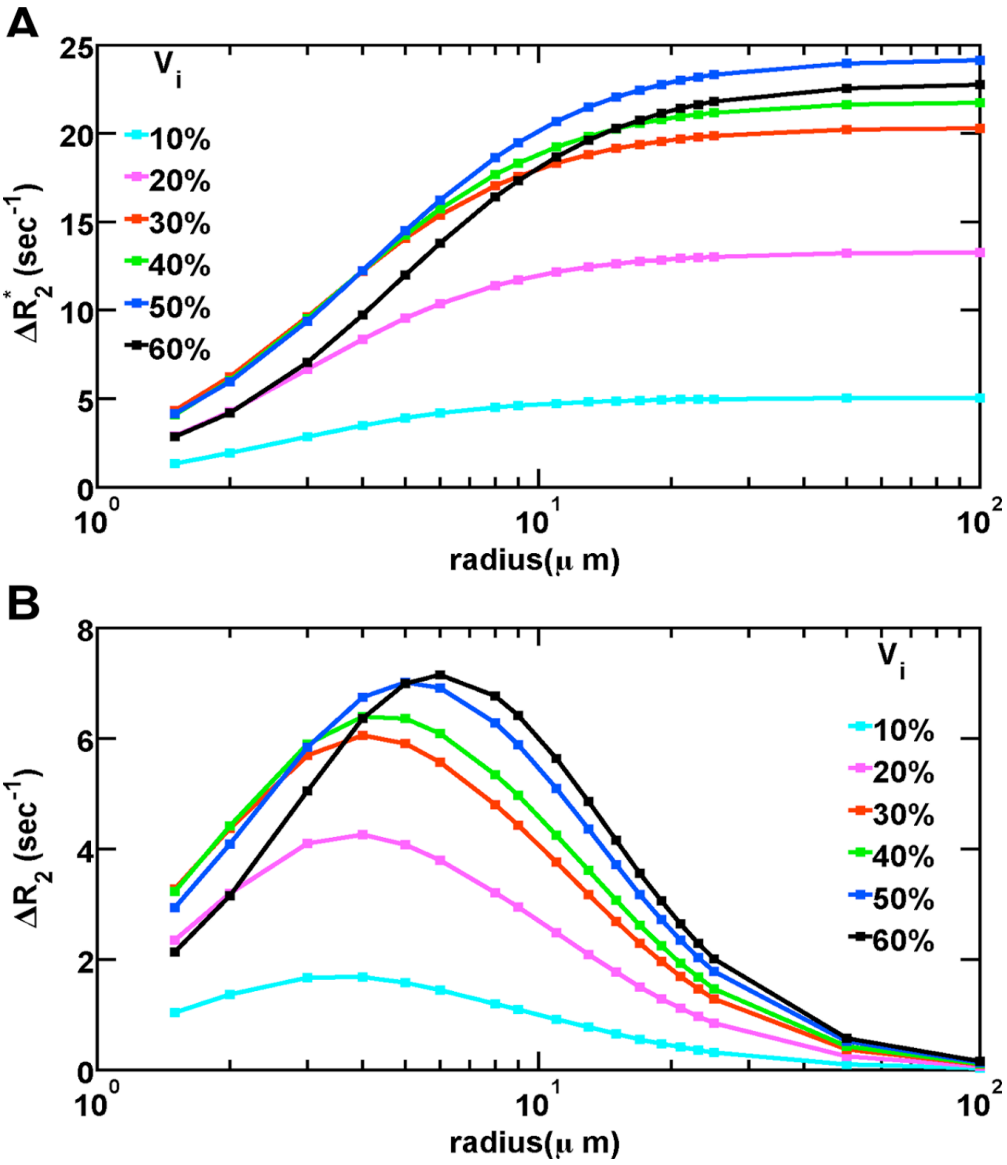

Figure 5.7: Dependence of ΔR_2^* and ΔR_2 on cell size. The cell size dependence of ΔR_2^* (a), and ΔR_2 (b) computed at different cell density levels ranging from v_i=10% to v_i=60%. For all cell volume fractions, the characteristic perturber size dependence of ΔR_2^* and ΔR_2 is attained, but as cell density increases the perturber size where ΔR_2 peaks and ΔR_2^* reaches a plateau shifts to larger sizes. These results were computed using, $D=10^{-5}$ cm^2/s, $\Delta\chi = 5\times10^{-8}$, B_0 =1.5T, Δt = 0.2 ms, GE TE = 40 ms and SE TE = 80 ms.

5.5 Discussion and Conclusion

Previous reports have shown that T_2^* leakage effects influence DSC-MRI data and have suggested a link between their presence and tissue cellularity (17,18,66,71,103,104), but, to date, their biophysical basis is poorly characterized. In this study, we validate using realistic and systematic simulations, that features of extravascular space influence T_2 and T_2^* leakage effects.

The FPFDM has the potential for modeling nonstandard geometries that may better mimic cells and microvasculature *in vivo*. We computed relaxivities for simulated 3D cellular models consisting of packed spheres and ellipsoids (Fig. 5.1), and found greater relaxivity for packed ellipsoids over all volume fractions compared to the sphere packing (Fig. 5.1b and 5.1c). This suggests that the additional degree of freedom in spatial orientation for ellipsoids increases field perturbation heterogeneity. A critical step towards elucidating the origins of T_2 and T_2^* leakage effects in this study was the use of realistic tissue models and the FPFDM for DSC-MRI signal estimation. The use of structures like ellipsoids to mimic cells enables a closer approximation of cellular orientation, packing density and spatial heterogeneity. These features are essential for approximating the magnitude of T_2^* leakage effects observed clinically. In contrast, the use of packed spheres as cells leads to more homogenous field perturbations and, consequently, greatly underestimate T_2 and T_2^* leakage effects.

Simulation results also demonstrate that in addition to cell shape and packing arrangement, cell volume fraction influence the computed ΔR_2 and ΔR_2^* values. The observed dependence of ΔR_2^* and ΔR_2 on cell volume fraction (Fig. 5.1b and 5.1c) can be understood by examining the cell volume fraction induced changes to the computed local magnetic field perturbation (ΔB) and the standard deviation of the magnetic field perturbation between the simulated grid points within the voxel (ΔB_{std}). At low cell volume fractions (e.g. 20%) the addition of cells into the structure will increase both the ΔB in the vicinity of the new cell and the ΔB_{std}. At higher cell volume fractions (~45-55%), adding new cells increases ΔB in their vicinity and the ΔB_{std} will reach a peak. Beyond this peak, adding more cells will continue to add perturbation, however, as the structure becomes more populated, a higher fraction of the protons will experience similar ΔB values, causing the ΔB_{std} to decrease. The observed ΔR_2^* dependence on cell volume fraction is consistent with the notion that the standard deviation of the field perturbation determines the ΔR_2^* rather than the net magnetic field perturbation of the voxel (103). This is further supported by the result shown in Fig. 5.2. The similarity between the ΔB_{std} and ΔR_2 shows that the irreversible relaxation measured by the SE sequence comparably depends on the competing effects of field variations and diffusion relaxation mechanisms, which is expected for a system in the intermediate relaxation regime, consistent with the values we used for cell size, D, B_0 and $\Delta\chi$ (47). The result also shows that ΔR_2^* reaches its peak value at slightly lower volume fraction (~50%) than ΔB_{std}, suggesting an increase in motional averaging as cell density increases.

Computational results presented in Figs. 5.3 and 5.4 reveal DSC-MRI derived T_2 and T_2^* leakage effects depend on cellular separation and cluster size. The observed dependence of ΔR_2^* on cell separation and cluster volume is directly associated with the variation of the field perturbation between the simulation grids within the simulated voxel (ΔB_{std}). In general, for a given cell volume fraction and cell size, cells that are closely packed (small cellular separation) or cells that form a large colony (large cluster volume) create large ΔB_{std}, thus yield greater ΔR_2^*. On the contrary, though the changes are very small the computed ΔR_2 values are inversely

related with cellular compactness. This can be explained by examining the competing effects of relaxtion due to local field variations and diffusion mediated susceptibility phase dispersion. For the tissue models used in this investigation, although ΔB_{std} is higher for compactly packed cells (small cell separation or large volume cluster) than cell arrangements that are more disperse across the voxel (large cell separation or small volume cluster), the 180^o refocusing pulse is more effective to recover the diffusion mediated loss of phase coherence for compactly packed cells than the loosely packed cells. This is mainly due to the nature of the tissue model employed here. For practical reasons, as seen from water molecules diffusing in the periphery of a large colony of cells, the colony appears as a large perturber resulting a pseudo system in the static dephasing regime, yielding small ΔR_2 owing to an effective recovery of the static dephasing by the formation of an echo.

Further dependence of T_2 and T_2^* leakage effects on cellular features is demonstrated using ellipsoid shape variation, as determined by the aspect ratio. For a given cell volume fraction and size, the computed ΔR_2^* values were found to depend on ellipsoid shape, Fig. 5.5. The observed dependence of ΔR_2^* on aspect ratio could be understood via close examination of the ellipsoid shape and the associated field perturbation. For very flat ellipsoids (small aspect ratio) the spatial distortion of the dipole field nature of the field perturbation is large, resulting in the majority of spins near the ellipsoid to experience either the positive or the negative field perturbation leading to a narrow phase dispersion, thus small ΔR_2^*. For ellipsoids with aspect ratio close to 1 (spheres and close to spherical shapes), the distortion of the dipole field perturbation is very small, resulting in nearby spins experiencing both the positive and the negative field perturbations leading to a wider phase dispersion. However, due to the symmetry of the dipole field perturbations, tissue structures composed of such shapes experience significant cancelation of field perturbation when the negative and the positive poles from neighboring perturbers overlap, leading to intermediate ΔR_2^* values. The extreme effect of this overlapping between the positive and the negative dipole field perturbation explains the very small ΔR_2^* values for FCC spherical packing. For ellipsoids with intermediate aspect ratios, though the intermediate distortion of the dipole field perturbation leads to smaller phase dispersion among nearby spins than would be observed for spheres, the lack of cancelation due to overlapping of opposite poles yield larger ΔR_2^* values. These effects become more apparent at stronger fields as shown in Fig. 5.5. While the shape dependence is smaller, the ΔR_2 follows a similar trend.

The results shown in Figs. 5.6 and 5.7 are consistent with previous reports of the characteristic pertuber size dependency of relaxation rates. Furthermore, these computational results demonstrate the influence of cell density on the strength of the diffusion narrowing process. For high cell density, at fixed values of B_0, $\Delta\chi$ and cell size, the process of motional averaging influences ΔR_2^* at relatively lower diffusion values. Similarly, at fixed values of B_0, $\Delta\chi$ and D, motional averaging stays significant at relatively larger cell sizes. Consequently, for high cell densities, the perturber size where ΔR_2 peaks and ΔR_2^* reaches a plateau occurs at relatively larger cell sizes as compared to lower cell density. This suggests that for physiologically relevant tumor cell volume fractions levels (50-60%) observed in vivo (102), DSC-MRI derived ΔR_2^* values are highly sensitivity to variations in tumor cell size (105).

In summary, the computational results presented herein support the hypothesis that DSC-MRI data acquired in the presence of contrast agent leakage are highly sensitive to variations in cell density, distribution, geometry and size, suggesting DSC-MRI derived CA leakage effects could potentially be used to extract information about the underlying spatial distribution of tumor cells within tissue. The upcoming chapter exploits a multi-echo DSC-MRI approach to discern T_1

and T_2^* leakage effects in order to extract a clinically feasible imaging biomarker that could be used to characterize the tumor cellular characteristics.

CHAPTER 6

ASSESSING TUMOR CELLULARITY USING MULTI-ECHO DSC-MRI DERIVED MEASURES OF THE TRANSVERSE RELAXIVITY AT TRACER EQUILIBRIUM (TRATE)

6.1 Introduction

DSC-MRI derived perfusion parameters have proven useful for assessing tumor grade and treatment response. But DSC-MRI signals are ambiguous due to changes in T_1 and T_2^*-relaxivity during tracer extravasation, often resulting in unreliable estimates of perfusion parameters (7,8,96). In addition to improving the reliability of DSC-MRI data acquired in the presence of CA leakage, there is an increased interest in leveraging the temporal characteristics of such signals to estimate additional biological information. Pharmacokinetic modeling of DSC-MRI signals in brain tumors has been used to extract CA extravasation rate constants (e.g. K^{trans}) and the extravascular extracellular volume fraction (v_e) (20,99,106-109). The appearance of leakage effects on DSC-MRI signals, whether they are predominantly T_1 or T_2^*-based, has been characterized by the Percent Signal Recovery (PSR), a parameter potentially capable of differentiating between gliomas, metastasis and lymphomas (71). Recent studies have shown that CA leakage-induced T_2^* effects are dependent upon the extravascular geometry (17-19,66,104) and by quantifying these effects, new imaging biomarkers may be derived (19). Once validated, such parameters could improve the characterization of brain tumors.

Currently, multi-echo DSC-MRI, along with a pre-contrast T_1 map, is used to characterize T_1 and T_2^* leakage effects, as this enables their simultaneous separation and quantification (18,19,99,107). The dynamic T_1 change enables estimation of the tissue CA concentration. Combining the CA concentration with the dynamic T_2^* changes enables the assessment of the tissue CA transverse (T_2^*) relaxivity. Recently, Sourbron et al used this approach in colorectal cancer xenografts to evaluate the vascular and extravascular CA relaxivity, and found that it provided supplementary information on tumor microstructure that is distinct from traditional compartmental volume fraction measurements (19).

In this study, we aimed to evaluate whether multi-echo DSC-MRI derived measures of the Transverse Relaxivity at Tracer Equilibrium (*TRATE*) may be used to evaluate brain tumor cytoarchitecture. To validate the sensitivity of *TRATE* to tumor cellular features we employ realistic biophysical simulations and compare its characteristics in two animal brain tumor models that are known to have histologically different cellular properties. We also present initial results of *TRATE* data in a glioma patient. The *TRATE* maps are spatially compared to parameters traditionally derived from DSC-MRI, Dynamic Contrast Enhanced (DCE)-MRI and Diffusion Weighted Imaging (DWI) in order to preliminarily assess its potential to provide unique sensitivity to microstructural features not assessed with these techniques.

6.2 Method

6.2.1 TRATE: Theory

When CA extravasation effects are present, the tissue transverse relaxation rate depends on both dipole-dipole microscopic interactions between the CA and water protons and mesoscopic effects due to magnetic field perturbation induced by CA compartmentalization within vascular walls and around cells. Models have been previously proposed (17-20), that incorporate both microscopic and mesoscopic contributions to the measured transverse relaxtion rate change (ΔR_2^*):

$$\Delta R_2^* = r_2\left(v_e C_e + v_p C_p\right) + r_{2p}^* v_p\left(v_e\left|C_p - C_e\right| + v_i C_p\right) + r_{2e}^* v_e v_i C_e \tag{6.1}$$

Here v_e, v_i and v_p denote volume fractions of the extravascular extracellular space (EES), extravascular intracellular space (EIS) and vascular space, respectively. C_e and C_p represent the CA concentration of the EES and the vascular space, r_{2p}^* and r_{2e}^* are the effective T_2^* relaxivities of CA compartmentalized within the vascular space and EES, and r_2 is the CA T_2 relaxivity.

This model expresses the tissue CA concentration (C_t) as the sum of individual compartment CA concentrations weighted by the corresponding volume fractions ($C_t = v_e C_e + v_p C_p$), and assumes that the CA does not penetrate into cells and a fast water exchange process. At time points well past the first pass of CA, when C_e and C_p are approximately equivalent, Eq. 6.1 can be written as:

$$\Delta R_2^* = \left\{ r_2 + \frac{v_i}{v_p + v_e}\left(v_p r_{2p}^* + v_e r_{2e}^*\right)\right\} C_t \tag{6.2}$$

The first bracketed term in Eq. 6.2 can be considered as the effective tissue transverse relaxivity at CA equilibrium and will be termed the transverse relaxivity at tracer equilibrium (*TRATE*) hereafter. With this definition, Eq. 6.2 simplifies to:

$$\Delta R_2^* = TRATE \times C_t \tag{6.3}$$

With multi-echo DSC-MRI data and a pre-contrast T_1 map the tissue CA concentration and the ΔR_2^* can be computed using the extracted T_1 and T_2^* changes, respectively, thereby enabling the computation of *TRATE*.

6.2.2 TRATE: Simulation

To investigate the dependence of *TRATE* on tissue vascular and cellular features, simulated realistic 3D tissue structures were created using randomly packed ellipsoids around fractal tree

based vascular networks, magnetic field perturbations and ΔR_2^* were computed using the FPFDM as previously described in chapters 3-5.

For CA concentration levels corresponding to tracer equilibrium, the slope of the computed ΔR_2^* versus C_t was used to estimate *TRATE*. To investigate the relative contribution of the vascular and extravascular features to *TRATE* measurements, the signal relaxation was computed using tissue models with fixed cellular features and variable vascular volume fractions. Furthermore, to evaluate the dependence of ΔR_2^* and *TRATE* on cellular features, such as cell volume fraction and cell size, the vascular volume fraction was kept fixed while these features were systematically varied.

Unless mentioned otherwise, all simulation studies were carried out using the following input parameters. All input tissue structures consisted of a $(0.5\ mm)^3$ 3D volume sampled with 128^3 simulation grids. The restricted water diffusion coefficient (D) was set to $1.3\times10^{-3}\ mm^2/s$ (110) and clinically relevant TE and B_0 values of 40 ms and 3T were chosen. The susceptibility difference between compartments was calculated using $\Delta\chi = \chi_m.\ [CA]$, where [CA] is compartmental CA concentration and χ_m is the CA molar susceptibility ($0.027\times10^{-6}\ mM^{-1}$) (62). While the susceptibility-induced relaxation was computed using the FPFDM, the relatively small effects of microscopic transverse relaxation were calculated and included using the product of C_t and the Gd-DTPA T_2 relaxivity ($r_2 = 4.5\ mM^{-1}\ s^{-1}$ (111)).

6.2.3 TRATE: Animal studies

Measures of *TRATE* were compared in two rodent brain tumor models, C6 glioblastoma (n = 7) and 9L gliosarcoma (n = 7). Male Wistar and Fischer rats (Harlan, Indianapolis, IN, USA) were inoculated with either 1×10^5 C6 or 9L cells (American Type Culture Collection, Manassas, VA, USA). Prior to all surgical and imaging procedures, animals were immobilized in a stereotactic head holder. Anesthesia was induced via a 5%/95% isoflurane/oxygen mixture and maintained via a 2%/95% isoflurane/oxygen mixture.

All experiments were carried out 14–16 days after tumor inoculation and adhered to our institution's animal care and use committee policies. Scans were conducted at 4.7T (Agilent) with a Doty shielded Litz coil (38 mm ID). A pre-contrast T_1 (T_{10}) map was obtained using a gradient-echo based multiple flip angle approach with the following parameters: TR = 200 ms, TE = 2 ms, FOV = $(40\ mm)^2$, slice thickness (ST) = 2.0 mm, matrix = 64^2, five flip angles (FA) (ranging from 12° to 60°), and 4 excitations. A multi-echo fast low angle shot sequence was used to acquire DSC-MRI data with a temporal resolution of one image per second for a total duration of 17 minutes with: TR=15.625 ms, TE1/TE2=4/8 ms, FOV=$(40\ mm)^2$, ST=2.0 mm, FA=9°, and matrix=64^2. After the acquisition of 60 baseline images, a bolus of Gd-DTPA (0.2 mmol kg^{-1} per body weight) was intravenously delivered using a power injector at an infusion rate of 2.4 ml/min. As described above, the multi-echo DSC-MRI sequence was used to quantify T_1 and T_2^* time series. The pre-contrast T_1 maps were combined with the T_1-weighted time series to derive ΔR_1 (112). The last two minutes of the ΔR_1 and ΔR_2^* time series data were then used to compute *TRATE* using:

$$C_t = \Delta R_1 / r_1, \qquad and \qquad TRATE = \Delta R_2^* / C_t \tag{6.4}$$

where r_1 is the Gd-DTPA T_1 relaxivity (3.9 $mM^{-1} s^{-1}$) (111).

The reference region pharmacokinetic model was applied to the ΔR_1 time series in order to compute the DCE-MRI parameters, v_e and K^{trans} (107,113). Furthermore, DWI was performed to estimate *ADC* maps using a fast spin echo sequence (TR=200 ms, TE=30 ms, FOV=$(40\ mm)^2$, ST=1.0 mm, matrix=64^2, four b-values between 0 to 1000 s/mm^2, and 4 excitations). To evaluate tumor cellularity, all animals were sacrificed after the MRI exams, the tumor tissue dissected and fixed in 10% formalin, cut into 5-μm sections and stained with hematoxylin and eosin (H&E). The H&E slides were digitally scanned and analyzed to quantify cell density using an Ariol SL-50 automated scanning microscope. Statistical analysis to evaluate differences in H&E-based cell density, *ADC* and *TRATE* between the 9L and C6 tumors was performed using Student's t-test. Pearson's Correlation Coefficients were computed to assess spatial correlations between the imaging parameters.

6.2.4 TRATE: Clinical study

A patient (64 yo M) with a recurrent high-grade glioma was scanned at 3T (Philips Healthcare, Cleveland, OH) using a 32 channel head coil. Multiple FA data was acquired (TR=7.6 ms, TE=3.7 ms, FA=2°-20° in 2° increments, FOV=240x240 mm^2, ST=5 mm, matrix=96^2) to produce a T_{10} map. Next, a multi-echo single-shot EPI acquisition (TR=1.5 s, TE1/TE2=7/31 ms, FOV=240x240 mm^2, ST=5 mm, matrix =96^2) was performed before, during, and after administration of 0.1 mmol/kg Gd-DTPA at an infusion rate of 4 ml/s (followed by a saline flush). The scan duration was 7.5 minutes and followed all guidelines set by the Vanderbilt University Institutional Review Board. Measures of ΔR_2^* and ΔR_1 were calculated from the multi-echo data for the entire time-course (112). DSC-MRI perfusion maps were calculated from the ΔR_2^* measurements and an automated measure of the AIF, using circular SVD-based deconvolution (114). Maps of K^{trans}, v_e and *ADC* (DW SE-ssEPI, TR=6s, TE=44ms, NEX=2, b=100,1000 s/mm^2) were also computed. Voxel wise estimates of C_t and *TRATE* were calculated according to Eq. 6.4.

6.3 Results

Figure 6.1 shows example FPFDM simulation results, demonstrating the main input and output parameters. Fig. 6.1a shows a 3D volume rendering of a sample tissue structure, which contains a 60% volume fraction of ellipsoids (average radius 15 μm) and a 6% vascular volume fraction with vessel sizes ranging from 5 μm to 45 μm. For illustrative purposes, the two compartment pharmacokinetic model described by Brix *et al* was used to create the C_e and C_p time curves (with clinically relevant input parameters) shown in Fig. 6.1b (61). Figure 6.1c shows a representative 2D slice through the tissue structure along with magnetic field perturbations computed at three time points indicated in Fig. 6.1b. For time points near the peak of C_p, where C_e is very small, the field perturbation is dominated by the vascular structure, as indicated by the strong field perturbations surrounding the vessels. As C_e increases, the field perturbation around cells starts to emerge and dominates the vascular field perturbation at time points near CA

equilibrium, as illustrated by the elevated field perturbations surrounding ellipsoids. The resulting ΔR_2^* time curve is shown in Fig. 6.1d.

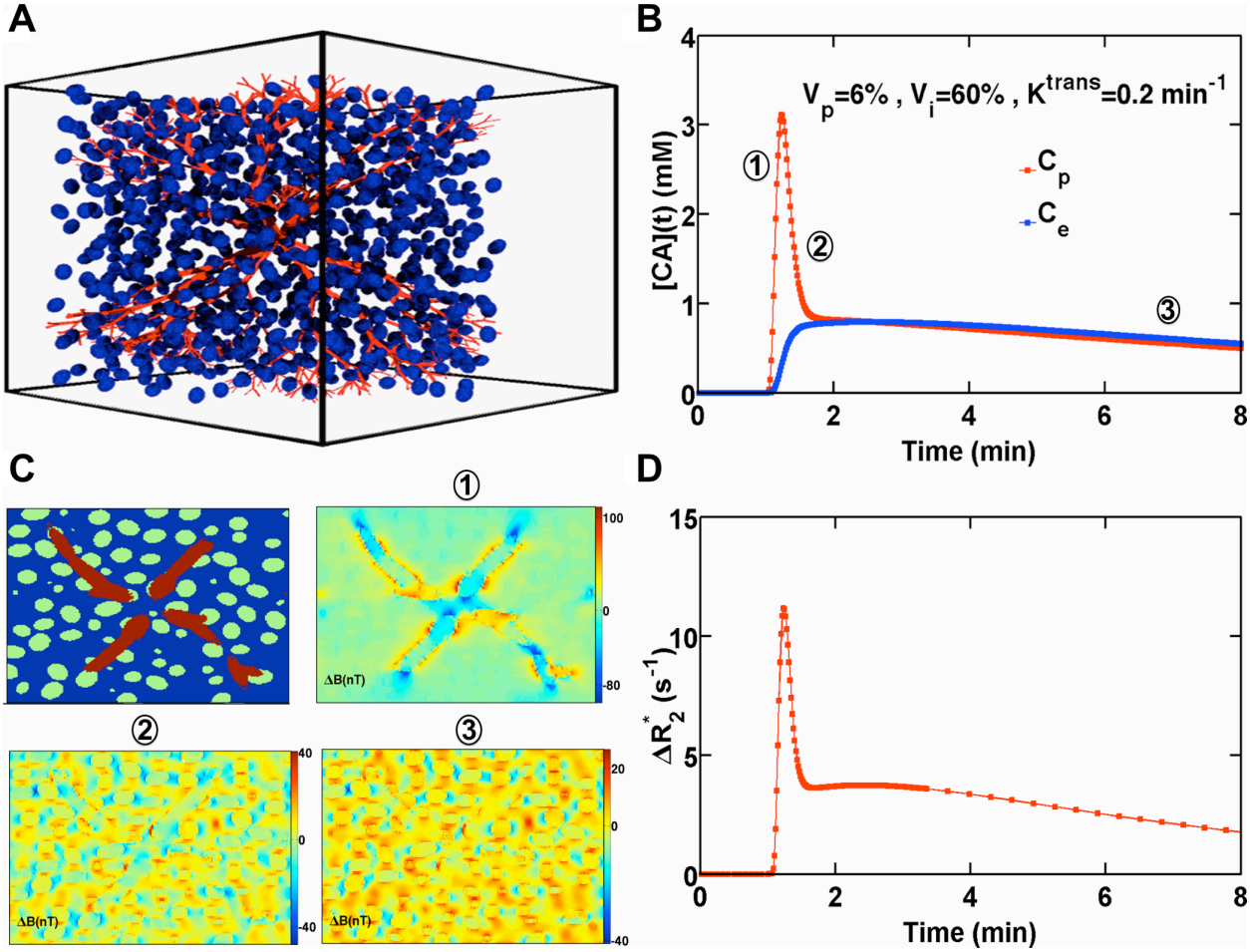

Figure 6.1: Example FPFDM simulation. (a) Sample tissue structure composed of ellipsoids packed around fractal tree based vascular network. (b) Simulated C_p and C_e curves derived using 2-compartment model. (c) Example 2D map through the tissue structure along with magnetic field perturbation computed at three different time points, showing the increasing contribution of the cells after the first pass. (d) The time evolution of the ΔR_2^* computed at $B_0 = 3$ T using the C_p and C_e curves in (b).

For CA concentration levels similar to tracer equilibrium and a range of relevant cellular and vascular volume fractions, Fig. 6.2a shows the computed ΔR_2^* values for two tissue structures containing only vascular networks (volume fractions of 6% and 9%) and four tissue structures containing only packed ellipsoids (volume fractions ranging from 20% to 65%). At a $\Delta\chi$ value of 0.2×10^{-7}, corresponding to one fifth the peak susceptibility difference for a 0.1 mmol/kg dose of Gd-DTPA, the computed ΔR_2^* values for the 45% and 65% cellular phantoms are 78% higher than that computed for the phantom containing a 9% vascular volume fraction. In general, this

difference increases with increasing susceptibility difference between tissue compartments. Fig. 6.2b shows ΔR_2^* values computed at five different tracer equilibrium concentrations for four different tissue structures with fixed cellular packing volume fraction of 55% and varying vascular volume fractions ranging from 3% to 12%. At a given tracer equilibrium concentration, the computed ΔR_2^* values are approximately equivalent for all vascular volume fractions. Across vascular volume fractions, a maximum difference of only 4% exists between the computed ΔR_2^* values, indicating that tissue vascularity has a negligible contribution to the computed ΔR_2^* values at CA equilibrium, when compared to the effects of CA compartmentalized within the EES.

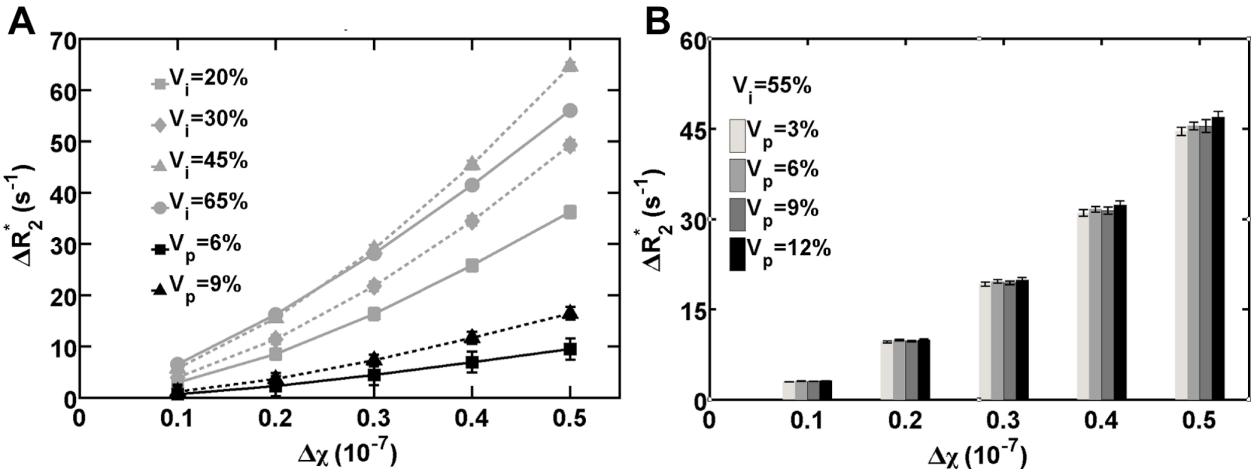

Figure 6.2: Comparison of vascular and extravascular induced ΔR_2^*. (a) A plot of the dose response of ΔR_2^* for four cellular and two vascular tissue structures. The computed ΔR_2^* values for cellular structures are substantially higher than those for the vascular structures. (b) A plot of ΔR_2^* dependence on tracer equilibrium concentration levels, for four tissue structures of fixed cellular structure but different vascular networks. At a given equilibrium concentration level the difference between the computed ΔR_2^* values is negligible, which indicates that at equilibrium the cellular features rather than the vascular differences drive the ΔR_2^* values.

The dependence of ΔR_2^* on cellular features (e.g. cell volume fraction, size) is shown in Fig. 6.3a. For a fixed cellular size, as cell volume fraction increases, the ΔR_2^* first increases and then decreases, reaching a peak value between a cell volume fraction of 40% and 45%. For a given cell volume fraction, increasing the cell size induces larger ΔR_2^* values. The computation in Fig. 6.3a is carried out at a fixed vascular volume fraction of 6% and equilibrium CA concentration corresponding to a $\Delta\chi$ value of 0.5×10^{-7}.

Figure 6.3b shows the dependence of ΔR_2^* on tissue CA concentration for two tissue structures, both with 6% vascular volume fraction and 55% cellular volume fraction, but different cell sizes. As compared to ΔR_2^* values computed for the tissue structure with smaller cell size (10 μm), the computed ΔR_2^* values for the tissue structure built using larger cell size

(20 μm) has higher values at each CA concentration levels, owing to its larger field perturbation and a smaller diffusion narrowing process.

The dose response of ΔR_2^* shown in Fig. 6.3b was used to estimate the *TRATE* parameter using the slope of a linear regression fit. Figure 6.3c shows the dependence of *TRATE* on cell size and volume fraction. For both tissue structures, *TRATE* increases with increasing cell volume fraction well up to 60%, unlike the ΔR_2^* values, which peaked near 40% cell volume fraction. For a given cell density, *TRATE* is also shown to increase with cell size.

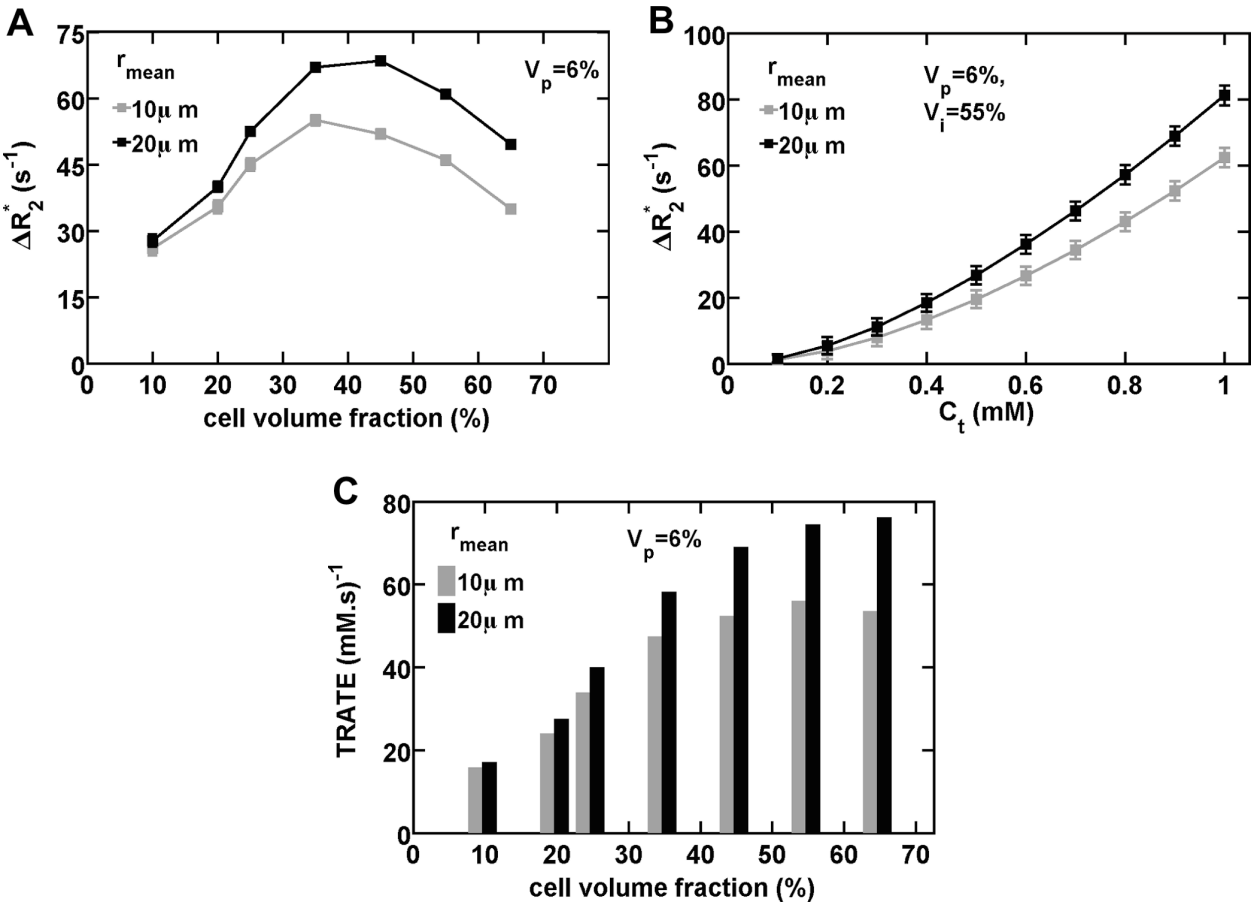

Figure 6.3: Dependence of ΔR_2^* and *TRATE* on cell size and volume fraction. (a) A plot of ΔR_2^* dependence on cell volume fraction and size. For a given cell volume fraction ΔR_2^* is larger for structures with 20 μm ellipsoids as compared to that with 10 μm ellipsoids. For a given cell size ΔR_2^* is sensitive to changes in cell volume fraction reaching a peak value approximately between 35% and 45%. (b) The linear response of ΔR_2^* to changes in tissue CA concentration for two tissue structures with different cell sizes. (c) The influence of cell volume fraction and size on *TRATE*. Unlike ΔR_2^* which peaks near 40% cell volume fraction, *TRATE* increases up to 60% cell volume fraction.

Example multi-echo DSC-MRI derived ΔR_2^* and ΔR_1 time curves for C6 glioblastoma, 9L gliosarcoma and normal tissue region of interests (ROI)s are illustrated in Fig. 6.4. The ΔR_1 time curves in C6 and 9L tumors and normal tissue are different in both magnitude and shape, illustrating the differences between the CA kinetics within these tissues. The derived ΔR_2^* time series in 9L tumors exhibited substantial and prolonged (out to 15 minutes) T_2^* leakage effects. In C6 tumors, these effects, while present, were less pronounced, as the ΔR_2^* values plateau after three minutes. In normal tissue, the ΔR_2^* values decrease to nearly pre-contrast levels immediately after the peak.

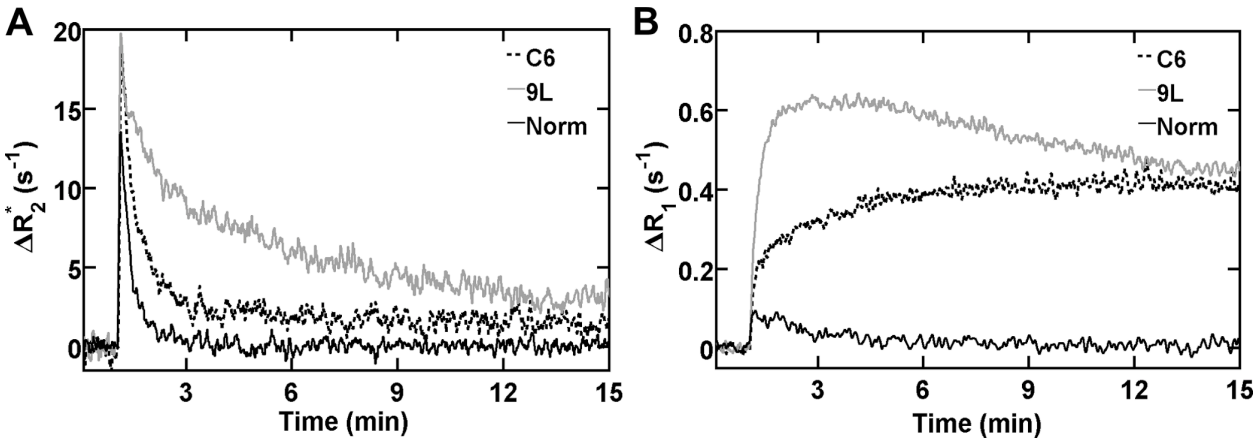

Figure 6.4: Example *in vivo* ΔR_2^* and ΔR_1 time curves. Example dual-echo DSC-MRI derived ΔR_2^* (a), and ΔR_1 (b) time curves for the C6 and 9L rat brain tumor ROIs along with a representative normal tissue. The 9L tumors exhibit elevated ΔR_2^* values that persist until the end of the scan. The ΔR_2^* values were much lower in C6 tumors. The ΔR_1 time curves for C6 and 9L tumor are markedly different indicating their unique pharmacokinetic characteristics.

Figure 6.5 depicts example C6 and 9L, K^{trans}, v_e, *ADC* and *TRATE* maps. Within a given tumor, the *TRATE* values were spatially heterogeneous. In these examples, the *TRATE* values were also markedly higher in the 9L tumors as compared to those in the C6 tumors. The *TRATE* maps exhibited little visual similarity with the other parameters. Across all the rats, the voxel-wise correlation coefficients, shown in Table 6.1, between *TRATE* and K^{trans}, v_e, *ADC* were low (with a maximum r = 0.54) and diverse.

Sample histologic images from H&E staining indicate that the C6 tumor cell density (Fig. 6.6a) is lower than that found in the 9L tumors (Fig. 6.6b). Cell nuclei count analysis shows on a group result that 9L tumors contain 30% more cells than C6 tumors (Fig. 6.7a). Consistent with this histology, *ADC* values in 9L tumors (0.87×10^{-3} mm^2/s) were significantly lower than those found in C6 tumors (1.23×10^{-3} mm^2/s) as shown in Fig. 6.7b. The *TRATE* values in 9L tumors were significantly higher (24.5 $mM^{-1}\ s^{-1}$) than those found in C6 tumors (12.9 $mM^{-1}\ s^{-1}$) as shown in Fig. 6.7c. Note that these values of *TRATE* are substantially larger than the range of T_2 relaxivity values for Gd-DTPA (3.8-4.5 $mM^{-1}\ s^{-1}$) measured in water and plasma solutions at 4.7T (111) .

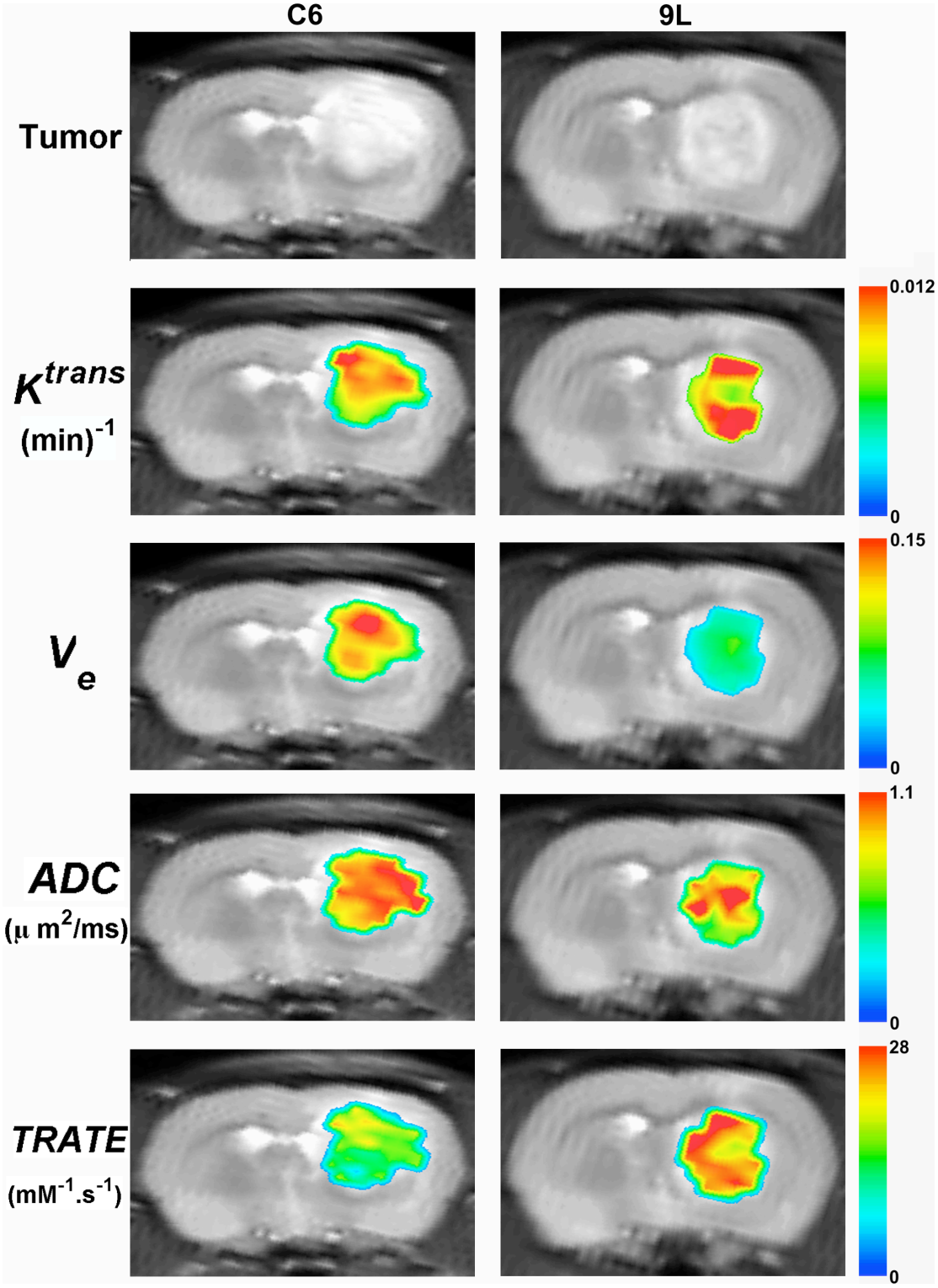

Figure 6.5: Example *in vivo* parameter maps. A comparison of *TRATE* maps with K^{trans}, v_e, *ADC* maps and anatomical post Gd-DTPA T_1 weighted images in the C6 and 9L tumors. Visually, *TRATE* maps were dissimilar to the other imaging parameters.

Table 6.1: Voxel-wise Pearson's correlation coefficient (r) between *TRATE* and *ADC*, K^{trans} and v_e for each animal included in the study.

Rat #	*ADC*	K^{trans}	v_e
1	-0.34	-0.49	-0.25
2	0.046	0.33	0.23
3	-0.18	0.01	-0.01
4	-0.12	0.18	-0.05
5	-0.39	0.30	-0.18
6	0.05	0.17	-0.11
7	-0.27	-0.06	-0.02
8	0.06	-0.19	-0.14
9	-0.27	0.22	-0.42
10	0.13	0.17	-0.08
11	0.31	0.54	0.51
12	-0.04	0.09	-0.03
13	-0.33	0.38	-0.15
14	0.01	0.25	-0.00

Figure 6.8 shows example multi-echo DSC-MRI data acquired from a ROI in a high-grade glioma patient. Similar to the 9L tumors, the derived ΔR_2^* time curves exhibit T_2^* leakage effects as shown in Fig. 6.8a. Immediately after the first pass, the ΔR_2^* only decreases by 40% of the peak value and then slowly decreases over the course of minutes, consistent with kinetics expected for CA extravasation. In contrast, normal tissue ΔR_2^* values decrease to nearly 85% of the peak value immediately after the peak and quickly plateau near pre-contrast levels. Example ΔR_1 time curve computed using T_{10} map and the extrapolated dual-echo data for tumor ROI is shown in Fig. 6.8b.

Figure 6.9 shows the tumor CBF, CBV, v_e, *ADC* and *TRATE* maps in this patient. As was the case in the animal tumor models, *TRATE* is heterogeneous across the tumor. The correlation between TRATE and the other imaging parameters was low (max r = 0.20). Across the tumor ROI the mean *TRATE* value was 28.8 $mM^{-1}\ s^{-1}$.

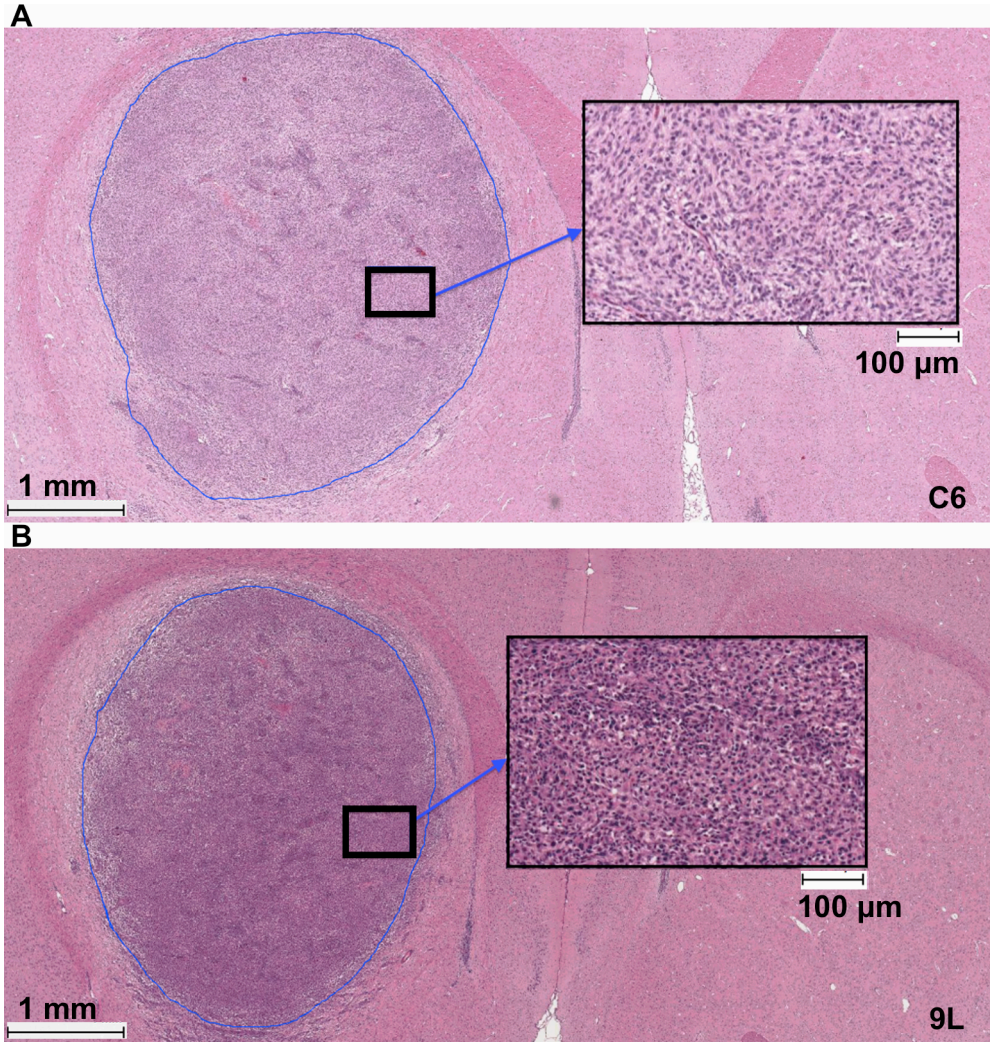

Figure 6.6: Example histological images. Representative H&E images for the C6 (a), and 9L (b) tumors, shows high cell density in 9L tumors.

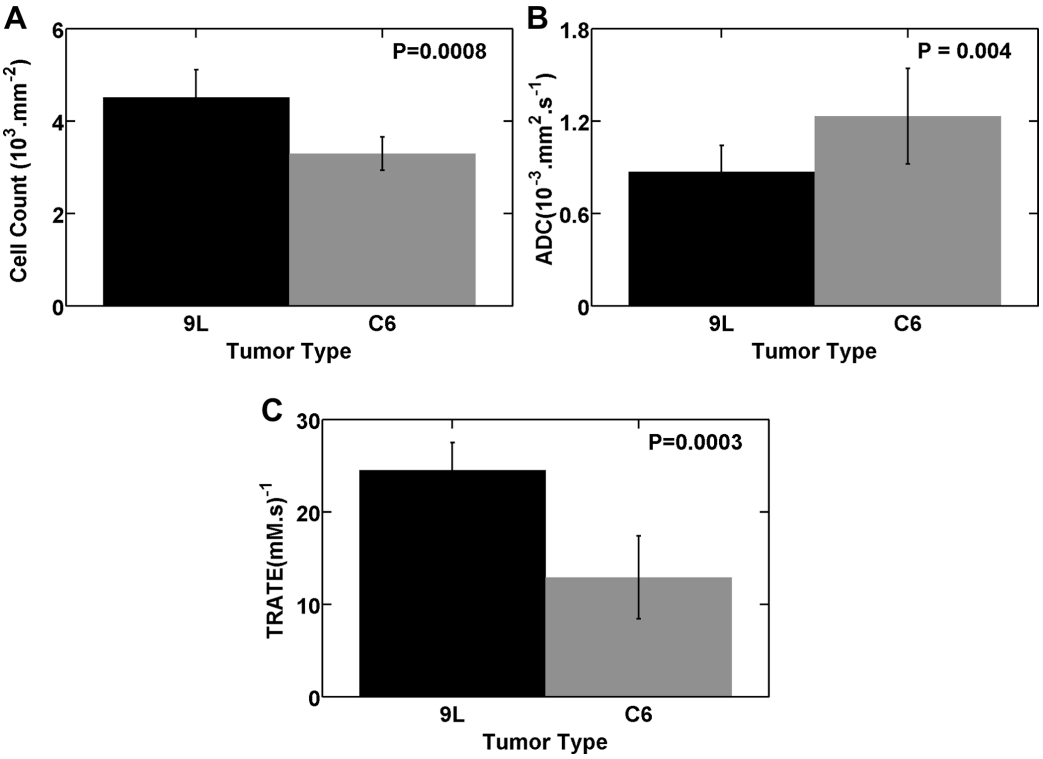

Figure 6.7: In vivo parameter estimates. (a) A group analysis of the cell nuclei count shows that 9L tumor types contain approximately 30% more cells than the C6 tumors. (b) The average ADC values in 9L tumors are significantly lower than those found in C6 tumors. (c) The average *TRATE* values in 9L tumors were significantly higher than those found in C6 tumors.

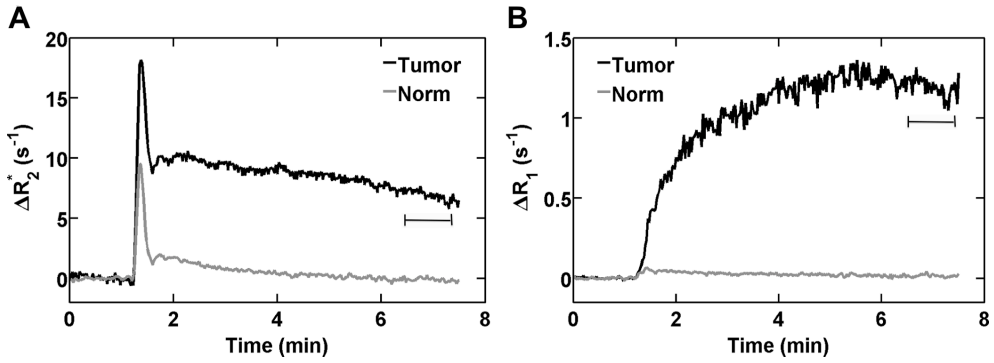

Figure 6.8: Example clinical dual-echo derived ΔR_2^* and ΔR_1 time curves. Representative dual-echo DSC-MRI derived ΔR_2^* and ΔR_1 in a patient with a recurrent high-grade glioma. (a) The tumor ROI ΔR_2^* time curve exhibits prolonged T_2^* leakage effects, whereas in normal tissue the ΔR_2^* values, after the first pass, decrease rapidly to pre-contrast levels. Example ΔR_1 time curve computed using T_{10} map and the dual-echo data for tumor ROI is shown in (b).

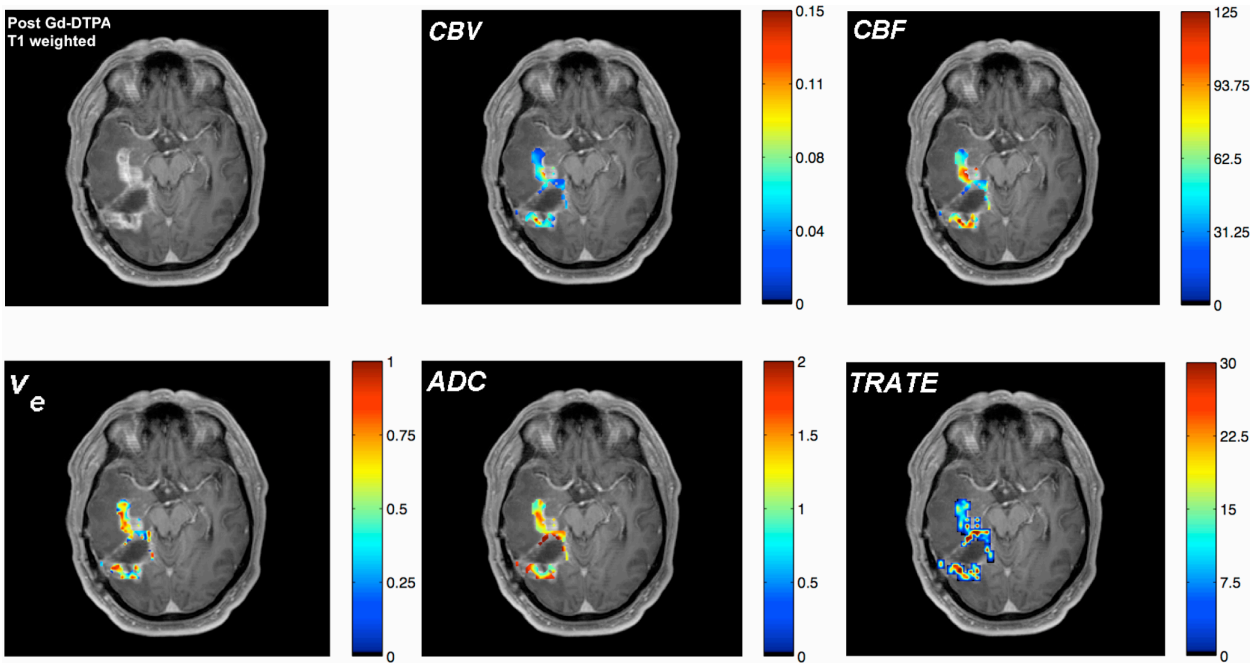

Figure 6.9: Example clinical parameter maps. Example dual-echo DSC-MRI derived maps of tumor blood volume, blood flow, v_e, *ADC*, *TRATE* along with a post-contrast T_1 weighted anatomical image in a glioma patient. The *TRATE* map is heterogeneous across the tumor ROI and visually dissimilar to the other parameter maps.

6.4 Discussion

In this study, we validate, for the first time, using realistic and systematic simulations and in vivo data, that T_2^* leakage effects, at CA equilibrium, are primarily influenced by tumor cellular characteristics. We also propose a straightforward method to quantify these effects by calculating the *TRATE* parameter, and show that it can be used to differentiate between brain tumors with varying cell density.

A key finding of the computational studies is that at tracer equilibrium the magnetic field perturbations are predominantly influenced by CA compartmentalization around cells. During the first pass of the agent the greatest field perturbation heterogeneity, as expected, is localized around blood vessels. However, at CA equilibrium, the tissue reduces to two effective compartments, the intracellular and extracellular space. Consequently, the cellular features primarily determine the induced field perturbation. Although the field perturbation created by individual cells might be weaker and fall faster than the field perturbation induced by vessels, given the high cell volume fraction of tissues, field perturbations induced by densely packed cells tends to be highly heterogeneous across the voxel, thereby influencing a large number of water protons. Consequently, susceptibility contrast induced parameters, such as *TRATE,* computed long after the first pass of the CA, are expected to depend on the underlying cellular features.

Simulation results demonstrate that cellular size and volume fraction influence the computed ΔR_2^* and *TRATE* values. For all simulated cell volume fractions, the ΔR_2^* values were larger for tissue structures packed with larger cells compared to those with smaller cells (Fig. 6.3a). An explanation for the observed ΔR_2^* on cell size and volume fraction is provided in chapter 5.

The dependence of ΔR_2^* on C_t exhibits a slight deviation from a linear relation (Fig. 6.3b). This is consistent with previous studies where a quadratic relation is observed at low CA concentration (45). However, using CA concentration values that would be expected at equilibrium, 0.1-0.5 mM, a linear regression fit yielded estimates of *TRATE* with regression values higher than 0.99. Unlike the ΔR_2^* dependence on cell volume fraction, where the peak ΔR_2^* occurs at relatively small v_i, the computed *TRATE* values increase with v_i beyond 60% and is expected to decrease for high v_i values (Fig. 6.3c). This shift of the peak to higher v_i values results from the quantification of C_t as the sum of individual compartment CA concentration weighted by the corresponding volume fractions ($C_t = v_e C_e + v_p C_p$). For a given equilibrium CA concentration (C_{eq}) and v_p values, the calculated C_t values, which are equivalent to $(1\text{-}v_i)C_{eq}$, are lower for high cell density structures as compared to those with lower cell density, thereby increasing *TRATE*. Although a more stringent systematic simulation study on the relation between *TRATE* and various physical, physiological and pulse sequence parameters is warranted, these results demonstrate that *TRATE* provides a reasonable range of sensitivity to in vivo cellular volume fraction levels (102).

As described above, Sourbron *et al* recently proposed T_2^*- relaxivity contrast imaging (RCI) as a means to characterize intra- and extravascular CA relaxivities in vivo (19). In general, *TRATE* imaging may be considered a subset of RCI as it focuses only on measuring CA relaxivity at tracer equilibrium rather than over the entire time course. Practically, the assessment of *TRATE* is computationally simpler as it does not rely upon multiple post-processing steps, including the extraction of parameters from a DCE-MRI two-compartment exchange model and the reliable separation C_p and C_e time curves. This later step highlights a key difference between RCI and *TRATE*. Whereas RCI aims to separate the intra- and extravascular CA relaxivities, *TRATE*, by definition, is the effective *tissue* CA relaxivity and, thus, only requires measuring the tissue CA concentration, which can be directly computed from the ΔR_1 time course. In the context of a DSC-MRI brain tumor study, the assessment of *TRATE* does not involve additional kinetic modeling and may provide a clinically feasible approach for characterizing tumor cellularity.

Both pre-clinical and clinical multi-echo DSC-MRI datasets exhibited substantial T_2^* leakage effects well after the first pass of the CA. Given that traditional DSC-MRI exams in brain tumors are typically no more than three minutes, this study is likely the first to confirm the presence of considerable T_2^* effects even out to ten minutes following CA injection. With single-echo acquisition methods, the detection of these T_2^* effects is confounded by simultaneous and competing changes in T_1, which is likely why they are only now being considered as a source of new tissue contrast with MRI. It is also important to note that the *TRATE* values in the brain tumors studied here were much greater than the microscopic T_2 relaxivity of Gd-DTPA, verifying that mesoscopic susceptibility changes across a voxel are the source of the T_2^* leakage effects.

Histology and *ADC* measurements indicate that 9L tumors have a higher cell density than that found in C6 tumors. Consistent with the computational results showing that *TRATE* increases with increasing cell volume fraction, the *TRATE* values in 9L tumors were significantly higher than those in C6 tumors. In addition to the dissimilar *TRATE* values between the C6 and

9L tumor types, there was a lack of spatial correlation between *TRATE* and *ADC*, K^{trans} or v_e, indicating that *TRATE* maps could potentially serve as a new metric with which to evaluate tumor tissue. The dependence of *ADC* on cell density, however, is well established (115). As shown here, *TRATE* is sensitive to cell density but also upon other physical or physiological parameters that could alter the susceptibility induced transverse relaxation rates, such as, *ADC*, cellular size, cellular shape and overall cellular organization (49,103,104). This complex dependence of *TRATE* likely explains the lack of a spatial correlation between *TRATE* and *ADC*. Further studies are warranted to investigate the specific differences between the sensitivity of *TRATE* and *ADC* measurements to tissue cytoarchitecture.

From Fig. 6.4 it is clear that 9L and C6 tumors exhibit marked differences in their ΔR_1 time courses, which is indicative of differences in vascular hemodynamics, tissue compartment sizes and permeability. Thus, the sensitivity of ΔR_2^* measurements alone to tumor cellularity, even at CA equilibrium, is likely confounded by heterogeneous and dynamic changes in the tissue CA concentration. Because estimates of *TRATE* incorporate measures of the tissue CA concentration, the effect of these differences is minimized. *TRATE*, therefore, is instead influenced by local CA distribution within the EES. This sensitivity is in contrast to other perfusion-based imaging metrics such as PSR, which represents a complex combination of tissue microstructure and hemodynamic effects including blood flow, blood volume, vascular permeability, cell volume fraction and cellular geometry. Fortunately, the use of multiple-echo DSC-MRI, permits the separation of many of these factors through estimates of ΔR_1 and ΔR_2^*, enabling the isolation of tissue geometrical factors (e.g cell density and distribution). In addition, the acquisition of multiple echoes and calculation of absolute tissue relaxation rates likely makes the method for estimating *TRATE* less sensitive to pulse sequence parameters when compared to metrics such as PSR (70). Validation of this point, however, is the subject of future analysis.

Though pulse sequence parameters, such as echo time, may have nominal influence on the estimate of *TRATE*, the time, after CA injection, during which the measurement is made could be significant. Estimation of *TRATE* relies on the assumption that the distribution of CA is in a state of equilibrium between the vascular and extravascular extracellular space. With the use of a two-compartment pharmacokinetic modeling (61) it can be shown that, for a range of physiological parameters relevant to brain cancer, CA equilibrium occurs approximately five to seven minutes after CA injection. For this reason, estimation of *TRATE* requires a moderately longer DSC-MRI acquisition time. Additionally, physiological phenomena such as tissue necrosis could also influence *TRATE* measurements. In the case of tumor necrosis, which often occurs in both animal and human brain tumors, diffusion of CA into the necrotic region can occur, resulting in continuously increasing ΔR_1 (116). The estimate of *TRATE* in these regions may be confounded if CA equilibrium is never reached.

As previously indicated, there do exist limitations on the method for calculating *TRATE*. These limitations, however, are mainly focused on the tissue being analyzed and more specifically its vascular permeability. To reiterate, estimations of *TRATE* require CA extravasation out of the vasculature. Though computing a threshold for the amount of CA extravasation required is beyond the scope of the work presented here, the change in R_1 after contrast injection should be many times greater than the standard deviation of the baseline R_1 to avoid contributions from noise. An example where the ability to estimate *TRATE* may be impeded by insignificant changes in R_1 after CA injection is the case of brain tumor treatment with an antiangiogenic drug (e.g. bevacizumab). Antiangiogenic agents can nearly restore the BBB and essentially eliminate CA extrasvasation (6). *TRATE* estimates made during this process

(i.e. to evaluate treatment-induced changes in tumor cellularity) may be grossly overestimated due to the small mean ΔR_1, and caution should be used in the interpretation of these results. Future studies will seek to establish voxel-wise criteria on when *TRATE* can be reliably measured and its reproducibility.

In addition to studies aiming to further characterize the biophysical basis of *TRATE,* there are numerous opportunities to explore the clinical role of *TRATE* measurements. Given the previously shown potential of PSR to differentiate between lymphomas, gliomas and brain metastasis based on the presence or absence of T_2^* leakage effects (71), it is likely that *TRATE* would show similar differences while at the same time providing a quantitative and pulse sequence independent measure. The sensitivity of *TRATE* to cell density suggests its potential role to assess treatment-induced cytotoxicity, similar to the current use of functional diffusion mapping (117). Finally, although *TRATE* was assessed here using a DSC-MRI acquisition, it could just as easily be estimated as part of a multi-echo DCE-MRI study or even a multi-echo, post-CA injection steady-state exam. The use of these methods would enable the estimation of *TRATE,* and therefore cytoarchitectural features, at higher resolution and in any tissue in or outside the brain using clinically available pulse sequences.

6.5 Conclusion

DSC-MRI is commonly used to assess the vascular and hemodynamic status of brain tumors. When acquired with multi-echo pulse sequences and pre-contrast T_1 maps the studies described herein show that, by leveraging T_2^* leakage effects, tumor cellular features can also be interrogated through the parameter *TRATE*. The sensitivity of *TRATE* to tissue cytoarchitecture indicate that it could potentially serve as a unique structural signature or "trait" of different types of cancers and may be useful as a biomarker of cancer aggressiveness and early treatment response. Results in pre-clinical and clinical brain tumors indicate that *TRATE* provides unique information not present in DCE- and DSC-MRI parameters or DWI based *ADC* maps. Further computational and in vivo studies are needed to systematically characterize the dependency of *TRATE* on cellular geometry (e.g. orientation heterogeneity, shape, spatial distribution), establishing its reproducibility and sensitivity to cell density variations in other tumor types and during the course of treatment.

CHAPTER 7

CONCLUSION AND FUTURE DIRECTION

DSC-MRI derived tumor perfusion parameters such as, CBV, CBF, and MTT has proven to be useful for characterizing tumor grade and treatment response. Despite its increased use in brain tumor and stroke patients, accurate calculation of perfusion parameters using DSC-MRI relies on two assumptions: 1) a linear relationship, with a spatially uniform k_p exists between CA concentration and the measured ΔR_2^*; and 2) the blood-brain barrier (BBB) is intact, so that CA remains intravascular and can be treated as a nondiffusible tracer. However, heterogeneous distributions of blood vessels within tissue and the dependence of susceptibility field gradients on vascular geometry may yield spatially variant k_p values across tissue. This is supported by several theoretical and experimental studies suggesting the sensitivity of mesoscopic relaxtion on vascular geometry (36,45,57-59). Furthermore, DSC-MRI signals acquired in the presence of CA extravasation are ambiguous due to additional changes in T_1 and T_2^* relaxivity (17-21). In this dissertation, using an efficient computational approach the biophysical basis of DSC-MRI signals has been comprehensively investigated. The major contributions of this thesis include:

1) Developing and validating an improved computational approach that combines the FPM with a matrix-based finite difference method (FDM) termed the Finite Perturber the Finite Difference Method (FPFDM), in order to efficiently investigate the influence of complex vascular and extravascular morphological features on susceptibility-induced transverse relaxation.
2) Developing realistic biological tissues models composed of ellipsoids packed around fractal-tree based vascular networks. The application of vascular network models enabled us to evaluate the relation between k_p and morphological parameters such as, branching angles, and bifurcation index. Modeling cells as ellipsoids enabled a model system that better mimics cellular densities found *in vivo,* the systematic investigation of several features relevant to DSC-MRI including ellipsoid orientation heterogeneity, volume, aspect ratio and higher packing fractions.
3) Demonstrating marked k_p heterogeneity across vascular networks, which suggests that the assumption of a constant k_p for all tissue types could affect DSC-MRI derived perfusion parameters. Computational results indicate that, compared to normal vascular networks, tumor vascular morphological features could lead to increased and decreased k_p values However, the observed k_p heterogeneity suggests treatment induced changes in vascular architecture could affect the interpretation of serial DSC-MRI data during treatment response. Further studies are needed to explore such effects and suggest the need to validate serial DSC-MRI measurements of tumor hemodynamics.
4) The discovery that DSC-MRI derived T_2 and T_2^* leakage effects depend on extravascular space features such as, cellular size, density, shape, distribution, arrangement and water diffusion coefficient. This supports the hypothesis that DSC-MRI derived CA leakage effects could potentially be used to extract information about the underlying spatial distribution of tumor cells within tissue.
5) Presenting a new approach to evaluate whether multi-echo DSC-MRI derived measures of the Transverse Relaxivity at Tracer Equilibrium (*TRATE*) may be used to characterize brain

tumor cytoarchitecture. Computational and experimental *in vivo* studies indicate that *TRATE* depend on cellular features. A voxel-wise comparison of *TRATE* with *ADC*, v_e, and K^{trans} maps showed low spatial correlation, indicating that *TRATE* could potentially serve as a new metric with which to evaluate tumor cellularity.

Although the presented experimental and computational results demonstrates the influence of vascular and cellular morphology on DSC-MRI derived transverse relaxation rates, and provides a means to characterize the tumor cellularity, there exist a great deal of research to be done to exploit and understand susceptibility contrast. Future studies will include:

1) The current computation approach does not consider the effects of *arbitrary* CA distribution within a given compartment and water exchange rate. Future studies will investigate the effect of water exchange rate and CA distribution on the observed morphological dependence of DSC-MRI derived ΔR_2^* and *TRATE* values.
2) The use of the FPFDM to systematically determine the most robust acquisition and post-processing schemes for reliable measure of tumor blood flow and blood volume. Contrast agent leakage effects still reduce the reliability of DSC-MRI measures of blood flow and volume in leaky tumor regions. To date no study has validated how clinicians should be acquiring and processing DSC-MRI data in order to extract measures of these parameters in brain tumors. The FPFDM is ideally suited for this role since we can compare dynamic signal changes, for the same vessel architecture with and without permeability, and determine which approach is best suited for the clinical environment.
3) While the FPFDM improved the computational efficiency of the FPM several improvements can still be made. We are currently exploring the use of parallel computing in order to minimize computing time for high-resolution tissue structures, which is particularly essential to model the fine structural details of vascular network (e.g. densely packed capillaries). High-resolution tissue models will improve our ability to study the dependence of DSC-MRI derived transverse relaxation rates on abnormal vascular features observed in tumors. Such studies may reveal new methods, as we discovered with *TRATE*, to non-invasively assess morphological characteristics of the tumor vasculature (e.g. vessel tortuosity), providing new ways to assess features that are known to correlate with tumor malignancy(118,119).

Given the potential of imaging parameters like percent signal recovery (PSR)(71), T_2^* relaxivity contrast imaging (RCI) (19), and *TRATE* to serve as clinical tools for evaluating the brain tumor microenvironment and treatment response, the FPFDM is currently being utilized to investigate the influence of physical, physiological and pulse sequence parameters on such emerging biomarkers.

Dynamic susceptibility contrast MRI, as a field, is over 20 years old but the underlying contrast mechanisms, applications and biological features it reflects is still evolving. The studies described herein represent significant contributions to the DSC-MRI community, from basic science tools that enable us to better characterize the biophysical basis of DSC-MRI to new *in vivo* biomarkers that may be easily extracted from clinically relevant acquisition schemes. Over time these studies should lay the groundwork that is necessary to improve the quality and type of information extracted from clinical DSC-MRI scans and thereby provide improved methods for staging and characterizing brain tumors as well as planning treatments and monitoring response.

REFERENCES

1. Damadian R. Tumor detection by nuclear magnetic resonance. Science 1971;171(3976):1151-1153.

2. Rosen BR, Belliveau JW, Vevea JM, Brady TJ. Perfusion imaging with NMR contrast agents. Magnetic resonance in medicine : official journal of the Society of Magnetic Resonance in Medicine / Society of Magnetic Resonance in Medicine 1990;14(2):249-265.

3. Meier P, Zierler KL. On the theory of the indicator-dilution method for measurement of blood flow and volume. Journal of applied physiology 1954;6(12):731-744.

4. Aronen HJ, Gazit IE, Louis DN, Buchbinder BR, Pardo FS, Weisskoff RM, Harsh GR, Cosgrove GR, Halpern EF, Hochberg FH, et al. Cerebral blood volume maps of gliomas: comparison with tumor grade and histologic findings. Radiology 1994;191(1):41-51.

5. Aronen HJ, Pardo FS, Kennedy DN, Belliveau JW, Packard SD, Hsu DW, Hochberg FH, Fischman AJ, Rosen BR. High microvascular blood volume is associated with high glucose uptake and tumor angiogenesis in human gliomas. Clinical cancer research : an official journal of the American Association for Cancer Research 2000;6(6):2189-2200.

6. Batchelor TT, Sorensen AG, di Tomaso E, Zhang WT, Duda DG, Cohen KS, Kozak KR, Cahill DP, Chen PJ, Zhu M, Ancukiewicz M, Mrugala MM, Plotkin S, Drappatz J, Louis DN, Ivy P, Scadden DT, Benner T, Loeffler JS, Wen PY, Jain RK. AZD2171, a pan-VEGF receptor tyrosine kinase inhibitor, normalizes tumor vasculature and alleviates edema in glioblastoma patients. Cancer cell 2007;11(1):83-95.

7. Bruening R, Kwong KK, Vevea MJ, Hochberg FH, Cher L, Harsh GRt, Niemi PT, Weisskoff RM, Rosen BR. Echo-planar MR determination of relative cerebral blood volume in human brain tumors: T1 versus T2 weighting. AJNR American journal of neuroradiology 1996;17(5):831-840.

8. Donahue KM, Krouwer HG, Rand SD, Pathak AP, Marszalkowski CS, Censky SC, Prost RW. Utility of simultaneously acquired gradient-echo and spin-echo cerebral blood volume and morphology maps in brain tumor patients. Magnetic resonance in medicine : official journal of the Society of Magnetic Resonance in Medicine / Society of Magnetic Resonance in Medicine 2000;43(6):845-853.

9. Maeda M, Itoh S, Kimura H, Iwasaki T, Hayashi N, Yamamoto K, Ishii Y, Kubota T. Tumor vascularity in the brain: evaluation with dynamic susceptibility-contrast MR imaging. Radiology 1993;189(1):233-238.

10. Sugahara T, Korogi Y, Kochi M, Ushio Y, Takahashi M. Perfusion-sensitive MR imaging of gliomas: comparison between gradient-echo and spin-echo echo-planar imaging techniques. AJNR American journal of neuroradiology 2001;22(7):1306-1315.

11. Lemasson B, Serduc R, Maisin C, Bouchet A, Coquery N, Robert P, Le Duc G, Tropres I, Remy C, Barbier EL. Monitoring blood-brain barrier status in a rat model of glioma receiving therapy: dual injection of low-molecular-weight and macromolecular MR contrast media. Radiology 2010;257(2):342-352.

12. Siegal T, Rubinstein R, Tzuk-Shina T, Gomori JM. Utility of relative cerebral blood volume mapping derived from perfusion magnetic resonance imaging in the routine follow up of brain tumors. Journal of neurosurgery 1997;86(1):22-27.

13. Sugahara T, Korogi Y, Tomiguchi S, Shigematsu Y, Ikushima I, Kira T, Liang L, Ushio Y, Takahashi M. Posttherapeutic intraaxial brain tumor: the value of perfusion-sensitive contrast-enhanced MR imaging for differentiating tumor recurrence from nonneoplastic contrast-enhancing tissue. AJNR American journal of neuroradiology 2000;21(5):901-909.

14. Sorensen AG, Emblem KE, Polaskova P, Jennings D, Kim H, Ancukiewicz M, Wang M, Wen PY, Ivy P, Batchelor TT, Jain RK. Increased survival of glioblastoma patients who respond to antiangiogenic therapy with elevated blood perfusion. Cancer research 2012;72(2):402-407.

15. Kamoun WS, Ley CD, Farrar CT, Duyverman AM, Lahdenranta J, Lacorre DA, Batchelor TT, di Tomaso E, Duda DG, Munn LL, Fukumura D, Sorensen AG, Jain RK. Edema control by cediranib, a vascular endothelial growth factor receptor-targeted kinase inhibitor, prolongs survival despite persistent brain tumor growth in mice. Journal of clinical oncology : official journal of the American Society of Clinical Oncology 2009;27(15):2542-2552.

16. Rosen BR, Belliveau JW, Buchbinder BR, McKinstry RC, Porkka LM, Kennedy DN, Neuder MS, Fisel CR, Aronen HJ, Kwong KK, et al. Contrast agents and cerebral hemodynamics. Magnetic resonance in medicine : official journal of the Society of Magnetic Resonance in Medicine / Society of Magnetic Resonance in Medicine 1991;19(2):285-292.

17. Quarles CC, Gochberg DF, Gore JC, Yankeelov TE. A theoretical framework to model DSC-MRI data acquired in the presence of contrast agent extravasation. Physics in medicine and biology 2009;54(19):5749-5766.

18. Sourbron S, Heilmann M, Biffar A, Walczak C, Vautier J, Volk A, Peller M. Bolus-tracking MRI with a simultaneous T1- and T2*-measurement. Magnetic resonance in medicine : official journal of the Society of Magnetic Resonance in Medicine / Society of Magnetic Resonance in Medicine 2009;62(3):672-681.

19. Sourbron S, Heilmann M, Walczak C, Vautier J, Schad LR, Volk A. T2*-relaxivity contrast imaging: first results. Magnetic resonance in medicine : official journal of the Society of Magnetic Resonance in Medicine / Society of Magnetic Resonance in Medicine 2013;69(5):1430-1437.

20. Bjornerud A, Sorensen AG, Mouridsen K, Emblem KE. T1- and T2*-dominant extravasation correction in DSC-MRI: part I--theoretical considerations and implications for assessment of tumor hemodynamic properties. Journal of cerebral blood flow and metabolism : official journal of the International Society of Cerebral Blood Flow and Metabolism 2011;31(10):2041-2053.

21. Paulson ES, Schmainda KM. Comparison of dynamic susceptibility-weighted contrast-enhanced MR methods: recommendations for measuring relative cerebral blood volume in brain tumors. Radiology 2008;249(2):601-613.

22. Rabi I, Zacharias JR, Millman S, Kusch P. A New Method of Measuring Nuclear Magnetic Moment. Physical Review 1938;53(4):318.

23. Purcell EM, Torrey HC, Pound RV. Resonance Absorption by Nuclear Magnetic Moments in a Solid. Physical Review 1946;69(1-2):37.

24. Bloch F, Hansen WW, Packard M. Nuclear Induction. Physical Review 1946;69(3-4):127.

25. Hahn EL. Spin Echoes. Physical Review 1950;80(4):580.

26. Lauterbur PC. Image Formation by Induced Local Interactions - Examples Employing Nuclear Magnetic-Resonance. Nature 1973;242(5394):190-191.

27. Wehrli FW. On the 2003 Nobel Prize in medicine or physiology awarded to Paul C. Lauterbur and Sir Peter Mansfield. Magnetic resonance in medicine : official journal of the Society of Magnetic Resonance in Medicine / Society of Magnetic Resonance in Medicine 2004;51(1):1-3.

28. Mansfield P. Multi-Planar Image-Formation Using Nmr Spin Echoes. Journal of Physics C-Solid State Physics 1977;10(3):L55-L58.

29. Ogawa S, Lee TM, Kay AR, Tank DW. Brain magnetic resonance imaging with contrast dependent on blood oxygenation. Proceedings of the National Academy of Sciences of the United States of America 1990;87(24):9868-9872.

30. Haacke EM. Magnetic resonance imaging : physical principles and sequence design. New York: Wiley; 1999. 914 p.

31. Stewart GN. Researches on the Circulation Time in Organs and on the Influences which affect it: Parts I.-III. The Journal of physiology 1893;15(1-2):1-89.

32. Zierler KL. Equations for Measuring Blood Flow by External Monitoring of Radioisotopes. Circulation research 1965;16:309-321.

33. Zierler KL. Theoretical basis of indicator-dilution methods for measuring flow and volume. Circulation research 1962;10:393– 407.

34. Ostergaard L, Weisskoff RM, Chesler DA, Gyldensted C, Rosen BR. High resolution measurement of cerebral blood flow using intravascular tracer bolus passages. Part I: Mathematical approach and statistical analysis. Magnetic resonance in medicine : official journal of the Society of Magnetic Resonance in Medicine / Society of Magnetic Resonance in Medicine 1996;36(5):715-725.

35. Rempp KA, Brix G, Wenz F, Becker CR, Guckel F, Lorenz WJ. Quantification of regional cerebral blood flow and volume with dynamic susceptibility contrast-enhanced MR imaging. Radiology 1994;193(3):637-641.

36. Pathak AP, Rand SD, Schmainda KM. The effect of brain tumor angiogenesis on the in vivo relationship between the gradient-echo relaxation rate change (DeltaR2*) and contrast agent (MION) dose. J Magn Reson Imaging 2003;18(4):397-403.

37. Miyati T, Banno T, Mase M, Kasai H, Shundo H, Imazawa M, Ohba S. Dual dynamic contrast-enhanced MR imaging. Journal of magnetic resonance imaging : JMRI 1997;7(1):230-235.

38. Willats L, Calamante F. The 39 steps: evading error and deciphering the secrets for accurate dynamic susceptibility contrast MRI. NMR in biomedicine 2013;26(8):913-931.

39. Frohlich AF, Ostergaard L, Kiselev VG. Theory of susceptibility-induced transverse relaxation in the capillary network in the diffusion narrowing regime. Magnetic resonance in medicine : official journal of the Society of Magnetic Resonance in Medicine / Society of Magnetic Resonance in Medicine 2005;53(3):564-573.

40. Kiselev VG. On the theoretical basis of perfusion measurements by dynamic susceptibility contrast MRI. Magnetic resonance in medicine : official journal of the Society of Magnetic Resonance in Medicine / Society of Magnetic Resonance in Medicine 2001;46(6):1113-1122.

41. Kiselev VG, Posse S. Analytical model of susceptibility-induced MR signal dephasing: effect of diffusion in a microvascular network. Magnetic resonance in medicine : official journal of the Society of Magnetic Resonance in Medicine / Society of Magnetic Resonance in Medicine 1999;41(3):499-509.

42. Kjolby BF, Ostergaard L, Kiselev VG. Theoretical model of intravascular paramagnetic tracers effect on tissue relaxation. Magnetic resonance in medicine : official journal of the Society of Magnetic Resonance in Medicine / Society of Magnetic Resonance in Medicine 2006;56(1):187-197.

43. Weisskoff RM, Zuo CS, Boxerman JL, Rosen BR. Microscopic susceptibility variation and transverse relaxation: theory and experiment. Magnetic resonance in medicine : official journal of the Society of Magnetic Resonance in Medicine / Society of Magnetic Resonance in Medicine 1994;31(6):601-610.

44. Boxerman JL, Bandettini PA, Kwong KK, Baker JR, Davis TL, Rosen BR, Weisskoff RM. The intravascular contribution to fMRI signal change: Monte Carlo modeling and diffusion-weighted studies in vivo. Magnetic resonance in medicine : official journal of the Society of Magnetic Resonance in Medicine / Society of Magnetic Resonance in Medicine 1995a;34(1):4-10.

45. Boxerman JL, Hamberg LM, Rosen BR, Weisskoff RM. MR contrast due to intravascular magnetic susceptibility perturbations. Magnetic resonance in medicine : official journal of the Society of Magnetic Resonance in Medicine / Society of Magnetic Resonance in Medicine 1995b;34(4):555-566.

46. Fisel CR, Ackerman JL, Buxton RB, Garrido L, Belliveau JW, Rosen BR, Brady TJ. MR contrast due to microscopically heterogeneous magnetic susceptibility: numerical simulations and applications to cerebral physiology. Magnetic resonance in medicine : official journal of the Society of Magnetic Resonance in Medicine / Society of Magnetic Resonance in Medicine 1991;17(2):336-347.

47. Kennan RP, Zhong J, Gore JC. Intravascular susceptibility contrast mechanisms in tissues. Magnetic resonance in medicine : official journal of the Society of Magnetic Resonance in Medicine / Society of Magnetic Resonance in Medicine 1994;31(1):9-21.

48. Ogawa S, Lee TM. Magnetic resonance imaging of blood vessels at high fields: in vivo and in vitro measurements and image simulation. Magnetic resonance in medicine : official journal of the Society of Magnetic Resonance in Medicine / Society of Magnetic Resonance in Medicine 1990;16(1):9-18.

49. Yablonskiy DA, Haacke EM. Theory of NMR signal behavior in magnetically inhomogeneous tissues: the static dephasing regime. Magnetic resonance in medicine : official journal of the Society of Magnetic Resonance in Medicine / Society of Magnetic Resonance in Medicine 1994;32(6):749-763.

50. Stables LA, Kennan RP, Gore JC. Asymmetric spin-echo imaging of magnetically inhomogeneous systems: theory, experiment, and numerical studies. Magnetic resonance in medicine : official journal of the Society of Magnetic Resonance in Medicine / Society of Magnetic Resonance in Medicine 1998;40(3):432-442.

51. Pathak AP, Ward BD, Schmainda KM. A novel technique for modeling susceptibility-based contrast mechanisms for arbitrary microvascular geometries: the finite perturber method. NeuroImage 2008;40(3):1130-1143.

52. Hwang SN, Chin CL, Wehrli FW, Hackney DB. An image-based finite difference model for simulating restricted diffusion. Magnetic resonance in medicine : official journal of the Society of Magnetic Resonance in Medicine / Society of Magnetic Resonance in Medicine 2003;50(2):373-382.

53. Xu J, Does MD, Gore JC. Numerical study of water diffusion in biological tissues using an improved finite difference method. Physics in medicine and biology 2007;52(7):N111-126.

54. Donahue KM, Weisskoff RM, Burstein D. Water diffusion and exchange as they influence contrast enhancement. Journal of magnetic resonance imaging : JMRI 1997;7(1):102-110.

55. Landis CS, Li X, Telang FW, Coderre JA, Micca PL, Rooney WD, Latour LL, Vetek G, Palyka I, Springer CS, Jr. Determination of the MRI contrast agent concentration time course in vivo following bolus injection: effect of equilibrium transcytolemmal water exchange. Magnetic resonance in medicine : official journal of the Society of Magnetic Resonance in Medicine / Society of Magnetic Resonance in Medicine 2000;44(4):563-574.

56. Kiselev VG. Transverse relaxation effect of MRI contrast agents: a crucial issue for quantitative measurements of cerebral perfusion. Journal of magnetic resonance imaging : JMRI 2005;22(6):693-696.

57. Gillis P, Peto S, Moiny F, Mispelter J, Cuenod CA. Proton transverse nuclear magnetic relaxation in oxidized blood: a numerical approach. Magnetic resonance in medicine : official journal of the Society of Magnetic Resonance in Medicine / Society of Magnetic Resonance in Medicine 1995;33(1):93-100.

58. Kiselev VG, Novikov DS. Transverse NMR relaxation as a probe of mesoscopic structure. Physical review letters 2002;89(27):278101.

59. Ye FQ, Allen PS. Relaxation enhancement of the transverse magnetization of water protons in paramagnetic suspensions of red blood cells. Magnetic resonance in medicine : official journal of the Society of Magnetic Resonance in Medicine / Society of Magnetic Resonance in Medicine 1995;34(5):713-720.

60. Simpson NE, He Z, Evelhoch JL. Deuterium NMR tissue perfusion measurements using the tracer uptake approach: I. Optimization of methods. Magnetic resonance in medicine : official journal of the Society of Magnetic Resonance in Medicine / Society of Magnetic Resonance in Medicine 1999;42(1):42-52.

61. Brix G, Bahner ML, Hoffmann U, Horvath A, Schreiber W. Regional blood flow, capillary permeability, and compartmental volumes: measurement with dynamic CT--initial experience. Radiology 1999;210(1):269-276.

62. Weisskoff RM, Kiihne S. MRI susceptometry: image-based measurement of absolute susceptibility of MR contrast agents and human blood. Magnetic resonance in medicine : official journal of the Society of Magnetic Resonance in Medicine / Society of Magnetic Resonance in Medicine 1992;24(2):375-383.

63. Pintaske J, Martirosian P, Graf H, Erb G, Lodemann KP, Claussen CD, Schick F. Relaxivity of Gadopentetate Dimeglumine (Magnevist), Gadobutrol (Gadovist), and Gadobenate Dimeglumine (MultiHance) in human blood plasma at 0.2, 1.5, and 3 Tesla. Investigative radiology 2006;41(3):213-221.

64. Christen T, Zaharchuk G, Pannetier N, Serduc R, Joudiou N, Vial JC, Remy C, Barbier EL. Quantitative MR estimates of blood oxygenation based on T2*: a numerical study of the impact of model assumptions. Magnetic resonance in medicine : official journal of the Society of Magnetic Resonance in Medicine / Society of Magnetic Resonance in Medicine 2012;67(5):1458-1468.

65. Klassen LM, Menon RS. NMR simulation analysis of statistical effects on quantifying cerebrovascular parameters. Biophysical journal 2007;92(3):1014-1021.

66. Pannetier NA, Debacker CS, Mauconduit F, Christen T, Barbier EL. A simulation tool for dynamic contrast enhanced MRI. PloS one 2013;8(3):e57636.

67. Hall MG, Alexander DC. Convergence and parameter choice for Monte-Carlo simulations of diffusion MRI. IEEE transactions on medical imaging 2009;28(9):1354-1364.

68. Beaumont M, Lemasson B, Farion R, Segebarth C, Remy C, Barbier EL. Characterization of tumor angiogenesis in rat brain using iron-based vessel size index MRI in combination with gadolinium-based dynamic contrast-enhanced MRI. Journal of cerebral blood flow and metabolism : official journal of the International Society of Cerebral Blood Flow and Metabolism 2009;29(10):1714-1726.

69. Marty B, Djemai B, Robic C, Port M, Robert P, Valette J, Boumezbeur F, Le Bihan D, Lethimonnier F, Meriaux S. Hindered diffusion of MRI contrast agents in rat brain extracellular micro-environment assessed by acquisition of dynamic T1 and T2 maps. Contrast media & molecular imaging 2013;8(1):12-19.

70. Boxerman JL, Paulson ES, Prah MA, Schmainda KM. The Effect of Pulse Sequence Parameters and Contrast Agent Dose on Percentage Signal Recovery in DSC-MRI: Implications for Clinical Applications. AJNR American journal of neuroradiology 2013.

71. Mangla R, Kolar B, Zhu T, Zhong J, Almast J, Ekholm S. Percentage signal recovery derived from MR dynamic susceptibility contrast imaging is useful to differentiate common enhancing malignant lesions of the brain. AJNR American journal of neuroradiology 2011;32(6):1004-1010.

72. Marques JP, Bowtell R. Application of a fourier-based method for rapid calculation of field inhomogeneity due to spatial variation of magnetic susceptibility. . Concepts in Magnetic Resonance Part B-Magnetic Resonance Engineering 2005;25B(1):65-78.

73. Salomir R, Senneville BDD, Moonen CTW. A fast calculation method for magnetic field inhomogeneity due to an arbitrary distribution of bulk susceptibility. Concepts in Magnetic Resonance Part B-Magnetic Resonance Engineering 2003;19B(1):26-34.

74. Baish JW, Gazit Y, Berk DA, Nozue M, Baxter LT, Jain RK. Role of tumor vascular architecture in nutrient and drug delivery: an invasion percolation-based network model. Microvascular research 1996;51(3):327-346.

75. Gazit Y, Berk DA, Leunig M, Baxter LT, Jain RK. Scale-invariant behavior and vascular network formation in normal and tumor tissue. Physical review letters 1995;75(12):2428-2431.

76. Jain RK. Normalizing tumor vasculature with anti-angiogenic therapy: a new paradigm for combination therapy. Nature medicine 2001;7(9):987-989.

77. Rybaczuk M, Kedzia A, Paradowski L. Fractal characteristics of brain vessel microangioarchitecture during the fetal period. Medical science monitor : international medical journal of experimental and clinical research 2002;8(8):MT145-152.

78. Schreiner W, Neumann F, Neumann M, End A, Muller MR. Structural quantification and bifurcation symmetry in arterial tree models generated by constrained constructive optimization. Journal of theoretical biology 1996;180(2):161-174.

79. Murray CD. The Physiological Principle of Minimum Work: I. The Vascular System and the Cost of Blood Volume. Proceedings of the National Academy of Sciences of the United States of America 1926;12(3):207-214.

80. Cohn D. Optimal systems I: the vascular system. Bull Math Biophys 1954;16:pp. 59–74.

81. Cohn D. Optimal systems II: the vascular system. Bull Math Biophys 1955;17:pp. 219–227.

82. Rosen R. Optimal principles in biology. London: Butterworths 1967.

83. Schreiner W, Karch R, Neumann M, Neumann F, Roedler SM, Heinze G. Heterogeneous perfusion is a consequence of uniform shear stress in optimized arterial tree models. Journal of theoretical biology 2003;220(3):285-301.

84. Schreiner W, Neumann F, Karch R, Neumann M, Roedler SM, End A. Shear stress distribution in arterial tree models, generated by constrained constructive optimization. Journal of theoretical biology 1999;198(1):27-45.

85. Zamir M. Distributing and delivering vessels of the human heart. The Journal of general physiology 1988;91(5):725-735.

86. Zamir M, Phipps S. Network analysis of an arterial tree. Journal of biomechanics 1988;21(1):25-34.

87. Changizi MA, Cherniak C. Modeling the large-scale geometry of human coronary arteries. Canadian journal of physiology and pharmacology 2000;78(8):603-611.

88. Gan RZ, Tian Y, Yen RT, Kassab GS. Morphometry of the dog pulmonary venous tree. J Appl Physiol (1985) 1993;75(1):432-440.

89. Kassab GS, Rider CA, Tang NJ, Fung YC. Morphometry of pig coronary arterial trees. The American journal of physiology 1993;265(1 Pt 2):H350-365.

90. Newman GC, Hospod FE, Patlak CS, Fain SE, Pulfer KA, Cook TD, O'Sullivan F. Experimental estimates of the constants relating signal change to contrast concentration for cerebral blood volume by T2* MRI. Journal of cerebral blood flow and metabolism : official journal of the International Society of Cerebral Blood Flow and Metabolism 2006;26(6):760-770.

91. Gabrys E, Rybaczuk M, Kedzia A. Fractal models of circulatory system. Symmetrical and asymmetrical approach comparison. Chaos Solitons & Fractals 2005;24(3): 707-715.

92. Gabrys E, Rybaczuk M, Kedzia A. Blood flow simulation through fractal models of circulatory system. . Chaos Solitons & Fractals 2006;27(1):1-7.

93. Karshafian R, Burns PN, Henkelman MR. Transit time kinetics in ordered and disordered vascular trees. Physics in medicine and biology 2003;48(19):3225-3237.

94. Dickson PV, Hamner JB, Sims TL, Fraga CH, Ng CY, Rajasekeran S, Hagedorn NL, McCarville MB, Stewart CF, Davidoff AM. Bevacizumab-induced transient remodeling of the vasculature in neuroblastoma xenografts results in improved delivery and efficacy of systemically administered chemotherapy. Clinical cancer research : an official journal of the American Association for Cancer Research 2007;13(13):3942-3950.

95. Hopfner M, Schuppan D, Scherubl H. Growth factor receptors and related signalling pathways as targets for novel treatment strategies of hepatocellular cancer. World journal of gastroenterology : WJG 2008;14(1):1-14.

96. Quarles CC, Ward BD, Schmainda KM. Improving the reliability of obtaining tumor hemodynamic parameters in the presence of contrast agent extravasation. Magnetic resonance in medicine : official journal of the Society of Magnetic Resonance in Medicine / Society of Magnetic Resonance in Medicine 2005;53(6):1307-1316.

97. Boxerman JL, Schmainda KM, Weisskoff RM. Relative cerebral blood volume maps corrected for contrast agent extravasation significantly correlate with glioma tumor grade,

whereas uncorrected maps do not. AJNR American journal of neuroradiology 2006;27(4):859-867.

98. Emblem KE, Bjornerud A, Mouridsen K, Borra RJ, Batchelor TT, Jain RK, Sorensen AG. T(1)- and T(2)(*)-dominant extravasation correction in DSC-MRI: part II-predicting patient outcome after a single dose of cediranib in recurrent glioblastoma patients. Journal of cerebral blood flow and metabolism : official journal of the International Society of Cerebral Blood Flow and Metabolism 2011;31(10):2054-2064.

99. Schmiedeskamp H, Andre JB, Straka M, Christen T, Nagpal S, Recht L, Thomas RP, Zaharchuk G, Bammer R. Simultaneous perfusion and permeability measurements using combined spin- and gradient-echo MRI. Journal of cerebral blood flow and metabolism : official journal of the International Society of Cerebral Blood Flow and Metabolism 2013;33(5):732-743.

100. Delaney GW, Cleary PW. The packing properties of superellipsoids. . Europhys Lett 2010;89:34002.

101. Yamasaki F, Kurisu K, Satoh K, Arita K, Sugiyama K, Ohtaki M, Takaba J, Tominaga A, Hanaya R, Yoshioka H, Hama S, Ito Y, Kajiwara Y, Yahara K, Saito T, Thohar MA. Apparent diffusion coefficient of human brain tumors at MR imaging. Radiology 2005;235(3):985-991.

102. Jain RK. Transport of molecules in the tumor interstitium: a review. Cancer research 1987;47(12):3039-3051.

103. Pannetier N, Debacker C, Mauconduit F, Christen T, Barbier E. Does R2 * increase or decrease when contrast agent extravasates? A simulation study. 2011; Montreal, Canada. p p. 3916.

104. Semmineh NB, Xu J, Boxerman JL, Delaney GW, Cleary PW, Gore JC, Quarles CC. An efficient computational approach to characterize DSC-MRI signals arising from three-dimensional heterogeneous tissue structures. PloS one 2014;9 (1):e84764.

105. Hosokawa M, Kenmotsu H, Koh Y, Yoshino T, Yoshikawa T, Naito T, Takahashi T, Murakami H, Nakamura Y, Tsuya A, Shukuya T, Ono A, Akamatsu H, Watanabe R, Ono S, Mori K, Kanbara H, Yamaguchi K, Tanaka T, Matsunaga T, Yamamoto N. Size-based isolation of circulating tumor cells in lung cancer patients using a microcavity array system. PloS one 2013;8(6):e67466.

106. Kim EJ, Kim DH, Lee SH, Huh YM, Song HT, Suh JS. Simultaneous acquisition of perfusion and permeability from corrected relaxation rates with dynamic susceptibility contrast dual gradient echo. Magnetic resonance imaging 2004;22(3):307-314.

107. Quarles CC, Gore JC, Xu L, Yankeelov TE. Comparison of dual-echo DSC-MRI- and DCE-MRI-derived contrast agent kinetic parameters. Magnetic resonance imaging 2012;30(7):944-953.

108. Sourbron S, Ingrisch M, Siefert A, Reiser M, Herrmann K. Quantification of cerebral blood flow, cerebral blood volume, and blood-brain-barrier leakage with DCE-MRI. Magnetic resonance in medicine : official journal of the Society of Magnetic Resonance in Medicine / Society of Magnetic Resonance in Medicine 2009;62(1):205-217.

109. Vonken EP, van Osch MJ, Bakker CJ, Viergever MA. Simultaneous quantitative cerebral perfusion and Gd-DTPA extravasation measurement with dual-echo dynamic susceptibility contrast MRI. Magnetic resonance in medicine : official journal of the Society of Magnetic Resonance in Medicine / Society of Magnetic Resonance in Medicine 2000;43(6):820-827.

110. Le Bihan D. [Diffusion, perfusion and functional magnetic resonance imaging]. Journal des maladies vasculaires 1995;20(3):203-214.

111. Rohrer M, Bauer H, Mintorovitch J, Requardt M, Weinmann HJ. Comparison of magnetic properties of MRI contrast media solutions at different magnetic field strengths. Investigative radiology 2005;40(11):715-724.

112. Barbier EL, den Boer JA, Peters AR, Rozeboom AR, Sau J, Bonmartin A. A model of the dual effect of gadopentetate dimeglumine on dynamic brain MR images. Journal of magnetic resonance imaging : JMRI 1999;10(3):242-253.

113. Yankeelov TE, Luci JJ, Lepage M, Li R, Debusk L, Lin PC, Price RR, Gore JC. Quantitative pharmacokinetic analysis of DCE-MRI data without an arterial input function: a reference region model. Magnetic resonance imaging 2005;23(4):519-529.

114. Wu O, Ostergaard L, Weisskoff RM, Benner T, Rosen BR, Sorensen AG. Tracer arrival timing-insensitive technique for estimating flow in MR perfusion-weighted imaging using singular value decomposition with a block-circulant deconvolution matrix. Magnetic resonance in medicine : official journal of the Society of Magnetic Resonance in Medicine / Society of Magnetic Resonance in Medicine 2003;50(1):164-174.

115. Anderson AW, Xie J, Pizzonia J, Bronen RA, Spencer DD, Gore JC. Effects of cell volume fraction changes on apparent diffusion in human cells. Magnetic resonance imaging 2000;18(6):689-695.

116. Skinner JT, Yankeelov TE, Peterson TE, Does MD. Comparison of dynamic contrast-enhanced MRI and quantitative SPECT in a rat glioma model. Contrast media & molecular imaging 2012;7(6):494-500.

117. Moffat BA, Chenevert TL, Lawrence TS, Meyer CR, Johnson TD, Dong Q, Tsien C, Mukherji S, Quint DJ, Gebarski SS, Robertson PL, Junck LR, Rehemtulla A, Ross BD.

Functional diffusion map: a noninvasive MRI biomarker for early stratification of clinical brain tumor response. Proceedings of the National Academy of Sciences of the United States of America 2005;102(15):5524-5529.

118. Bullitt E, Zeng D, Gerig G, Aylward S, Joshi S, Smith JK, Lin W, Ewend MG. Vessel tortuosity and brain tumor malignancy: a blinded study. Academic radiology 2005;12(10):1232-1240.

119. Lorthois S, Cassot F. Fractal analysis of vascular networks: insights from morphogenesis. Journal of theoretical biology 2010;262(4):614-633.